RICE UNIVERSITY

Two-dimensional molybdenum ditelluride (MoTe2): synthesis, characterization, and application
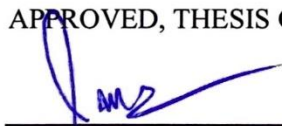
by

Xiang Zhang

A THESIS SUBMITTED
IN PARTIAL FULFILLMENT OF THE
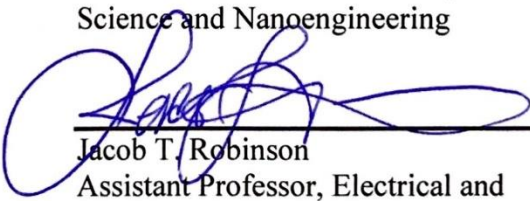REQUIREMENTS FOR THE DEGREE

Doctor of Philosophy

APPROVED, THESIS COMMITTEE

Pulickel M. Ajayan, Chair
Benjamin M. and Mary Greenwood
Anderson Professor, Materials Science and
Nanoengineering, Department Chair

Robert Vajtai
Associate Research Professor, Materials
Science and Nanoengineering

Jacob T. Robinson
Assistant Professor, Electrical and
Computer Engineering and Bioengineering

HOUSTON, TEXAS
April 2018

ABSTRACT

Two-dimensional molybdenum ditelluride (MoTe2): synthesis, characterization, and application

by

Xiang Zhang

Recent research efforts in two-dimensional (2D) materials have shown an increasing focus on molybdenum ditelluride (MoTe$_2$). Unlike other TMDs, MoTe$_2$ is distinguished by the existence of two stable phases, hexagonal 2H phase and monoclinic 1T' phase, both of which can be synthesized directly. 2H MoTe$_2$ is a semiconductor with a band gap of ∼ 1 eV, while 1T' MoTe$_2$ is metallic which can be transformed to a type-II Weyl semimetal at low temperature. The semiconductor-metal junction between 2H and 1T' MoTe$_2$ shows the potential to resolve the issue of the existence of high Schottky barrier in traditional devices. MoTe$_2$ does not only possesses a myriad of physical properties to further unravel but also shows great potential towards various industrial applications such as analog circuits and spintronics.

Chapter 1 gives a brief introduction to 2D materials. Several common synthesis methods and characterization methods are discussed. The structure, properties, and chemical vapor deposition (CVD) synthesis process of three important members in the 2D family, graphene, hexagonal boron nitride (h-BN) and

transition metal dichalcogenides (TMDs) are introduced. In the end, a few application examples of 2D materials are mentioned.

Chapter 2 focuses on the phase-controlled synthesis of large-area $MoTe_2$ films and 2H/1T' $MoTe_2$ heterostructures by CVD. The as-grown $MoTe_2$ films have been characterized by Raman spectroscopy, X-ray diffraction (XRD), atomic force microscopy (AFM), X-ray photoelectron spectroscopy (XPS), ultraviolet-visible (UV-vis) spectrophotometry, micro-extinction spectroscopy (MExS), and transmission electron microscopy (TEM), with extra attention to the differences between 2H phase and 1T' phase. In addition, converting MoS_2 or $MoSe_2$ to $MoTe_2$ has been found as another possible synthesis approach.

In chapter 3, several types of $MoTe_2$-based devices are fabricated and measured. In a field-effect transistor (FET) device, 2H phase $MoTe_2$ channel shows p-type semiconducting behavior and exhibits exponentially higher sheet resistance than 1T' $MoTe_2$. We also demonstrate a decreased contact resistance through using the 1T' phase as the contact electrodes for 2H phase-based transistor by observing improved drain-source current compared to Ti/Au metal contacts. Theoretical simulations further confirm that the contact barrier of 2H/1T' $MoTe_2$ in-plane heterostructure is lower than that of 2H $MoTe_2$/Ti vertical junction.

Chapter 4 studies the surface Raman enhancement on 2H and 1T' $MoTe_2$. Copper phthalocyanine (CuPc) and rhodamine 6G (R6G) are used as the probe molecules. The surface-enhanced Raman scattering (SERS) signal is found to become stronger with a phase-transition from 2H phase to 1T' phase, and with a decreasing

number of layers of MoTe$_2$. Additionally, the MoTe$_2$-based heterostructures, such as graphene/MoTe$_2$ and h-BN/MoTe$_2$, are also explored as novel platforms for SERS enhancement. Their performance has been carefully analyzed and is supported by theoretical simulations.

Chapter 5 introduces our recent effort in the spatial phase-targeted synthesis of 2H and 1T' MoTe$_2$. A series of technique has been adapted to characterize MoTe$_2$ films synthesized by this novel method. We also show that this strategy is suitable not only for large-scale patterns but also for tiny features. A substrate with tens of dumbbell-shaped devices has been successfully fabricated, each of which has a 2H phase channel connected by a 1T' phase square on each side.

In chapter 6, we use the ultrafast electron diffraction (UED) to investigate the nonradiative process in 2H MoTe$_2$ at SLAC National Accelerator Laboratory. The pump-probe kinetics and momentum-dependent kinetics have been studied.

This thesis doesn't only study the fundamental properties of MoTe$_2$ but also paves the way towards the large-scale application of MoTe$_2$ in electronic and optoelectronic devices.

Acknowledgments

I would like to thank Prof. Ajayan for giving me this opportunity to work in his group. Prof. Ajayan's immense knowledge, creative thoughts, and great vision have inspired me a lot in research. His enthusiasm, patience, and noble personality show me what an excellent researcher & advisor should be. I also feel very grateful for the freedom he gives to this group, which makes me have enough opportunities to explore many different areas, to learn various knowledge and techniques, to collaborate with people from all kinds of background around the country, and the world. It is my great honor to graduate with a Ph.D. from Prof. Ajayan's group.

I would like to thank Prof. Vajtai for his help and guidance during my Ph.D. career. Prof. Vajtai is always in his office, willing to discuss with me, to help me solve any problem. I also want to thank Prof. Robinson for serving on my thesis committee and providing insightful comments.

I would like to appreciate all the people who have been involved in the work presented in this thesis, Zehua Jin, Luqing Wang, Prof. Lulu Qu, Dr. Ming-Fu Lin, Fan Ye, Dr. Rachel Koltun, Jordan A. Hachtel, Dr. Weipeng Wang, Eduardo Villarreal, Dr. Yusuke Nakanishi, Zixing Wang, Jiawei Lai, Teresa Ha, Dr. Chandra Sekhar Tiwary, Dr. Shize Yang, Prof. Emilie Ringe, Prof. Boris I. Yakobson, Prof. Jun Lou. I could not imagine my thesis to be completed without their contributions.

In addition, I want to thank these people who have helped me during my time at Rice, Prof. Bo Li, Prof. Yongji Gong, Prof. Jingjie Wu, Dr. Lulu Ma, Dr. Kunttal

Contents

List of Figures

List of Tables

List of Equations

Nomenclature

0D	Zero-dimensional
1D	One-dimensional
2D	Two-dimensional
3D	Three-dimensional
AFM	Atomic force microscope
CVD	Chemical vapor deposition
DFT	Density functional theory
EDX	Energy-dispersive X-ray spectroscopy
FET	Field emission transistor
HADDF	High-angle annular dark field
h-BN	Hexagonal boron nitride
HER	Hydrogen evolution reaction
$MoTe_2$	Molybdenum ditelluride
PL	Photoluminescence
PMMA	Poly (methyl methacrylate)
RIE	Reactive-ion etching
sccm	standard cubic centimeters per minute
SEM	Scanning electron microscopy
SERS	Surface enhanced Raman scattering
STEM	Scanning transmission electron microscopy

TEM	Transmission electron microscopy
TMDs	Transition metal dichalcogenides
UED	Ultrafast electron diffraction
UV-vis	Ultraviolet-visible
vdWs	Van der Waals
XPS	X-Ray photoelectron spectroscopy
XRD	X-ray diffraction

<div align="right">

Chapter 1

</div>

<div align="right">

Introduction

</div>

1.1. 2D materials

The exfoliation of graphene from graphite in 2004 was deemed to be the birth of 2D materials.[1] Since that a lot of research has been dedicated into 2D materials due to their unique properties which do not exist in their bulk counterparts. The family of 2D materials has grown to include metals, semiconductors, and insulators. They provide a wide range of basic building blocks for advanced technological applications.

Graphene family	Graphene	hBN 'white graphene'		BCN	Fluorographene	Graphene oxide
2D chalcogenIdes	MoS_2, WS_2, $MoSe_2$, WSe_2		Semiconducting dichalcogenides: $MoTe_2$, WTe_2, ZrS_2, $ZrSe_2$ and so on	Metallic dichalcogenides: $NbSe_2$, NbS_2, TaS_2, TiS_2, $NiSe_2$ and so on		
				Layered semiconductors: GaSe, GaTe, InSe, Bi_2Se_3 and so on		
2D oxides	Micas, BSCCO	MoO_3, WO_3	Perovskite-type: $LaNb_2O_7$, $(Ca,Sr)_2Nb_3O_{10}$, $Bi_4Ti_3O_{12}$, $Ca_2Ta_2TiO_{10}$ and so on		Hydroxides: $Ni(OH)_2$, $Eu(OH)_2$ and so on	
	Layered Cu oxides	TiO_2, MnO_2, V_2O_5, TaO_3, RuO_2 and so on			Others	

Table 1.1 – 2D materials family.[2]

1.2. Synthesis of 2D materials

Preparation of materials is the foundation for exploring their properties and applications. Various methods have been developed to synthesize 2D materials, such as mechanical exfoliation, liquid exfoliation, hydrothermal method, chemical vapor deposition (CVD), chemical vapor transport (CVT), molecular beam epitaxy (MBE). All these methods can be classified into two categories: top-down approaches, and bottom-up approaches.

1.2.1. Mechanical exfoliation

Mechanical exfoliation method was used by Geim and Novoselov to separate the graphene sheets from graphite flakes in 2004.[3] In this method, the bulk layered material is peeled off by using scotch tape and multilayer material remains on the tape. Multilayer material becomes thinner after repeating peeling among tapes.

Eventually, few-layer or even monolayer 2D material can be obtained by adhering the tape to a target substrate like silicon wafer. Taking advantage of the weak Van der Waals force between the two adjacent layers of 2D materials, the mechanical exfoliation method is relatively simple, fast, low-cost and has less destructive than other methods. After removing the tape residue, the few-layer or monolayer 2D materials obtained by this method have high quality and clean surface. However, due to the limited size of exfoliated flake and the absence of layer number controllability, the mechanical exfoliation method is not suitable for large-scale production.
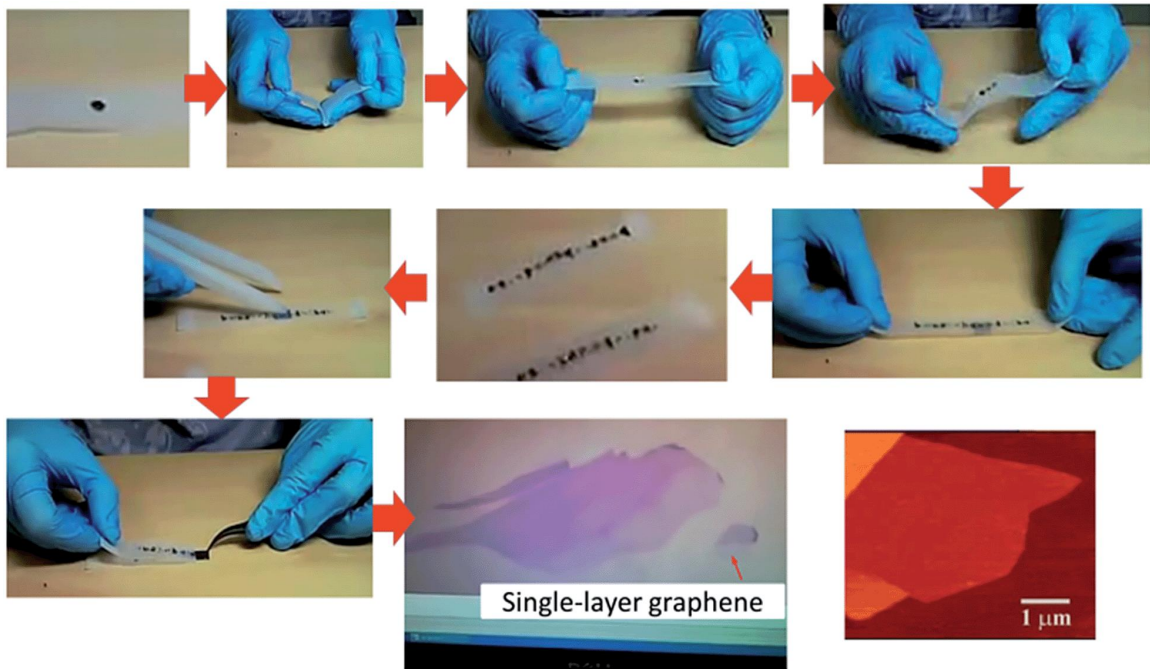
Figure 1-1 - An illustrative procedure of the Scotch-tape based micromechanical cleavage of highly ordered pyrolytic graphite (HOPG).[4]

1.2.2. Chemical vapor deposition (CVD)

The recent development of CVD technique has allowed successful production of 2D materials with large-scale, regular shape, uniform, and controllable thickness, greatly encouraging the utilization of 2D materials for practical device fabrications and other applications.

In the CVD process, a thin solid film is deposited onto a substrate via the chemical reactions of vapor species. A typical CVD setup consists of a gas delivery system, precursors, a reactor and a gas removal system, which is shown in Figure 1-2.

During the growth process, reactive gas species and precursor vapors are fed into the reactor by the gas delivery system. In the reactor, a chemical reaction takes place and the solid thin film is deposited onto substrates which were loaded previously. All the non-reacted gas and by-products are removed through the gas removal system.
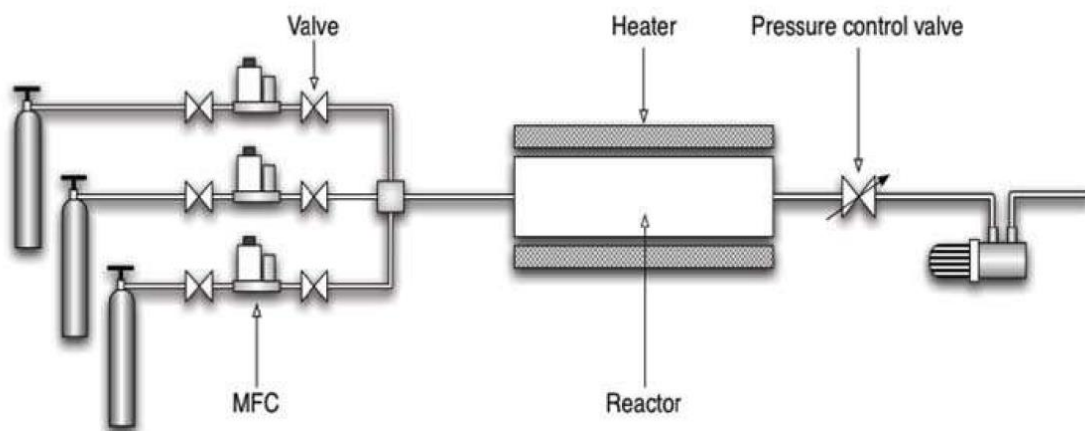
Figure 1-2 - The schematic diagram of a typical tube-furnace CVD system. Gas flows are regulated by mass flow controllers (MFCs) and fed into the reactor through a gas-distribution unit. Chemical deposition takes place in the reactor that is heated by the outside heaters. The exhaust gases are removed by vacuum pumps.[5]

1.2.3. Liquid exfoliation

Liquid exfoliation is another method to break the weak van der Waals bonds between layers to obtain thin 2D nanosheets. Layered bulk crystal can be exfoliated through sonication in organic solvents, such as isopropanol, dimethylformamide (DMF), N-methyl-pyrrolidinone (NMP). The matching of the surface tension between

the layer material and the solvent is very important to the efficiency of exfoliation. Liquid exfoliation makes it possible to produce a large number of 2D nanosheets in solution at low cost.
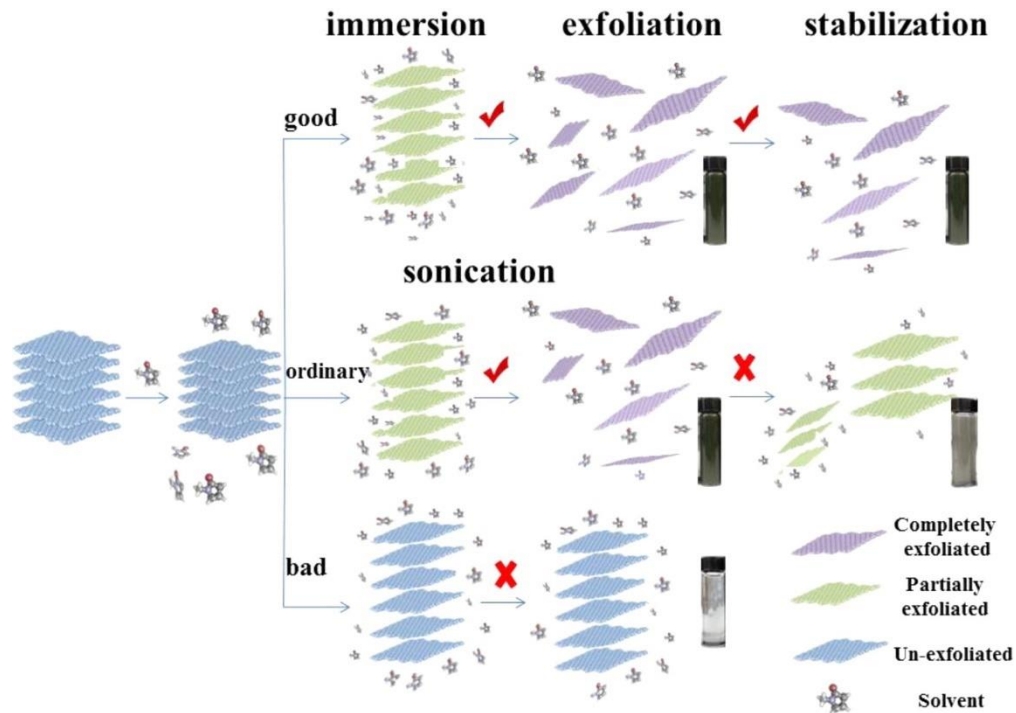
Figure 1-3 - Mechanism of liquid exfoliation process.[6]

1.3. Characterization methods

Although 2D material only has one or few atomic layers, it can be imaged under an optical microscope. In fact, graphene was distinguished by optical microscope when it was first discovered. The most common substrate that has been used to visualize single and few layers is SiO_2 on Si wafer. Due to the interference

effect from the reflection of the two surfaces of the SiO_2, 2D materials own color contrasts between flakes and the substrate.

Figure 1-4 shows the optical image for different thickness of graphene on SiO_2/Si substrates. The optical microscope is convenient and has been popular in the rough determination of the layer numbers.
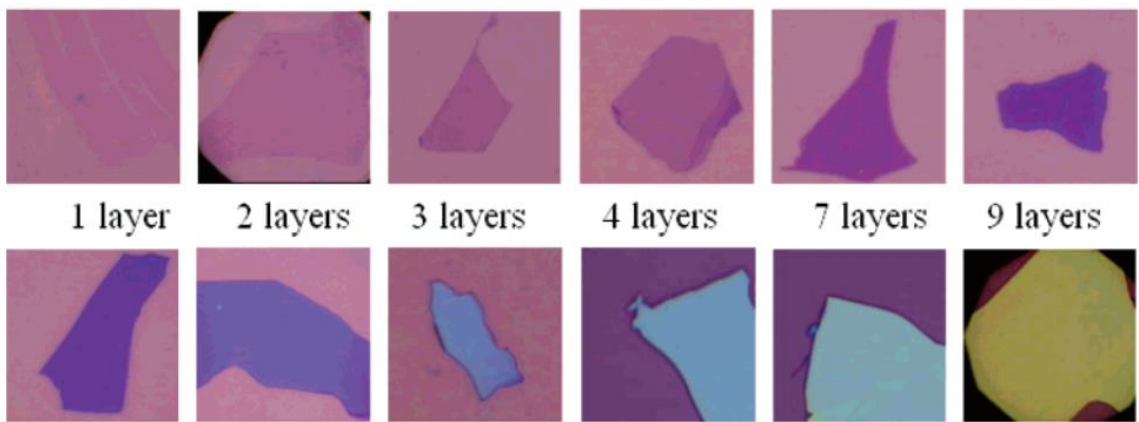
Figure 1-4 - The optical images of graphene sheets with different thicknesses.[7]

Raman spectroscopy relies on inelastic scattering of monochromatic light, providing valuable structural information about materials. When a laser is incident onto a sample, a small proportion of the scattered light might be shifted from the original laser wavelength. The difference between the incoming laser and scattered light indicates the information of vibrational modes, which are fingerprints of materials. In addition, due to differing interlayer interactions, Raman spectra vary

with the layer number of materials. The intensity and frequency of Raman peaks can be used to determine the thickness of 2D materials.

When a semiconductor is excited with a laser with photon absorptions, electron-hole pairs may undergo the reverse process, recombination of an optically created electron-hole pairs. This process is accompanied by the spontaneous emission of light, which is called photoluminescence (PL). It is required that the laser photon energy must be higher than the band gap. PL can be used to determine band gap, impurity levels, and detect defects.

Atomic force microscope (AFM) is a practical tool used to measure layer thickness. By approaching a sharp tip close to the sample surface, the electrostatic force between the top and the sample can be detected by the deflection of laser and transmitted into a photodiode detector.

Because electrons have a small de Broglie wavelength, electron microscopy techniques were invented to achieve higher spatial resolution than the optical microscope. Scanning electron microscopy (SEM) and transmission electron microscopy (TEM) are the two methods which are frequently used in 2D materials research. SEM is based on scattered elections, while TEM relies on transmitted electrons. SEM focuses on the surface, morphology, and composition of the sample. TEM seeks to see what is inside or beyond the surface, such as morphology, crystallization, layer sizes, interlayer stacking relationships, stress or even magnetic

domains. Last but not the least, SEM has a lower resolution of tens of nm, whereas TEM has a higher resolution of 1 nm or less.

X-ray diffraction (XRD) is a useful technique to determine the crystal phase and structure. X-ray is generated by a cathode ray tube, which then strikes toward the material. The periodic atomic structure of the material causes the incident X-rays to diffract into many specific directions. The angles and intensities of these diffracted X-rays are then collected and measured. Unit cell dimensions, geometry, the density of electrons within the crystal can be obtained from the angular positions of XRD peaks.

1.4. Typical 2D materials and their properties

1.4.1. Graphene

Graphene comprises a monolayer of hexagonal arranged sp^2 hybridized carbon atoms. It is the basic building materials for other allotropes of carbon, which can be wrapped up into 0D buckyballs rolled into 1D nanotubes or stacked into 3D graphite.[8]
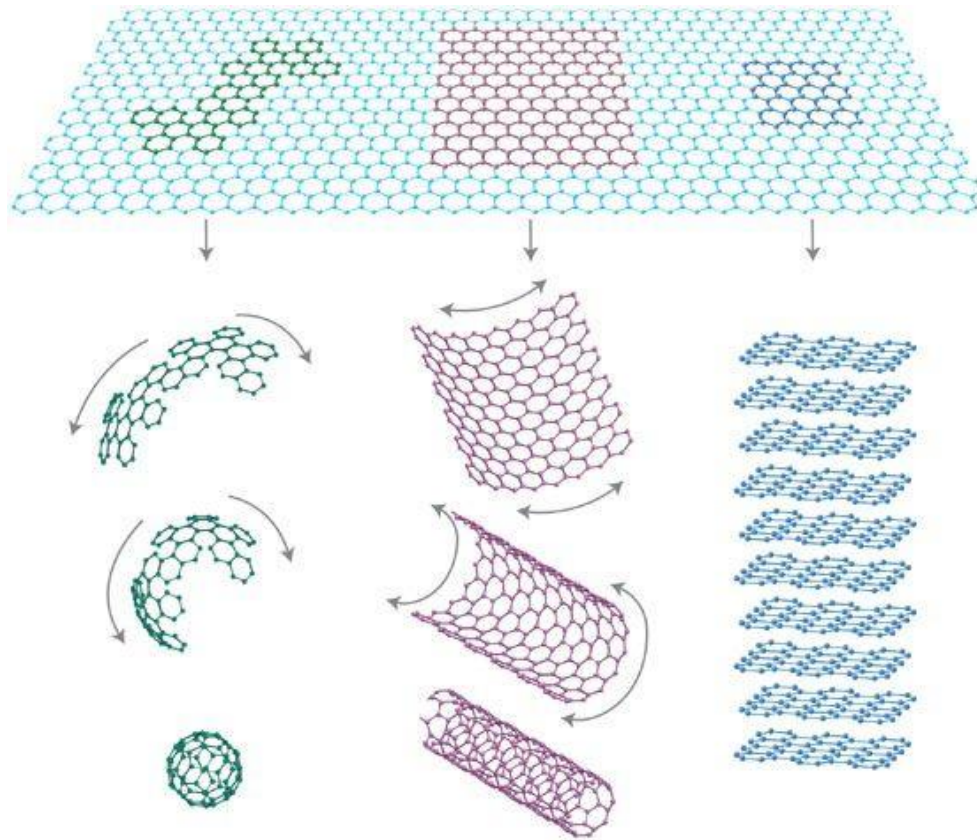
Figure 1-5 - Graphene is the mother of all other graphitic forms.[8]

There are two atoms in one graphene unit cell, which results in two conical points K and K', or Dirac points at the corners of Brillouin zone. The conductance band touches the valence band occurs at these two points, which makes graphene a zero-gap semiconductor, or semimetal. The band structures are responsible for most of graphene's notable electronic properties. Electrons from the top of the valence band can flow into the bottom of the conductance band even without thermal excitation. If the temperature is absolute zero, the conduction band has a certain concentration of electrons, while the valence band has equal concentration of holes.

Since the charge carriers act as quasi-particles or Dirac Fermions, graphene exhibits the half-integer quantum Hall effect (QHE) and the relativistic particle properties.
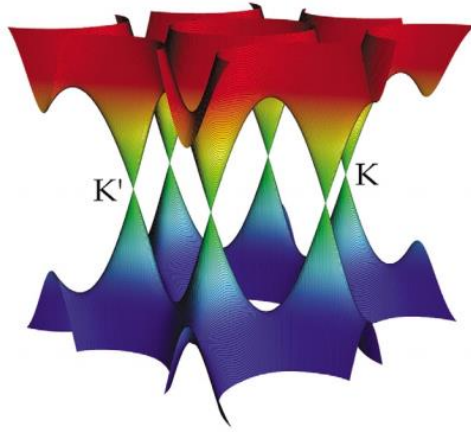
Figure 1-6 - Band structure of graphene.[9]

Graphene can display a concentration of charge carriers up to 10^{13} cm^{-2} and show remarkable electron mobility with reported values in excess of 15000 cm^2 V^{-1} s^{-1} even under ambient conditions.[1] Graphene also has excellent optical, mechanical and thermal properties. Monolayer graphene absorbs up to 2.3% of incident white light with less than 0.1% reflectance.[10] The thermal conductivity of graphene is in the order of 5300 W m^{-1} K^{-1}.[11] Graphene has an intrinsic tensile strength of 130.5 GPa and a Young's modulus of 1 Tpa.[12]

Raman spectra of monolayer graphene is featured by two main peaks, G, primary in-plane vibrational mode, and 2D, a second-order overtone of a different in-plane vibration D, as displayed in Figure 1-7. The shape and intensity of 2D peak

change with the thickness of graphene. D peak is not visible in pristine graphene due to crystal symmetries, which requires defect scattering to conserve momentum.
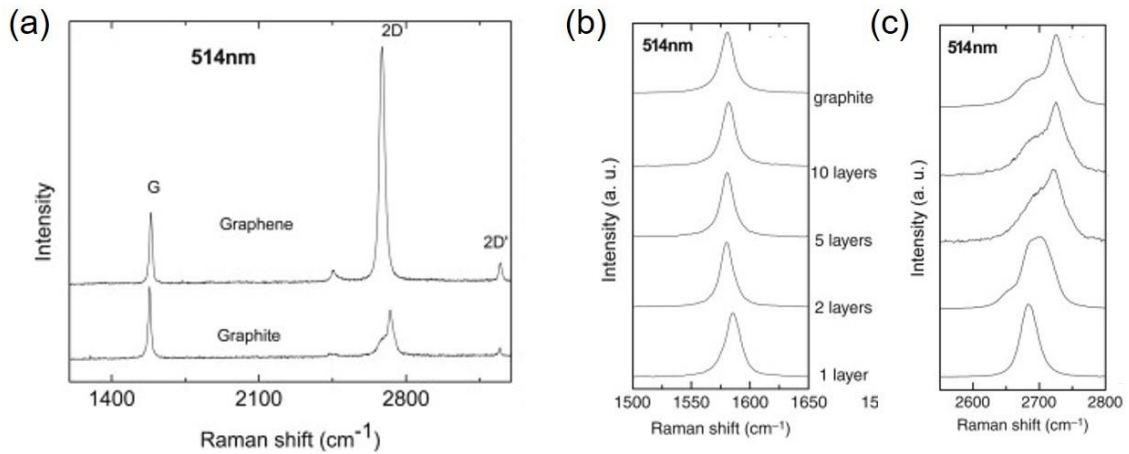
Figure 1-7 – (a) Raman spectra of graphene and graphite. Evolution of (b) G peak and (c) 2D peak as a function of layers. The excitation wavelength is 514 nm.[13]

Figure 1-8 shows the CVD furnace using for graphene growth in the lab. It has been reported that electropolishing can remove the chromium oxide layer on the commercial Cu foils and be beneficial to growing uniform and large graphene domains.[12] To synthesize monolayer graphene, a polished Cu foil is loaded into a small quartz tube, which is then inserted into a 2-inch quartz tube. The quartz tube is pumped down to 8×10^{-3} Torr by a mechanical pump. 15% H_2/Ar is used as the carrier gas, keeping the pressure at 1 Torr during the entire growth process. The furnace is heated up to 1000 ℃ in 20 min. The small quartz tube is moved toward the hot zone by using a magnet, in order to make the Cu foil annealed for another 20 min. After

that, 3.5 sccm methane is introduced into the quartz tube for 8 min. The small quartz tube is pulled out immediately after the valve of methane closes. The furnace is then shut off and cooled down to room temperature.
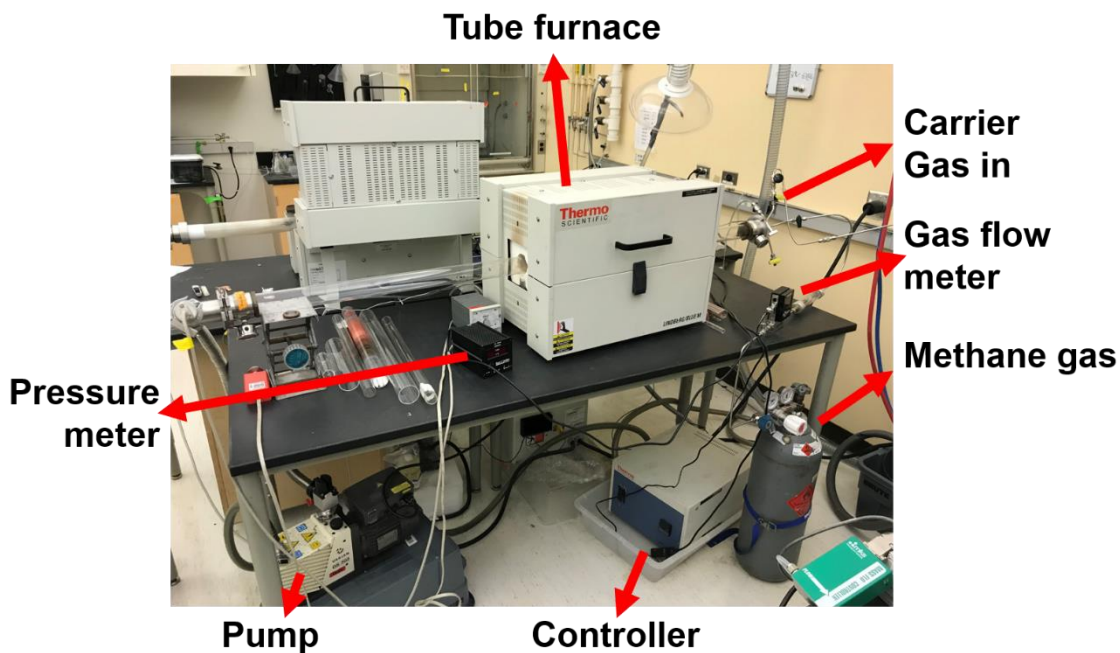
Figure 1-8 – Photograph of the CVD system for graphene synthesis

To synthesize multilayer graphene, Ni foil is used as the substrate. The growth process is similar, but the temperature is increased to 1100 °C, the reaction time is extended to 10 min, and the flow rate of methane is 20 sccm.

To transfer graphene onto other substrates, such as SiO_2/Si wafer, polymethyl methacrylate (PMMA)-assisted wet transfer method is adopted.[14] A layer of PMMA is first spin-coated onto graphene/Cu or graphene/Ni. The underlying metal then is

etched away by iron chloride (FeCl$_3$) solution. PMMA/graphene is washed with deionized (DI) water and transferred onto the target substrate. The PMMA layer can be dissolved in acetone and isopropanol (IPA).

1.4.2. Hexagonal boron nitride (h-BN)

h-BN is a compound consisting of equal numbers of boron and nitrogen atoms. The lattice constant values for h-BN are very close to the graphite lattice constant values, which are only 1.7% larger than graphene. The length of B-N bonds is 1.45 Å, while the distance between the centers of neighboring borazine (B$_3$N$_3$H$_6$) rings is 2.50 Å.[15] The spacing between two successive layers is 0.334 nm, which is similar to that of graphene.
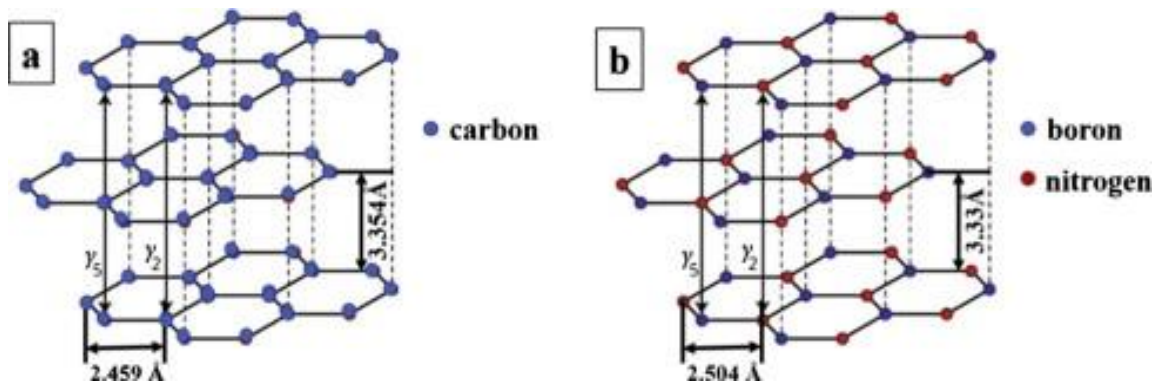
Figure 1-9 - Graphite (a) and hexagonal boron nitride (b) stacking sequence and lattice parameters.[16]

h-BN doesn't have any optical absorption in the visible region, which exhibits high transparency. h-BN has a very wide band gap (5.0-6.0 eV) with high breakdown

field. Therefore, h-BN can be used as dielectric substrates for electronic devices serving as spacers, protectors or gate layers. H-BN also has excellent chemical and thermal stability, high thermal conductivity, outstanding oxidation resistivity and low friction coefficient.

The primary Raman peak for h-BN is typically found in the region of 1366–1373 cm^{-1}. This peak originates from E_{2g} photon mode, which is analogous to the G peak of graphene. With the decreasing number of layers, the peak becomes weaker.
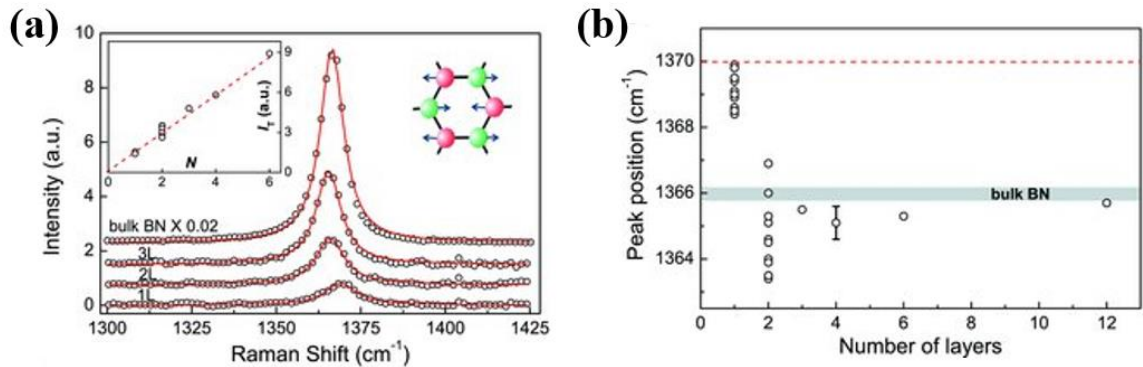
Figure 1-10 – (a) Raman spectra of h-BN. (b) Positions of the Raman peak for different thickness.[17]

Figure 1-11 shows the CVD furnace using for h-BN growth in the lab. The precursor is ammonia borane, which is placed upstream of the furnace. Electrical polished Cu foil is used as the substrate and inserted into a quartz tube. The quartz tube is pumped down to a low pressure in the order of 10^{-2} Torr before the valve of Ar/H$_2$ opens. The furnace is then heated to 1000 °C and the Cu foil is annealed at 1000

°C for 20 min. The ammonia borane is sublimed at ~80 °C with a heating belt to trigger the h-BN growth. The typical growth time for h-BN is 10 to 30 min.
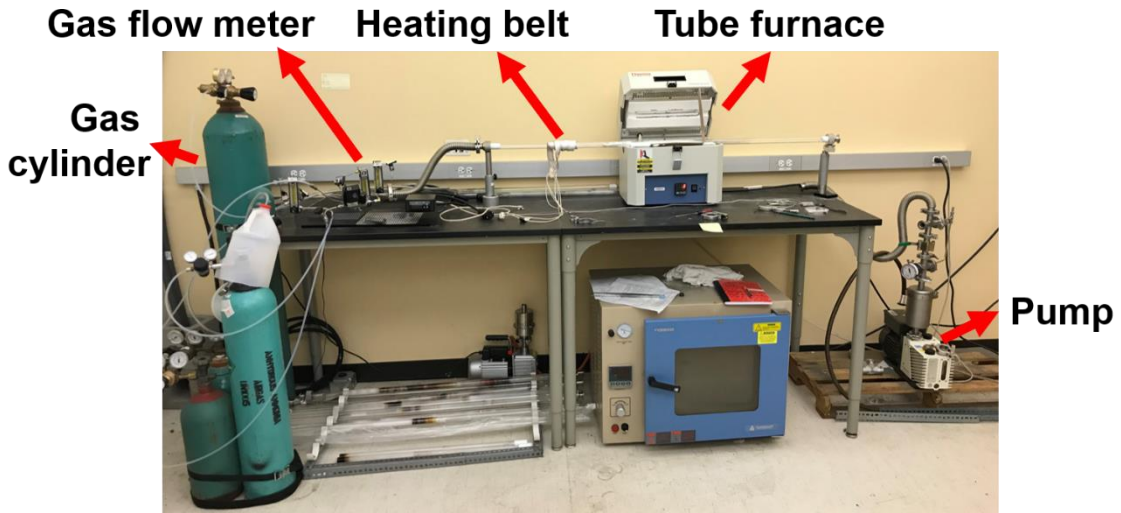
Figure 1-11 - Photograph of the CVD system for h-BN synthesis

1.4.3. Transition metal dichalcogenides (TMDs)

Transition metal dichalcogenides (TMDs) are in the form of MX_2, where M stands for the transition metal, such as Mo, W, Nb, Re, Ni, and V, X stands for chalcogens, such as S, Se, and Te. TMDs have strongly covalent bonded 2D X-M-X layers and weak interlayer Van der Waals interactions.

As graphene has a zero bandgap and h-BN has a large bandgap, TMDs own a wide range of bandgap covering all visible and infrared range. Most TMDs reveal direct bandgap in monolayer, whereas they are indirect bandgap in bulk form.
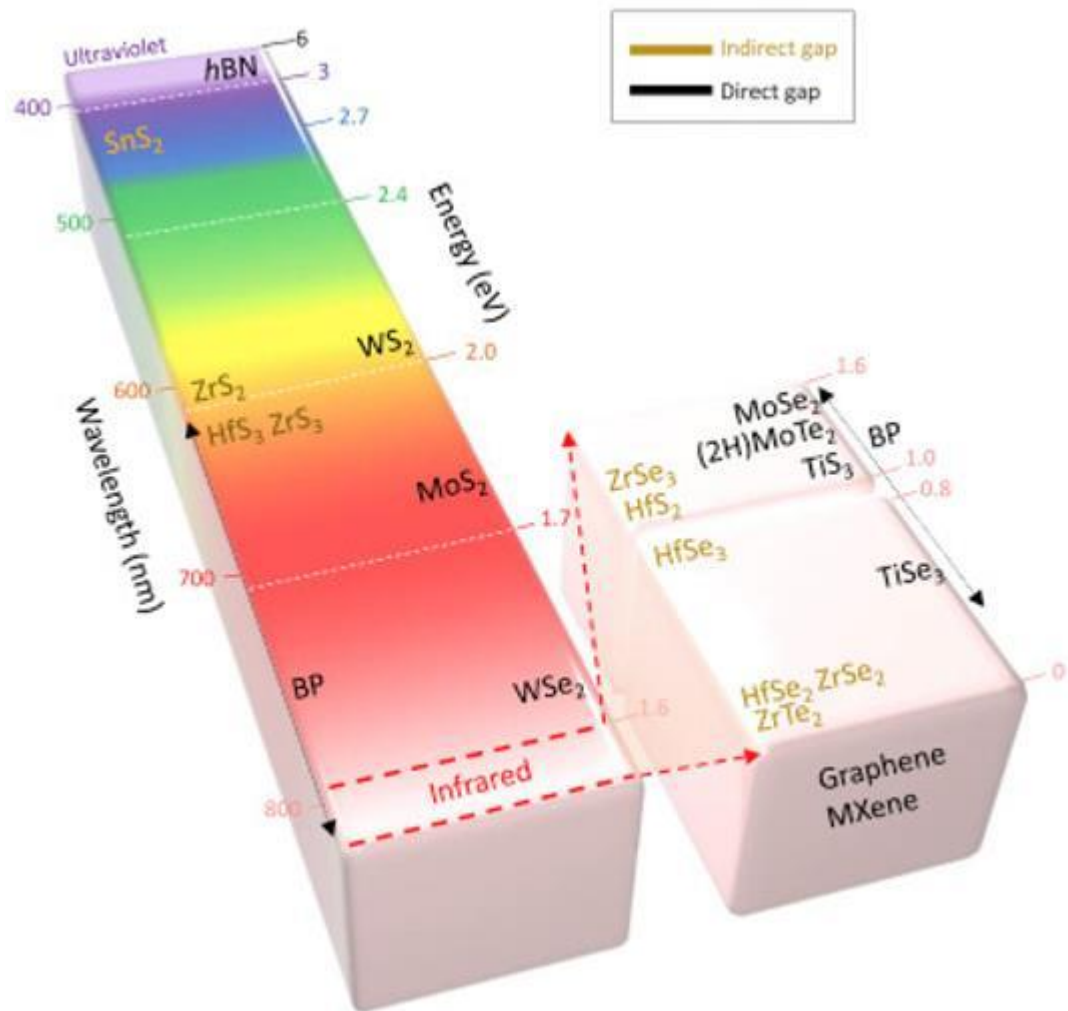
Figure 1-12 - Bandgap of 2D layered materials varying from zero band gap of graphene (white color) to a wide bandgap of h-BN. The color in the column is presenting the corresponding wavelength of bandgap.[18]

The structures of TMDs can be categorized as trigonal prismatic (hexagonal, H), octahedral (tetragonal, T) and distorted phase T'. Most TMDs have both metallic phase and semiconducting phase, the stable phase of which at room temperature is 2H phase.
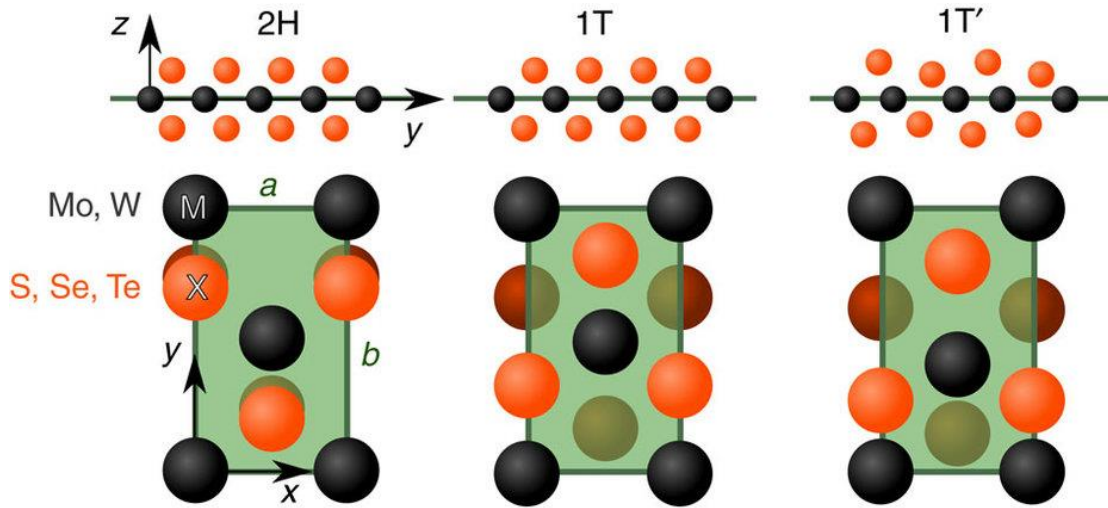
Figure 1-13 - The three crystalline phases of TMDs.[19]

The Raman spectra of bulk TMDs with 2H structure exhibits three active peaks at high frequencies, E_{1g}, E_{2g}^1 and A_{1g}. E_{1g} and E_{2g}^1 are in-plane modes, while A_{1g} is an out-of-plane mode. The in-plane modes shift to lower frequencies (or blue shift) and the out-of-plane mode shifts to higher frequencies (or redshift) with the increasing number of layers.

For example, for bulk MoS₂, the E_{2g}^1 peak is at 382 cm⁻¹ and the A_{1g} peak is at 407 cm⁻¹. For monolayer MoS₂, the E_{2g}^1 peak is at 385 cm⁻¹ and the A_{1g} peak is at 403 cm⁻¹. The frequency difference can be used to determine the layer number of MoS₂.
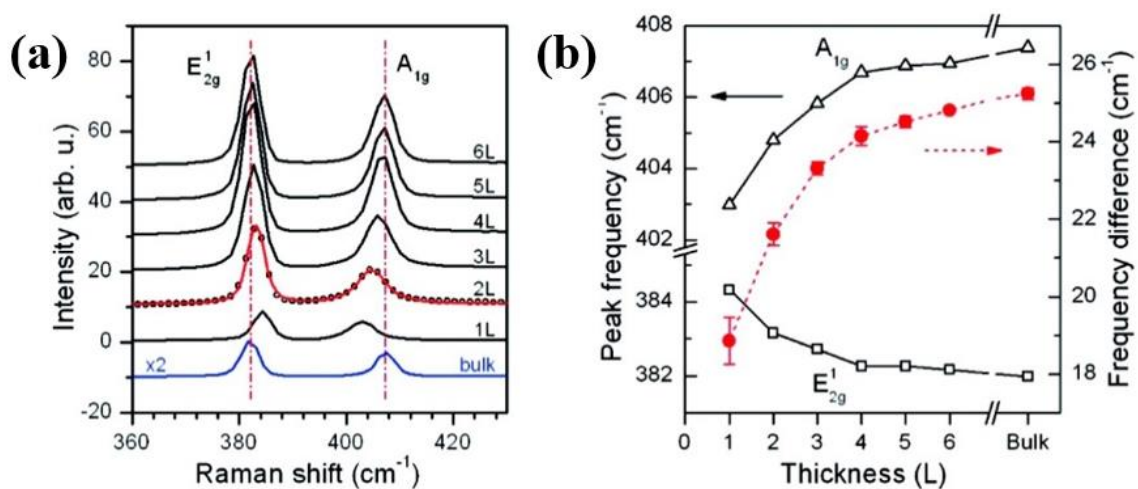
Figure 1-14 - (a) Raman spectra of MoS$_2$ with different thickness. (b) Frequencies of E_{2g}^1 and A_{1g} modes and their difference as a function of thickness.[20]

The transformation of MoSe$_2$ and WSe$_2$ from an indirect semiconductor in their bulk form to a direct semiconductor in their monolayers can be experimentally demonstrated by PL. As shown in Figure 1-15, the PL intensity increases with decreasing number of layers.
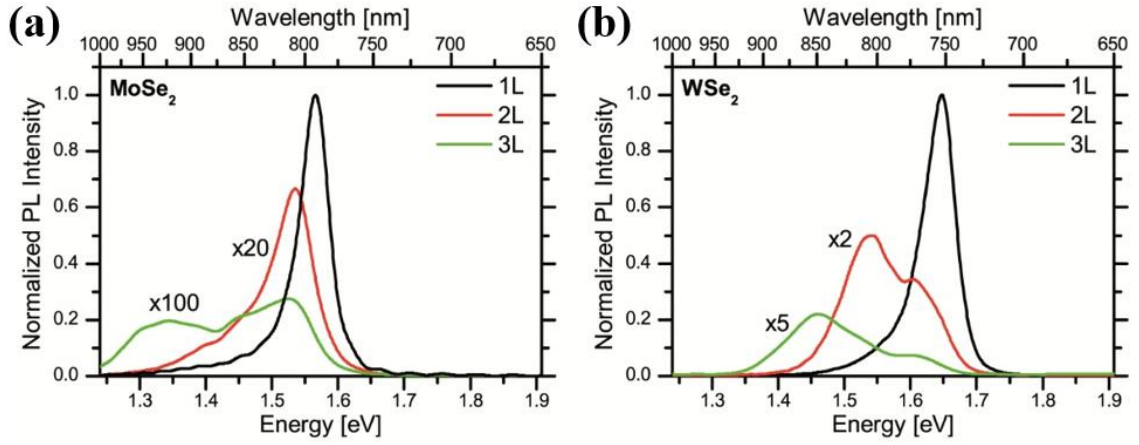
Figure 1-15 - (a) PL spectra of MoSe2 with different thickness. (b) PL spectra of WSe2 with different thickness.[21]

Figure 1-16 shows a schematic diagram of CVD synthesis of MoSe$_2$ or WSe$_2$. Molybdenum trioxide (MoO$_3$) or tungsten trioxide (WO$_3$) powder and selenium (Se) powder serve as precursors for MoSe$_2$ and WSe$_2$, respectively. SiO$_2$/Si wafer is placed face down at the center of the furnace. The furnace is heated to 750 °C (MoSe$_2$) or 900 °C (WSe$_2$) and held for 20 min with 15% H$_2$/Ar flowing as the carrier gas. The synthesis process for MoS$_2$ or WS$_2$ is similar to MoSe$_2$ or WSe$_2$, respectively. Se powers are replaced by S powers, the location of which need to be adjusted at the same time.
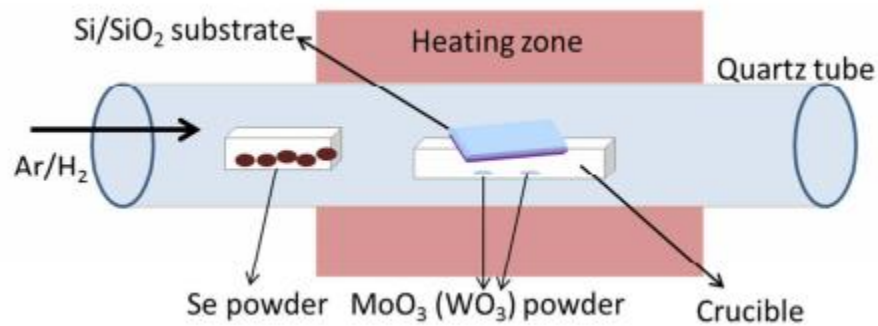
Figure 1-16 – Schematic of the CVD growth of MoSe₂ or WSe₂ setup.[22]

1.5. Applications

1.5.1. Electronic devices

Because 2D materials have atomic dimensions, smooth surface, and high flexibility, they are promising for next-generation electronics applications. Graphene was observed to have ultrahigh carrier mobility as the channel material in field emission transistors (FET).[3] TMD-based FETs exhibit high on/off ratio and high carrier mobility. Figure 1-17 shows a monolayer MoS_2 FET, which contains three parts: source-drain metal contacts, 2D material channel, and dielectric layer served as the gate electrode.
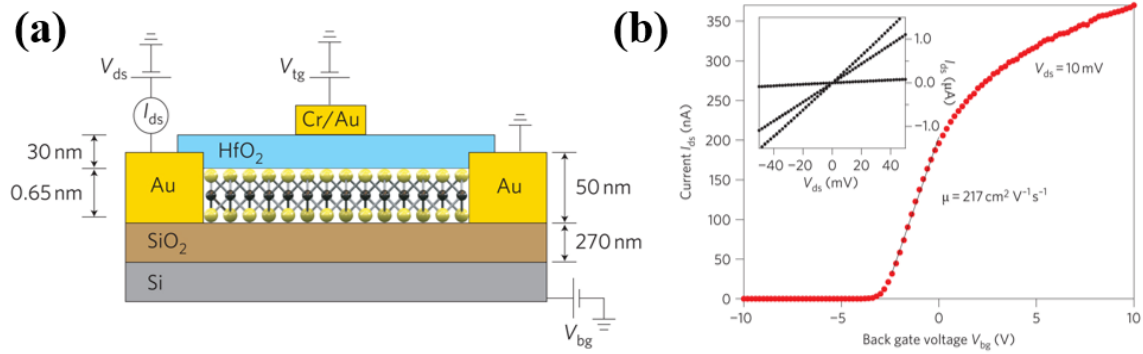
Figure 1-17 - (a) Cross-sectional view of the structure of a monolayer MoS$_2$ FET. (b) Room-temperature transfer characteristic for the FET with 10 mV applied bias voltage V$_{ds}$.[23]

In addition to serving as the channel material, graphene has also been demonstrated to be the promising electrode material.[24] Due to its optical transparency, high flexibility, excellent conductivity, graphene can be used in solar cells, organic light-emitting diodes, and nonvolatile memory devices. Besides, h-BN is a promising material as a dielectric layer or substrate for 2D electronic devices.[25]

1.5.2. Catalysis

Owing to their unique structural and electronic properties, some 2D materials show excellent performance in catalysis. They have been used in a variety of reactions, such as oxygen reduction reaction, oxygen evolution reaction, hydrogen evolution reaction (HER), water splitting and CO_2 activation.

Figure 1-18 indicates 1T MoS₂ nanosheets exhibit excellent catalytic activity toward the evolution of hydrogen. The activity of 2H MoS₂ is extremely reduced after partial oxidation, while 1T MoS₂ remains unaffected after oxidation.[26]
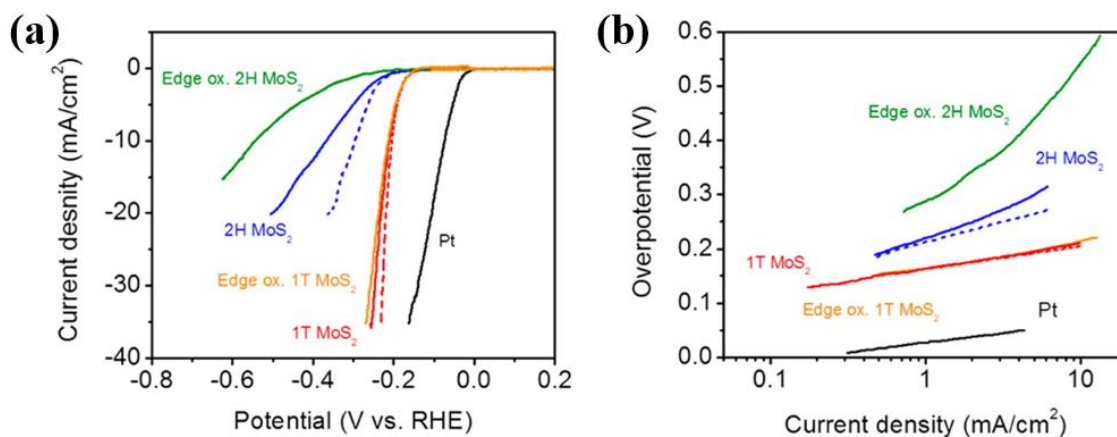
Figure 1-18 - HER activity of exfoliated MoS₂ nanosheets. (a) Polarization curves of 1T and 2H MoS₂ nanosheet electrodes before and after edge oxidation. (b) Corresponding Tafel plots obtained from the polarization curves.[26]

Researchers report that engineering defects, strains, crystal boundaries, and doping heteroatoms in 2D materials are two of the most effective ways to increase the number of active sites and thus to attain superior performance for electrocatalysis.[27]

1.5.3. Energy storage

With the increasing demand for energy, the development of reliable and renewable materials for energy storage is highly desirable. Due to their high surface-to-volume ratios, good conductivity, and excellent electrochemical behavior, 2D materials have been drawing researchers' attention in energy storage, such as batteries and supercapacitors.
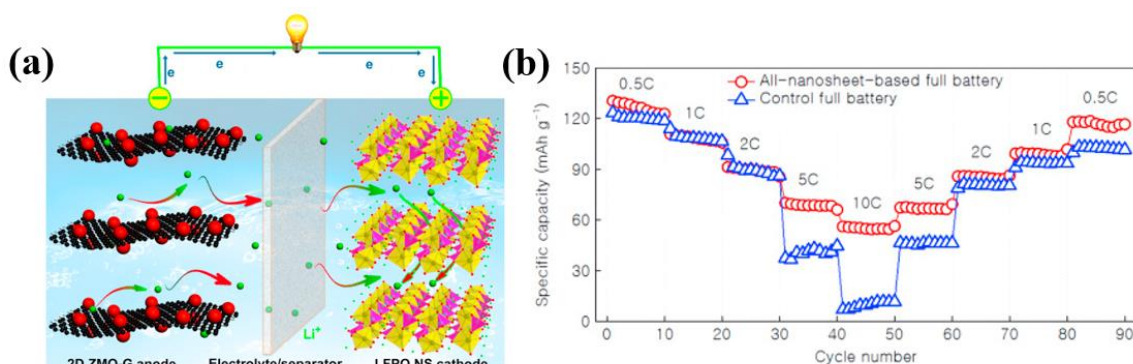
Figure 1-19 - (a) Schematic of an all-nanosheet-based full battery with ZnMn$_2$O$_4$-graphene hybrid nanosheet anode and LiFePO$_4$ nanosheet cathode. (b) This all-nanosheet-based full battery shows high rate capability and cycling stability.[28]

Because some 2D materials can accommodate more Li$^+$ ions during the Li$^+$ ion intercalation process, they have shown the potential to be the electrodes for Lithium-ion batteries. For example, Xiong et al.[28] fabricated an all-nanosheet-based full battery with ZnMn$_2$O$_4$-graphene hybrid nanosheet anode and LiFePO$_4$ nanosheet cathode, which shows high rate capability and mechanical flexibility (Figure 1-19).

In addition to these examples above, 2D materials have the potential to both enhance existing technologies and also create a wide range of new applications.

Chapter 2

Synthesis and Characterization of 2H and 1T' MoTe$_2$

2.1. Introduction

Molybdenum ditelluride (MoTe$_2$) belongs to the large family of 2D materials, specifically VI group TMDs, which has unique structures and interesting features.

MoTe$_2$ has four different crystal structures: hexagonal (2H phase or α-phase), octahedral (1T phase), monoclinic (1T' phase or β-phase), and orthorhombic (Td phase or γ phase).[29] The 2H structure in $\frac{P6_3}{mmc}$ space group, as described in the previous chapter, can be defined as sandwiches of three planes of 2D hexagonally packed atoms. The lattice constants of 2H MoTe$_2$ are a=3.519 Å, c=13.97 Å. The bond length of Mo-Mo is 3.52 Å, Mo-Te is 2. 71 Å. [30] When one of the 2H structure's Te layers is shifted, the Te atoms are in octahedral coordination around the Mo atoms and MoTe$_2$ becomes 1T phase. Because one of the optical phonon modes has an

imaginary vibrational frequency, the high-symmetry 1T structure is unstable, at least in the absence of external stabilizing influences. [19]

The 1T' structure is a monoclinic polymorph in $\frac{P2_1}{m}$. The coordination around the metal atom is slightly distorted octahedron of tellurium atoms, with the metal atoms displaced from the central position and making chains that run through the crystal in the crystallographic y direction.[30] The lattice parameters are a=6.330 Å, b=3.469 Å, c=13.89 Å, β=93°55'.[30]

A Td structure can be obtained by cooling the 1T' phase down to 247 K.[31] The Td phase shares the same in-plane crystal structure as the 1T' phase but has a vertical (90°) stacking and belongs to the non-centrosymmetric space group $P_{mn}2_1$.[29]
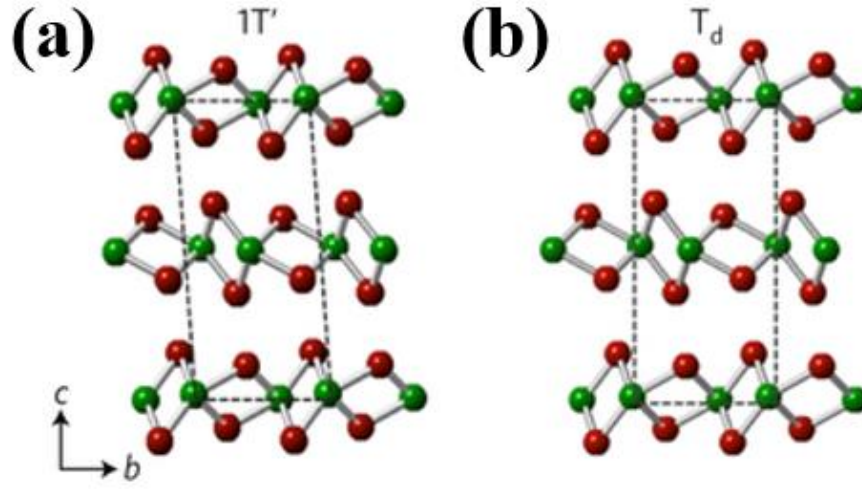
**Figure 2-1 - Crystal structures of MoTe2 in the 1T′ (a) and Td (b) phases.
Green balls are Mo atoms and red balls are Te atoms.[29]**

Figure 2-2 shows the calculated equilibrium relative energies of 2H, 1T and 1T'
phases of some TMDs. Compared to other TMDs, the energy difference between 2H
and 1T' MoTe2 is quite small, less than 0.1 eV per MoTe2 unit. Therefore, it is possible
to reversibly switch from to 2H phase to 1T' phase in specific conditions. Besides,
controllable synthesis of different phases of MoTe2 is likely to be achieved.
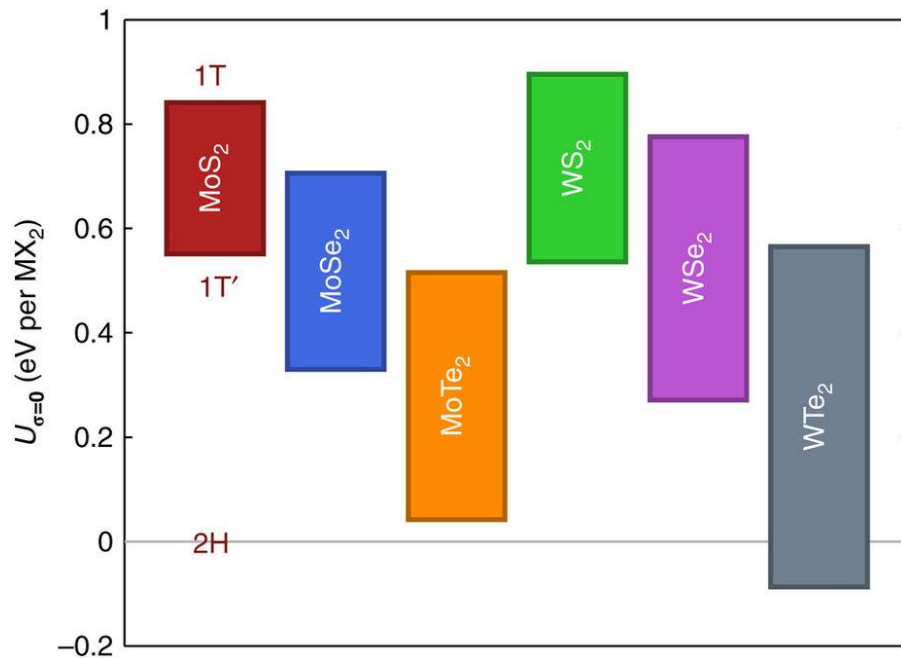
Figure 2-2 - Ground-state energy differences between monolayer phases of the some TMDs. The energy U is given per formula unit for 2H, 1T' and 1T phases.[19]

Bulk 2H MoTe$_2$ has an indirect band gap of ~1.0 eV, while monolayer 2H MoTe$_2$ is a semiconductor with a direct band gap of ~ 1.1 eV.[32] It has reported that 2H MoTe$_2$ is p-type semiconductor when prepared by using flux of tellurium. However, using bromine results in forming n-type semiconductor.[33]

2H MoTe$_2$ has a similar bandgap to Si (~1.1 eV), which makes it promising to be part of transistors and solar cells. It can expand the operating range of TMDs optoelectronic devices from visible to the near-infrared. Compared to MoS$_2$ and MoSe$_2$, the heavier element Te in 2H MoTe$_2$ leads to a strong spin-orbit coupling and

possibly to concomitantly longer decoherence times for exciton valley and spin indexes.[34] In addition, 2H MoTe$_2$ hold promise for use in logic transistors, charge density waves, superconductors, spintronics, and valley-optoelectronics.

1T' MoTe$_2$ is predicted to be a large gap quantum spin Hall insulator, which can be used in a topological field effect transistor to realize fast on/off switching by topological phase transition instead of carrier depletion. [35] It has been reported that 1T' MoTe$_2$ has a giant magnetoresistance (MR) 0f 16,000% in a magnetic field of 14T at 1.8 K in the bulk form.[36] Bulk 1T' MoTe$_2$ exhibits superconductivity with a transition temperature of 0.10 K.[37] The transition temperature can be raised to 8.2 K by applying external pressure at 11.7 GPa.[37]

Figure 2-3 shows two versions of Mo-Te phase diagram. (a) is from ASM Alloy Phase Diagram Database, drawn by Keum et al.[36] (b) is drawn by Predel et al.[38] by using results present in the literature.
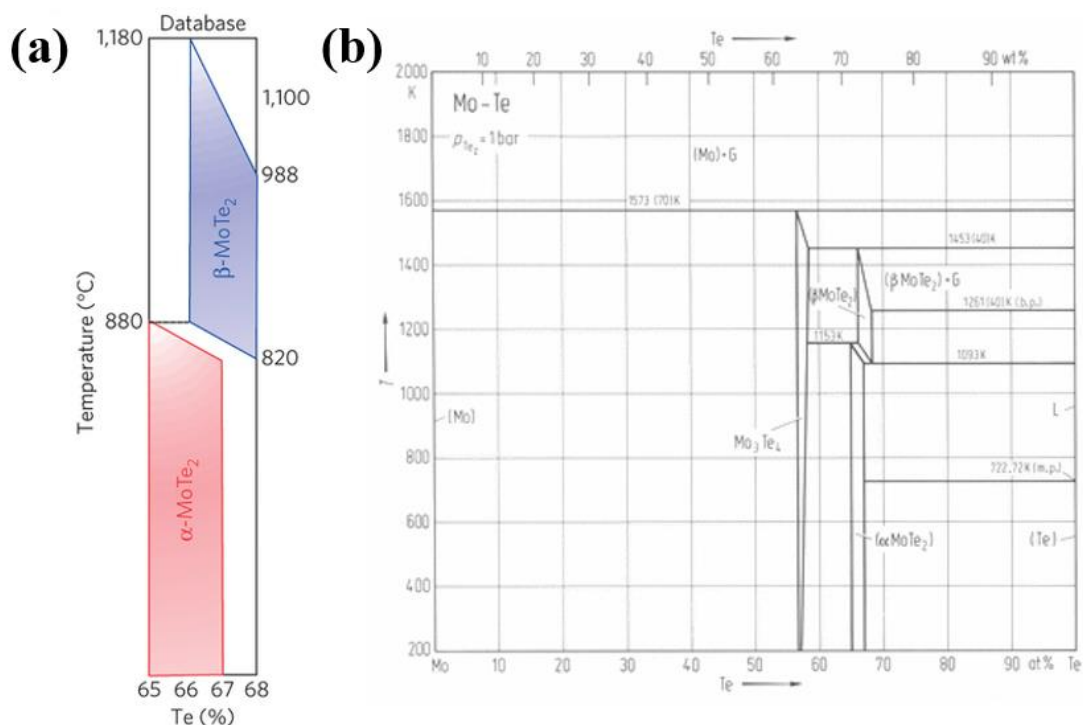
Figure 2-3 - Mo-Te phase diagrams. (a) is from ASM Alloy Phase Diagram Database, drawn by Keum et al. [36] (b) is drawn by Predel et al. [38] by using results present in the literature.

Both of the phase diagrams indicate that 2H MoTe2 is stable at relatively low temperature. The phase transition occurs and 1T' MoTe2 exits when the temperature is higher than ~800 °C. Besides, it can be noticed from Figure 2-3 (a) that when the concentration of Te becomes higher, the transition temperature turns lower.

Duerloo et al. [19] determined the phase diagrams of TMD monolayers as a function of strain by using density functional theory (DFT) and DFT-based methods. Figure 2-4 shows that monolayer TMD can be mechanically coupled to a substrate

with friction, making the lattice parameters a and b independently controlled. [19] For bulk materials, only compression can cause large elastic deformations. But large elastic deformations in monolayer TMDs can be achieved by tensile strain. [19]
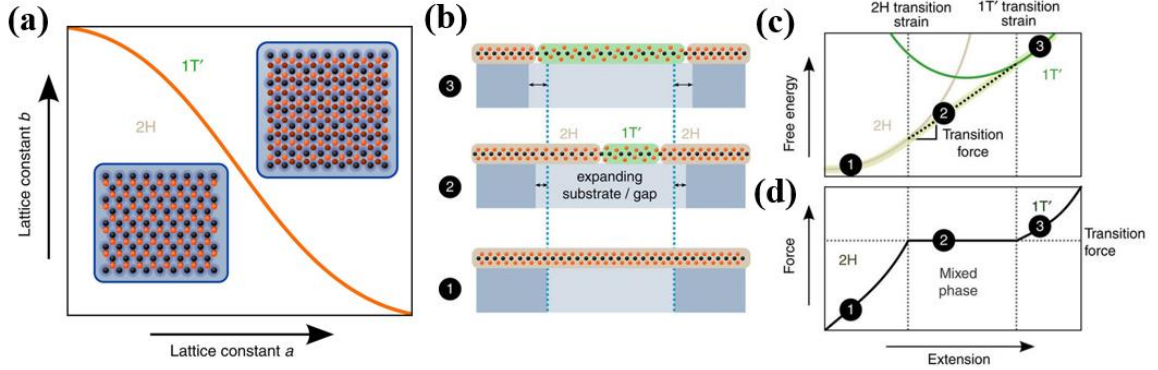
Figure 2-4 - (a) Substrate-based application of strain to a TMD monolayer. (b) (c) (d) Phase coexistence under an applied force or extension. [19]

Figure 2-4 (b) (c) (d) show a progress in which a tensile mechanical deformation expands a region of the TMD monolayer and cause the phase transition. In the beginning, the 2H phase deforms elastically and no phase transition is observed. Beyond some critical strain in step 2, 2H and 1T' phases are coexisting in mechanical equilibrium. In the end, the mechanically induced phase transition completes and the entire TMD monolayer is 1T' phase. [19] It is predicted that $MoTe_2$ may transform under equibiaxial tensile strains of <1.5% under appropriate constraints, while most TMDs need 10-15%.[19]

In addition to applying strains, Zhou et al. [39] found that atomic adsorption generally favors 1T' phase, while molecular adsorption induces 2H phase. By introducing gasses during the growth or cooling process, it may be possible to bias the grown $MoTe_2$ toward 2H or 1T' phase. [39]

Li et al. [40] reported that electrostatic gating may induce 2H to 1T' phase transition in TMD monolayer. If the dielectric layers are chosen appropriately, a gate voltage of several volts can drive the phase transition. [40] This theory was verified by Wang et al. [41], who fabricated a $MoTe_2$-based ionic liquid (DEME-TFSI) field effect transistor (Figure 2-5). The doping level of ionic liquid is one order of magnitude higher than that of a solid gate. It was observed that the Raman modes of 2H phase gradually disappeared and 1T' phase modes appeared as the gate bias changed from 0 V to 4.4 V.
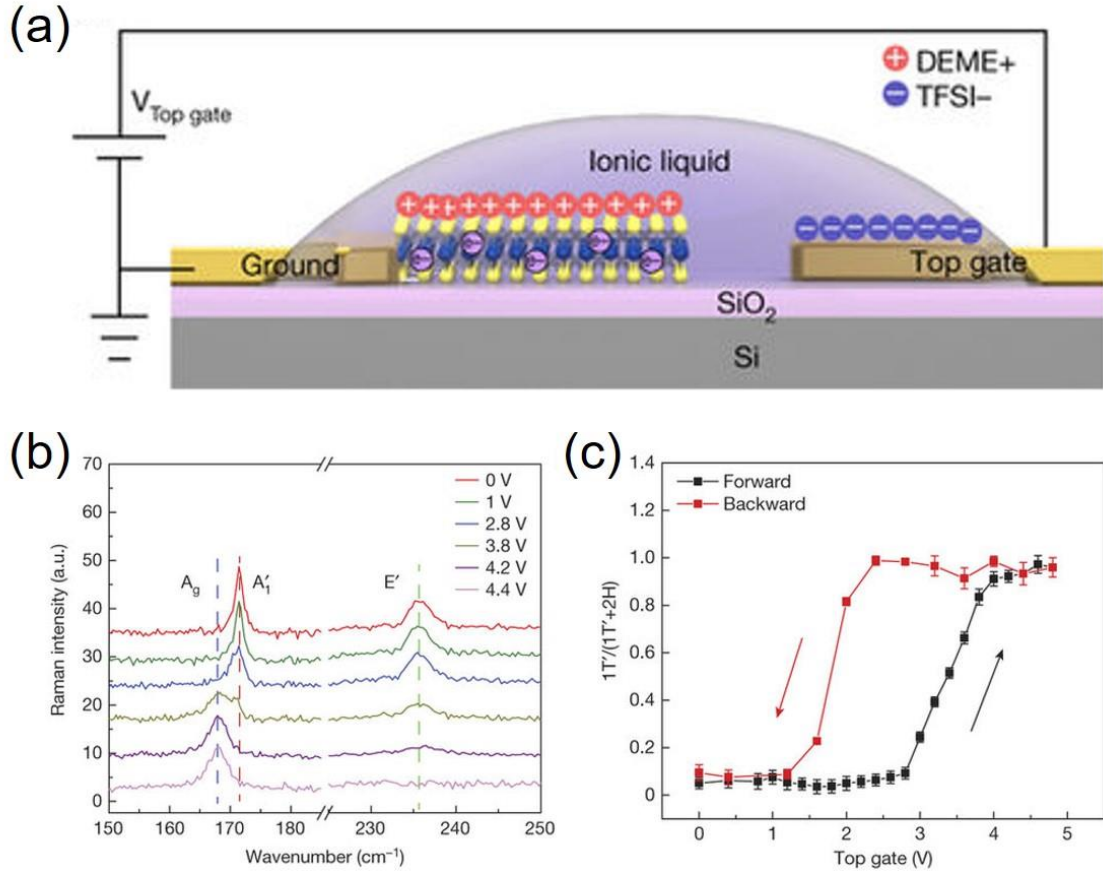
Figure 2-5 – (a) Schematics of a monolayer MoTe$_2$ field effect transistor. (b) Raman spectra of the 2H to 1T' phase transition in monolayer MoTe$_2$ under electrostatic bias. (c) Gate-dependent Raman intensity ratios.[41]

Cho et al. [42] successfully drive a MoTe$_2$ flake transforming from 2H phase to 1T' phase by using laser irradiation. The laser-driven phase patterning can also fabricate a heterophase homojunction.[42] Figure 2-6 shows the schematic of the process.
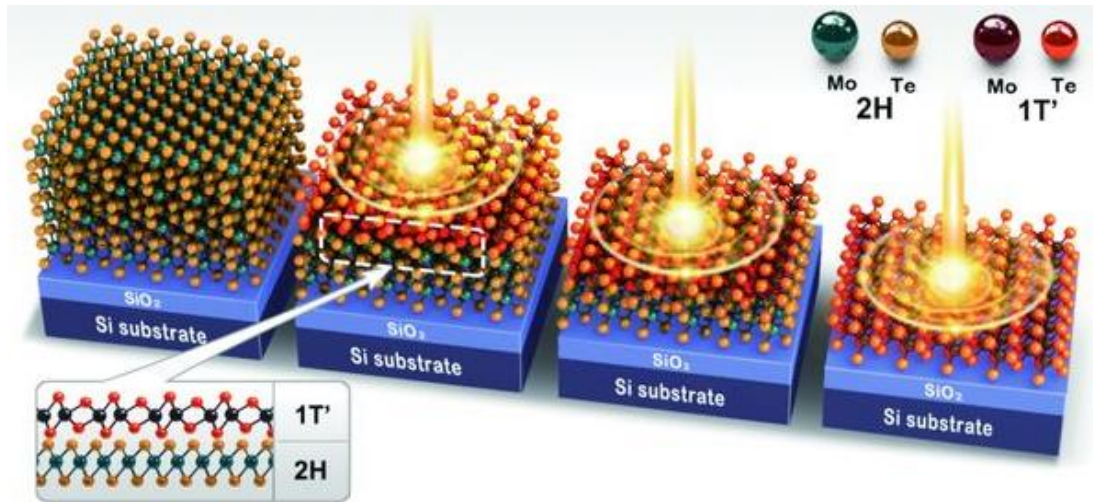
Figure 2-6 - Schematic of the laser-irradiation process.[42]

People have been using CVD method to synthesize 2D materials by metal or metal oxide deposition and subsequent reaction with S or Se. For example, Zhan et al. [43] grew few-layer MoS_2 by sulfurization of a thin Mo film. Song et al. [44] synthesized WS_2 nanosheets through the sulfurization of WO_3 film. Woods et al. [45] used the similar method to fabricate MoS_2/WS_2 layered heterostructure by one-step synthesis.

Figure 2-7 (a) and (b) show a typical growth schematic. Figure 2-7 (c) and (d) indicate morphologies of the samples.
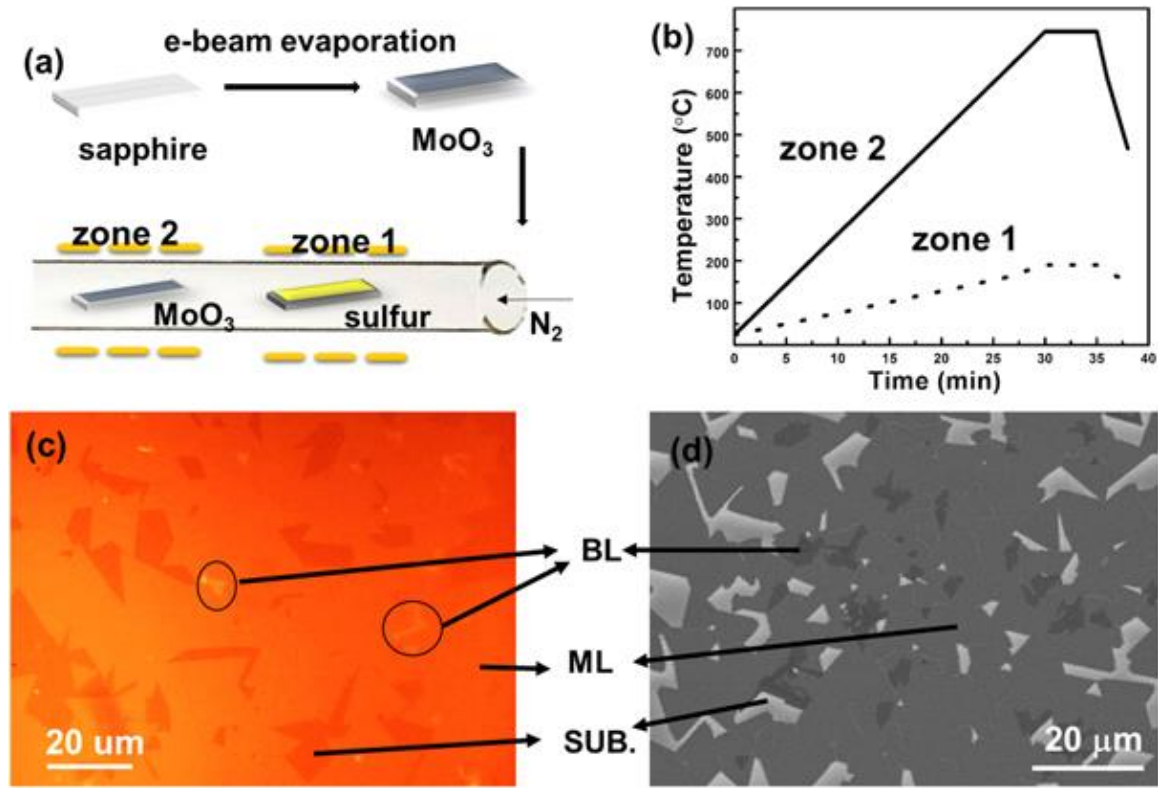
Figure 2-7 - (a) A schematic of the growth setup of MoS$_2$. (b) The heating profiles for the two zones. (c) Optical microscope and (d) scanning electron microscope (SEM) images of an unoptimized MoS$_2$ film. Monolayer (ML), bilayer (BL) and substrate (SUB) areas are marked. [46]

This method has couples of advantages. Firstly, a large continued film of TMDs can be synthesized by this method, which makes it possible to use TMDs for wafer-scale devices or other applications. Second, the thickness of as-grown TMDs can be well-controlled, which is mainly determined by the thickness of metal or metal oxide film. Third, the substrate has less effect on the growth. People have successfully used SiO$_2$/Si[43], sapphire[46], MgO[47], etc.

2.2. Synthesis

Two-dimensional MoTe$_2$ films are synthesized by tellurizing Mo thin film in a tube furnace, as illustrated in Figure 2-8 (a). 3 nm molybdenum (Mo) films are prepared by e-beam evaporation of Mo on a pre-cleaned SiO$_2$/Si substrate. During tellurization, the substrate is placed inside a ceramic crucible at the center of the furnace. Another ceramic crucible containing Te powder is placed upstream relative to the gas flow direction. Carrier gas H$_2$/Ar (15% H$_2$) with a flow rate of 50 SCCM is maintained during the whole growth process. The furnace is first purged by the carrier gas for 20 min and then heated up to the reaction temperature at a rate of 50 °C/min. The temperature is maintained for a specific duration of growth before cooling down to 500 °C. Once the temperature was below 500 °C, the lid of the furnace is opened to increase the cooling rate. By employing different reaction temperatures and times, we have synthesized large-area, high-quality MoTe$_2$ samples and achieved phase. Pure 2H, 1T' MoTe$_2$ films as well as mixed 1T'-2H MoTe$_2$ are successfully synthesized. The optical image in Figure 2-8 (b) shows a Mo film, 2H MoTe$_2$, 1T' MoTe$_2$, and 2H/1T' mixed-phase MoTe$_2$ from left to right respectively, all on SiO$_2$/Si substrate. It can also be seen that two phases of MoTe$_2$ are visually distinctive.
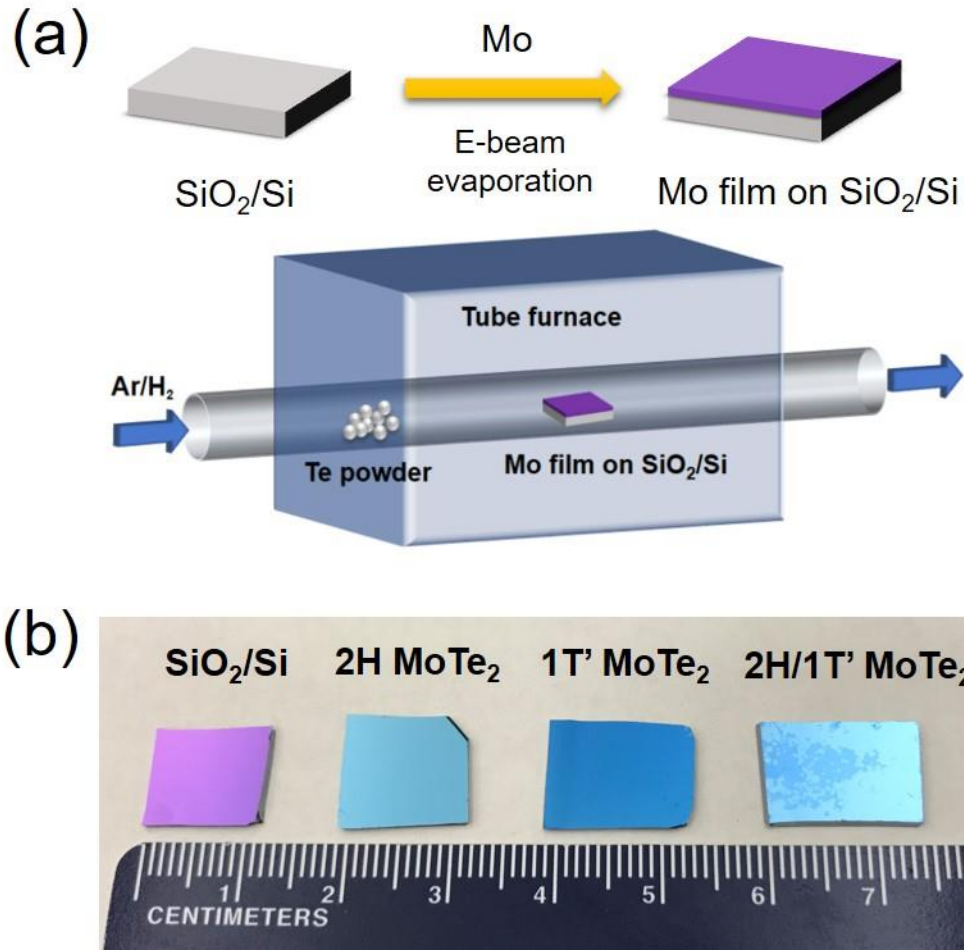
Figure 2-8 – (a) Schematic illustration of the synthesis process. (b)) An optical image of bare SiO$_2$/Si, pure 2H MoTe$_2$, pure 1T' MoTe$_2$, and mixed phased 2H/1T' MoTe$_2$ (from left to right).

To shed light on the phase control process, reaction temperature and growth time have been studied. We observe that pure 2H MoTe$_2$ is formed after a 2-hour reaction at 700 °C, while pure 1T' MoTe$_2$ is obtained after a 2-hour reaction at 800 °C. We have carried out a systematic study of the effect of the temperature and reaction

time on the MoTe$_2$ phase, and the results are demonstrated in Figure 2-9 and Figure 2-10. Optical images of the samples with controlled growth temperature from 600 °C to 800 °C and a fixed time of 2 hours are presented in Figure 2-9. Mixed-phase MoTe$_2$ is observed at 600 °C and 650 °C initially. When the temperature is increased to 700 °C, 2H phase starts to dominate, forming pure 2H MoTe$_2$ at 700 °C. However, both 2H and 1T' phases are observed when the temperature is further increased to 750 °C, which indicates the 2H phase to 1T' phase transition has begun. When the temperature reaches 800 °C, pure 1T' MoTe$_2$ film is obtained.
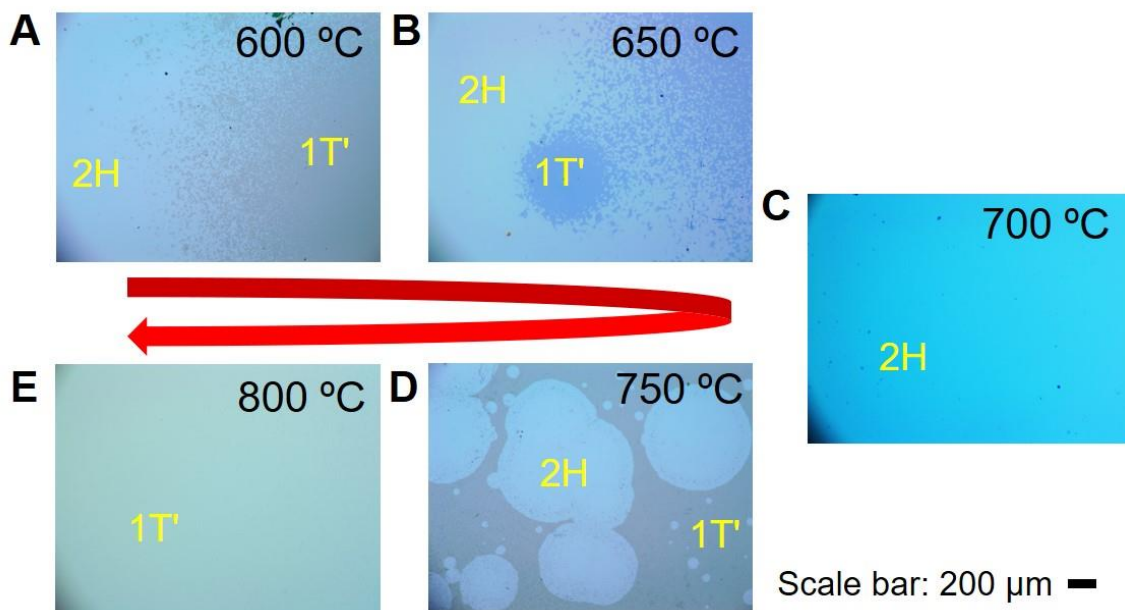
Figure 2-9 - Optical images of MoTe$_2$ films grown at controlled temperature (A) 600 °C, (B) 650 °C, (C) 700 °C, (D) 750 °C, (E) 800 °C, with a fixed time of 2 hours.

Figure 2-10 displays optical images of the samples with controlled reaction time from 1 hour to 3 hours, with the temperature fixed at 700 °C. Similarly, mixed phase MoTe$_2$ is first formed after a 1-hour synthesis, followed by a phase transition to 100% 2H MoTe$_2$ when the reaction time increases to 2 hours. At a 3-hour growth time, mixed phase MoTe$_2$ appears again.
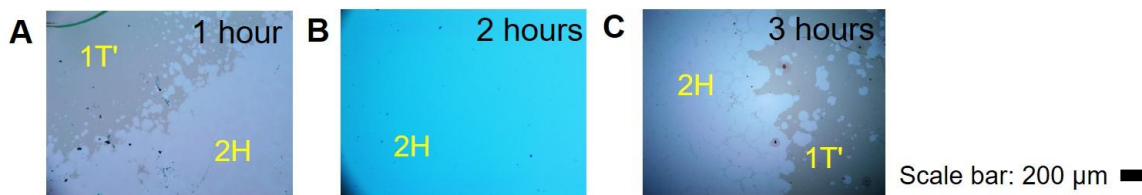
Figure 2-10 - Optical images of MoTe$_2$ films with controlled reaction time (A) 1 hour, (B) 2hours, (C) 3 hours, with the temperature fixed at 700 °C.

The 1T'-2H-1T' transition has been reported previously,[48,49] the mechanism of which can be attributed to strain and Te vacancy. [19,42] The 1T' phase is stable only under a certain tensile strain condition, while 2H phase is stable without strain.[19] The 1T' phase is formed initially because a large strain is created as the Mo film reacts with Te atoms and expands to MoTe$_2$. At low temperature or short growth time, the tellurization is incomplete, leaving unreacted Mo in the sample.[48] As the growth time or the reaction temperature increases, the strain might be released due to higher Te vapor concentration completing the tellurization process, transforming 1T' phase to 2H phase. The reversible 2H-1T' transition is observed when the temperature or the growth time further increases. This can be attributed to the small energy difference between these two phases. According to the experiments above, temperature and reaction time can determine the phase of the MoTe$_2$ film.

2.3. Characterization

As-synthesized MoTe$_2$ is characterized by Raman spectroscopy using a 532 nm excitation laser. 2H and 1T' phases of MoTe$_2$ give two distinct Raman patterns, which are presented in Figure 2-11 (a). The Raman-active modes of E_{1g} ($\sim$118 cm^{-1}), A_{1g} ($\sim$172 cm^{-1}), E_{2g}^1 ($\sim$232 cm^{-1}), and B_{2g}^1 ($\sim$287 cm^{-1}) are observed in 2H MoTe$_2$. E_{2g}^1 and E_{1g} are in-plane modes, while A_{1g} and B_{2g}^1 are out-of-plane modes.[50] For 1T' MoTe$_2$, the Raman-active modes of A_u ($\sim$108 cm^{-1}), A_g ($\sim$127 cm^{-1}), B_g ($\sim$161 cm^{-1}), and A_g ($\sim$256 cm^{-1}) are observed. All the peaks observed are consistent with previous reports, [48,50–52] suggesting both 2H and 1T' MoTe$_2$ films have been successfully synthesized. E_{2g}^1 ($\sim$232 cm^{-1}) and B_g ($\sim$161 cm^{-1}) are the prominent peaks of 2H MoTe$_2$ and 1T' MoTe$_2$, respectively. The dominant peaks from one phase are fully suppressed in the Raman spectra of the other phase, indicating MoTe$_2$ can be grown phase pure.

X-ray diffraction (XRD) patterns of 2H and 1T' MoTe$_2$ are shown in Figure 2-11 (b), where sharp-peaks from the (002), (004), (006), and (008) planes are detected. The high intensity of the peaks suggests that the 2H MoTe$_2$ film is highly oriented where the vdW planes are parallel to the plane of the substrate,[53] and the sample is free from contamination of other phases. It can be observed that the 2θ angles of these peaks of 2H MoTe$_2$ are slightly smaller than those of 1T' MoTe$_2$, indicating the average distance in the *c* direction of 2H MoTe$_2$ is larger than that of 1T' MoTe$_2$, according to Bragg's law. Figure 2-11 (c) shows that the (002) peak of 2H MoTe$_2$ and 1T' MoTe$_2$

occurs at 12.64° and 12.87°, respectively. From Bragg' law, the inter-planar distance for those phases are calculated to be 7.00 Å and 6.88 Å, which is consistent with previous results.[36,37,48,54]
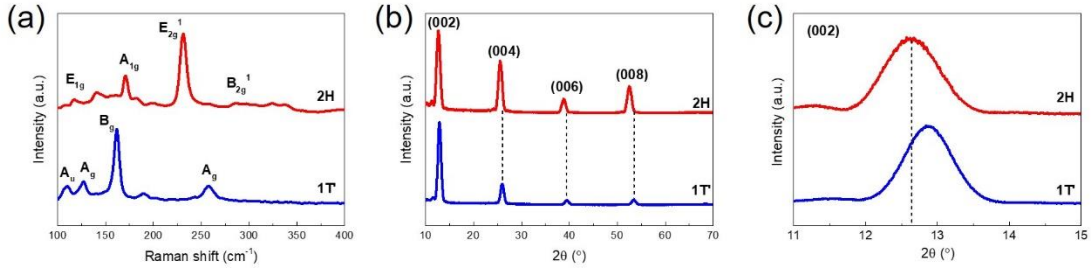
Figure 2-11 – (a) Raman spectra, (b) (c) XRD patterns of 2H and 1T' MoTe$_2$.

The thickness of pure 2H MoTe$_2$ and pure 1T' MoTe$_2$ films are characterized by atomic force microscopy (AFM), as shown in Figure 2-12 (a) and (b) across scratches. Both phases are measured to be around 10 nm thick. Figure 2-12 (c) shows an optical image of a region containing both 2H and 1T' phase. AFM measurements are conducted near the interface between two phases as displayed in Figure 2-12 (d) and (e). No significant difference between these two phases is observed, which confirms that 2H and 1T' MoTe$_2$ have a very similar thickness and surface morphology. AFM measurements also demonstrate that the MoTe$_2$ can be grown homogenously.
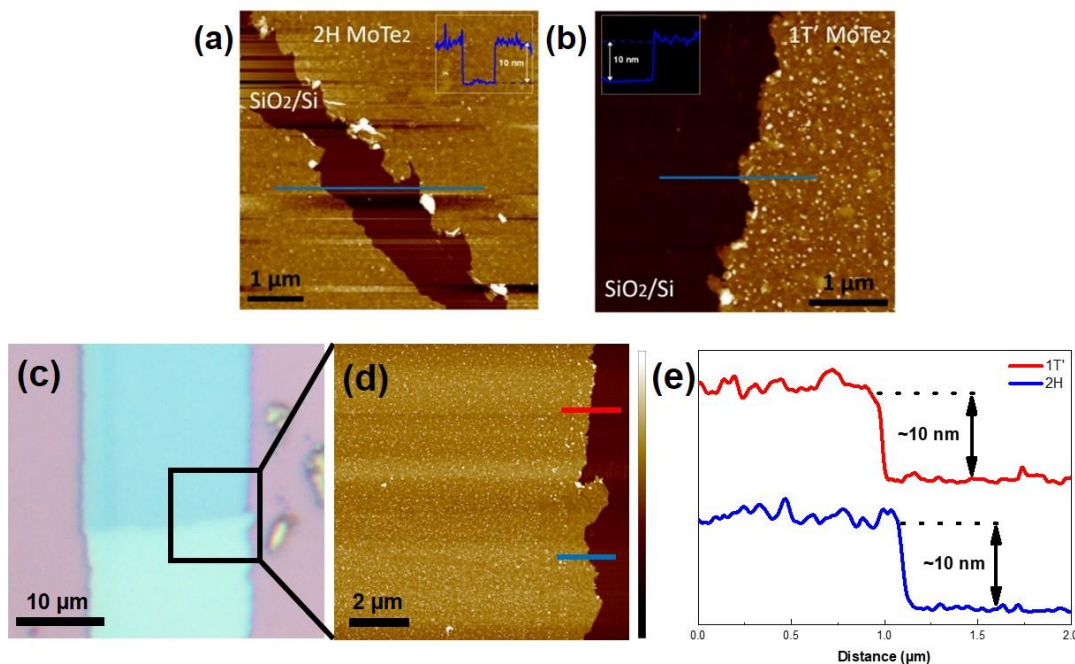
**Figure 2-12 - AFM height images of MoTe$_2$ films. (a) 2H MoTe$_2$ and (b) 1T'
MoTe$_2$. Inset: height profiles along the blue lines in (a) and (b), respectively,
showing both of 1T' and 2H MoTe$_2$ have a thickness of ~10 nm. (c) An optical
image of 2H/1T' MoTe$_2$ in-plane heterostructure. (d) AFM height image of a
square region in (c). (e) Height profiles along the red and blue lines,
respectively, showing both of 1T' and 2H regions have a thickness of ~10 nm.**

X-ray photoelectron spectroscopy (XPS) spectra of Mo 3d and Te 3d of 2H
MoTe$_2$ and 1T' MoTe$_2$ are displayed in Figure 2-13, respectively. The main peaks of
2H MoTe$_2$ are observed at 228.5 eV (Mo 3d$_{5/2}$), 231.6 eV (Mo 3d$_{3/2}$), 573.1 eV (Te
3d$_{5/2}$) and 583.5 eV (Te 3d$_{3/2}$). The main peaks of 1T' MoTe$_2$ are observed at 228.1 eV
(Mo 3d$_{5/2}$), 231.3 eV (Mo 3d$_{3/2}$), 572.8 eV (Te 3d$_{5/2}$) and 583.1 eV (Te 3d$_{3/2}$). It can be
seen that the 2H phase has a higher binding energy compared with 1T' phase. The

atomic ratio of Mo: Te is 1:2.1 for 2H MoTe₂, and 1:1.9 for 1T' MoTe₂. These results

indicate that both 2H MoTe₂ and 1T' MoTe₂ are stoichiometric, while 1T' MoTe₂ has a

slight Te deficiency.[49,55,56]
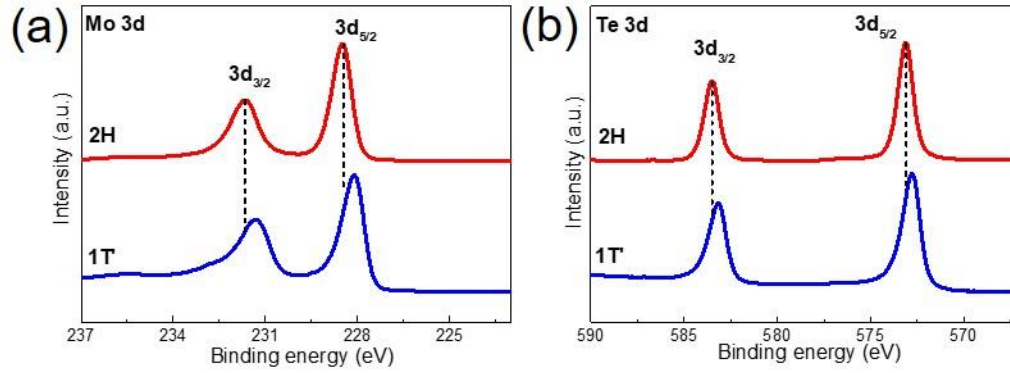
Figure 2-13 – (a) (b) XPS spectra of 2H (red) and 1T' (blue) MoTe₂.

To investigate the in-plane heterostructure of 2H/1T' MoTe₂, Raman intensity

mapping is conducted near the interface. A square region of 50 × 50 μm was selected

for Raman mapping in Figure 2-14 (a). Raman spectra collected from the left area

shows only 2H MoTe₂ peaks, while the right area shows only 1T' MoTe₂ peaks. Raman

intensity mapping using the 2H MoTe₂ E_{2g}^1 mode at 232 cm^{-1} (Figure 2-14 (b)) and

the 1T' MoTe₂ B_g mode at 161 cm^{-1} (Figure 2-14 (c)) demonstrates the spatial

distribution of 2H/1T' MoTe₂ heterostructure. The match between Raman mapping

and optical images suggests that we can distinguish these 2H and 1T' phases by their

optical contrast. SEM images of the heterostructure are illustrated in Figure 2-14 (d)

and (e), which also imply that a sharp interface has been formed. The contrast

between 2H and 1T' MoTe$_2$ can be attributed to their different electrical conductivities.
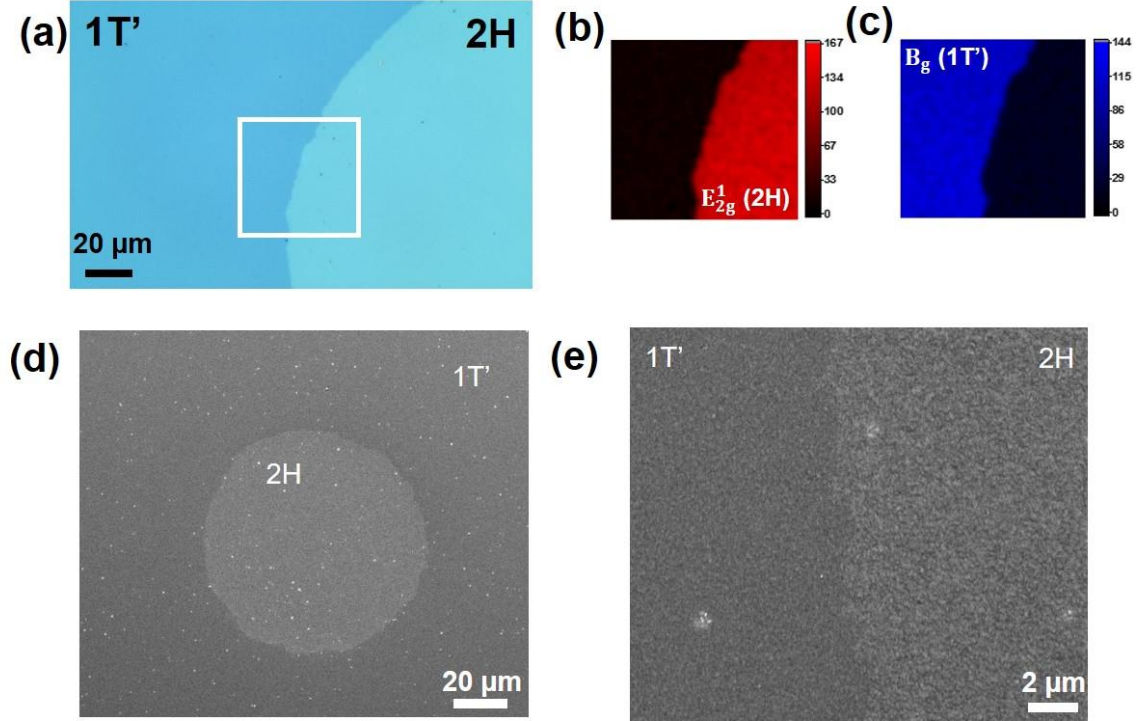
Figure 2-14 – (a)-(c) Raman intensity mapping and optical properties measurement of MoTe$_2$. (a) An optical image of the 2H/1T' interface and Raman intensity maps at (b) 232 cm $^{-1}$ (E$_{2g}^1$ mode of 2H phase) and (v) 161 cm $^{-1}$ (B$_g$ mode of 1T' phase). (d)(e) SEM images of 2H/1T' MoTe$_2$ in-plane heterostructure. (d) 2H region has higher brightness than 1T' region, which can be explained by their different electrical conductivities. 2H MoTe$_2$ is less conductive so that the accumulation of static electric charges on the surface

causes the charging effect. (e) High-magnification image reveals the sharp interface of 2H/1T' MoTe₂ in-plane heterostructure.

To study the optical properties of MoTe₂, Mo films are deposited on a sapphire substrate by e-beam evaporation, followed by the synthesis process described previously. Sapphire substrates are used for optical measurement because they transmit a high proportion of visible and infrared light. Figure 2-15 shows the Raman spectra of MoTe₂ grown on sapphire.
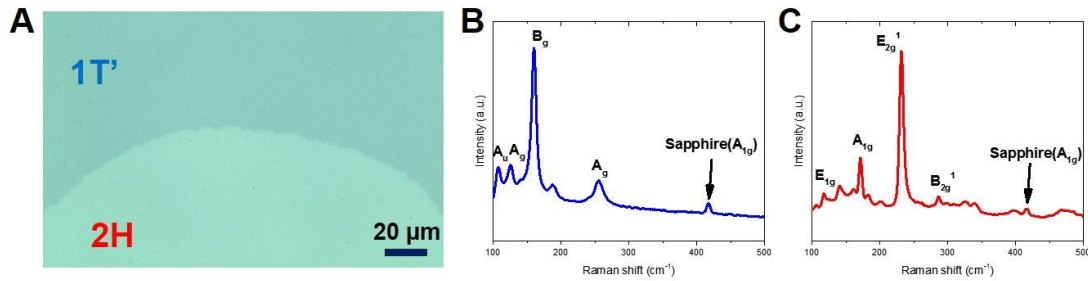
Figure 2-15 - MoTe₂ films on sapphire. (A) Optical image of 2H/1T' MoTe₂ in-plane heterostructure on sapphire, indicating that two phases are still visually distinctive. Raman spectra of (B) 1T' MoTe₂ and (C) 2H MoTe₂. In addition to the Raman modes of MoTe₂, sapphire A₁g peak can be also detected at 417 cm⁻¹.

The optical spectra from the visible to the near-infrared for 2H MoTe₂ and 1T' MoTe₂ are displayed in Figure 2-16. The main peaks of 2H MoTe₂ are at 1174 nm (1.05 eV), 721 nm (1.72 eV), and 496 nm (2.50 eV). These peaks are associated with transitions in different parts of the Brillouin zone.[32] The lowest direct optical

transition at the κ-point contributes to the excitonic peak, which has been proven to be very close to the emission peak.[57] There is a small step around 850 nm in all the curves, which is generated from lamp switching by ultraviolet-visible (UV-vis) spectrophotometry. Aside from the lamp artifact, the 1T' $MoTe_2$ spectrum does not show any peaks. The absorption measurement indicates that CVD-grown 2H $MoTe_2$ has an optical gap of 1.05 eV, while 1T' $MoTe_2$ does not show any absorption peak from 400 nm to 1400 nm.
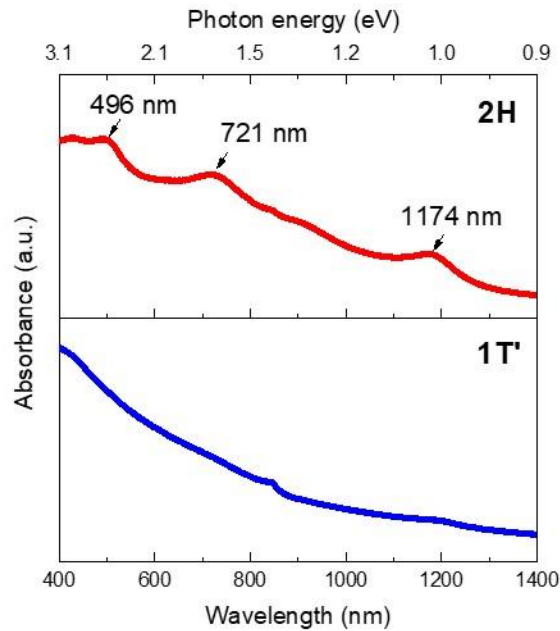
Figure 2-16 - Absorbance in the visible to near-infrared of 2H and 1T' $MoTe_2$

Furthermore, we explored the micro-scale optical transmission and absorption spectra of $MoTe_2$ samples by using Micro-Extinction Spectroscopy (MExS). Figure 2-17 (a) shows an optical image of $MoTe_2$ on sapphire, where 2H

phase, 1T' phase, and sapphire regions are indicated. The total integrated transmission intensity mapping of the same regions acquired by MExS is displayed in Figure 2-17 (b). The 1T' phase has around 20% larger total integrated transmission intensity than the 2H phase, while sapphire has the highest transmission. All the regions demonstrate uniform transmission strength throughout, which can be easily distinguished by the significant intensity differences among them.

An absorbance study is conducted across the 2H/1T' $MoTe_2$ interface, where the spectrum at each pixel along the arrow in Figure 2-17 (b) is retrieved from the MExS datacube output. Figure 2-17 (c) shows the evolution of the absorbance spectra collected from 1T' phase to 2H phase, where transmission intensity has been converted to absorbance. The first pixel is in the 1T' phase region and no absorption peak is observed (blue curve). The last spectra (red curve) is collected in the 2H phase region, which has two peaks and higher absorbance intensity than the spectra taken from the 1T' region. The two peaks are located at 495 nm and 715 nm, which are close to the previous measurement on pure 2H $MoTe_2$.[32] The evolution of absorbance spectra collected from 1T' phase to 2H phase clearly shows the different optical properties between these two phases.
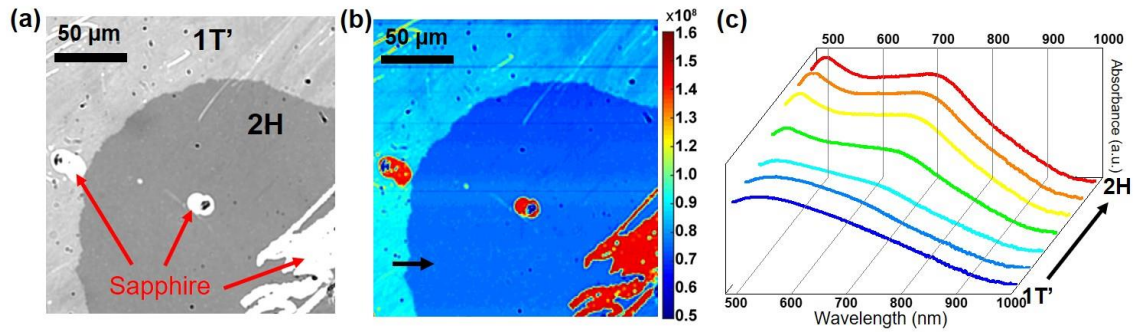
Figure 2-17 - (a) An optical image of 2H/1T' MoTe₂ in-plane heterostructure grown on sapphire. (b) A transmission intensity map of the same region in (a). (d) The evolution of absorbance spectra collected from 1T' phase (blue) to 2H phase (red).

The crystallographic configuration of MoTe₂ films is characterized by electron microscopy. MoTe₂ films grown on SiO₂/Si are transferred onto lacey carbon TEM grids using a PMMA assisted transfer method with hydrofluoric acid (HF) as the etchant. High-resolution transmission electron microscopy (HRTEM) images of the MoTe₂ films and their corresponding fast Fourier transforms (FFTs) are shown in Figure 2-18, with the hexagonal 2H phase in Figure 2-18 (a) and (b) and the monoclinic 1T' phase in Figure 2-18 (c) and (d). The interface between the two phases in the lateral heterostructures is investigated further with aberration-corrected scanning transmission electron microscopy (STEM). Figure 2-18 (e) show a defocused (low-magnification) STEM Ronchigram of the interface between 2H and 1T' MoTe₂ regions. The difference between the two samples can be observed even at low magnifications, due to the fact that in the transferred one a large number of

breaks and discontinuities are present in the 1T' region while the 2H region stays relatively continuous. A high magnification STEM image of the 2H/1T' interface is shown in Figure 2-18 (f). While the thickness of the heterostructures (~10 nm) and carbon contamination on the surface prevent direct imaging of the atomic structure of the interface, the spatial resolution is high enough to observe the interface region and the crystal structure on either side of the interface. Figure 2-18 (g) shows the FFT from the region on the 2H side highlighted by the blue box, and Figure 2-18 (h) shows the FFT from the 1T' region highlighted by the red box. The two FFTs show the same hexagonal and monoclinic structure observed in the reference images in Figure 2-18 (b) and (d), indicating that the heterostructure is single crystal on either side of the interface and that the two crystal phases interface directly.
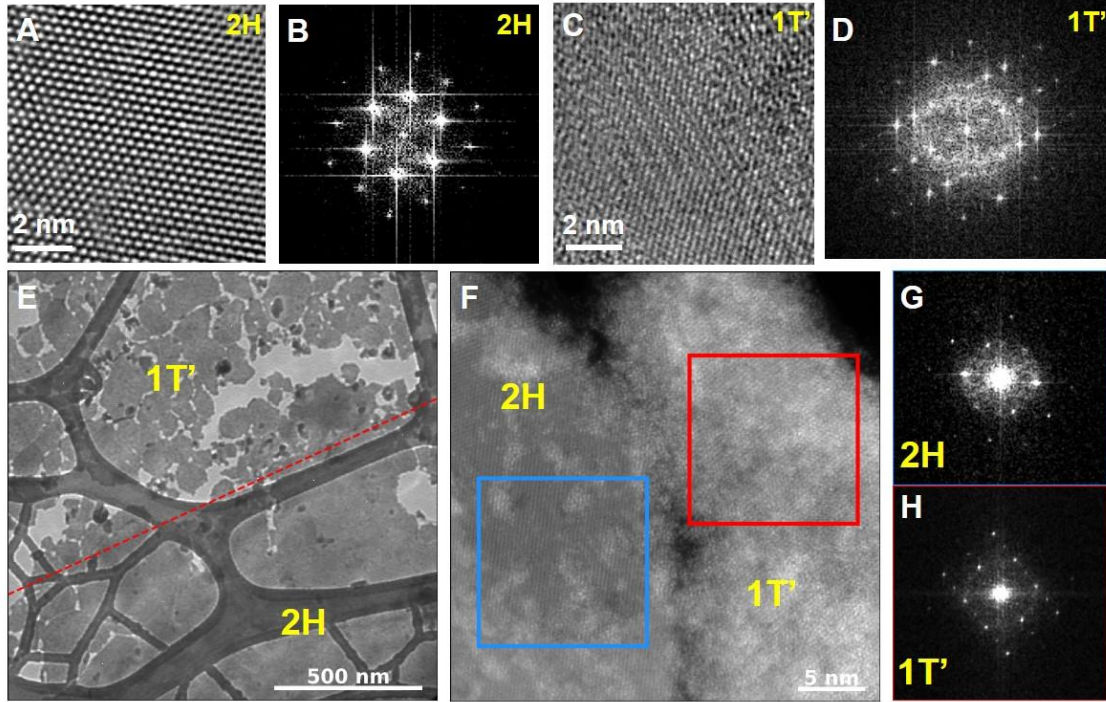
Figure 2-18 - Structure analysis of MoTe$_2$. TEM images and corresponding FFTs for 2H phase (A and B) and 1T' phase (C and D). (E) High defocus STEM Ronchigram image of the interface between 2H and 1T' phases in MoTe$_2$ heterostructure. (F) High magnification STEM image of the interface, showing that the two phases directly connect with one another. (G) FFT of the region marked by a blue outline in the STEM image in (F) demonstrating the region is single crystal and in the 2H phase. (H) FFT of the region marked by a red outline of STEM image in (F) demonstrating the region is single crystalline and 1T' phase.

2.4. Alternative synthesis approach

In addition to the synthesis of MoTe$_2$ through tellurizing Mo films, we have also studied converting MoS$_2$ and MoSe$_2$ to MoTe$_2$. Monolayer MoS$_2$ or MoSe$_2$ was

grown on SiO_2/Si by CVD method, which was then inserted into another quartz tube where a boat of Te power was placed upstream. The quartz tube was heated up to the reaction temperature and remained for a period of time. H_2/Ar was used as the carrier gas for the entire synthesis process. Figure 2-19 (a) shows the schematic diagram of the conversion process.

Figure 2-19 (b) displays an optical image of a $MoSe_2$ after conversion (at 600 °C for 30 min) and another $MoSe_2$ before conversion (inset). The color contrast of the sides and the area near top angle becomes weaker after conversion, suggesting that the structure of $MoSe_2$ has been changed. Figure 2-19 (c) and (d) are the Raman spectra and PL spectra taken at the weak-color area and the normal-color area. The normal-color area shows a Raman peak at 239 cm^{-1} (A_{1g}) and a PL peak at 822 nm, indicating it is still $MoSe_2$. The weak-color area shows a low-intensity Raman peak at 233 cm^{-1} (E_{2g}^1) and a quenched PL signal, suggesting that 2H $MoTe_2$ has been formed.
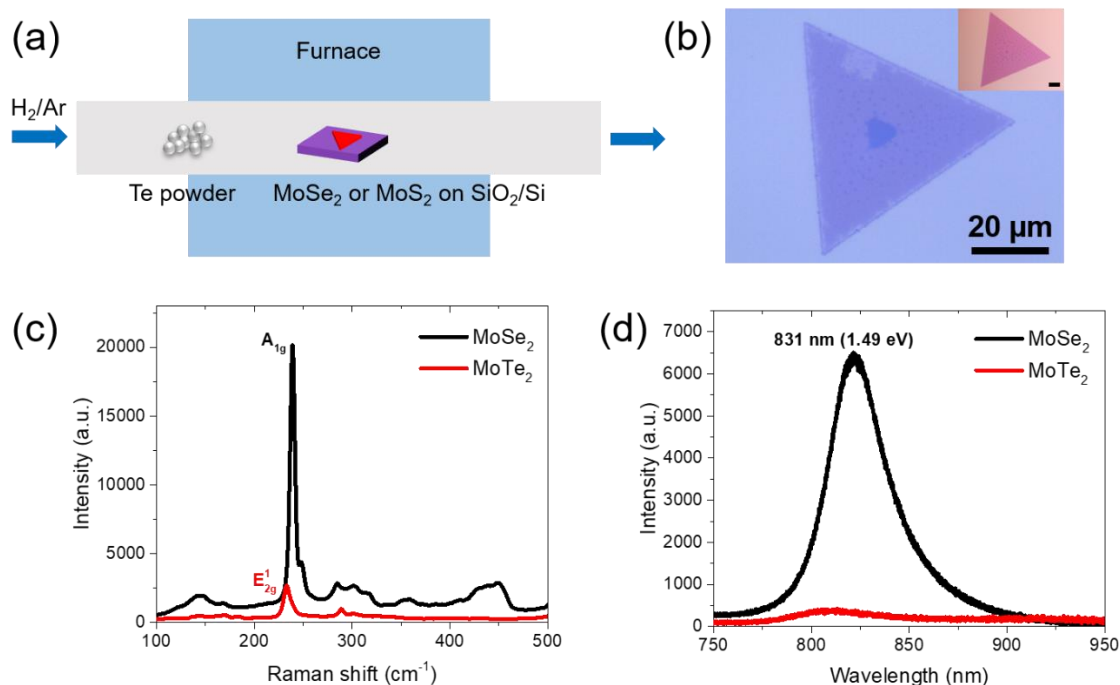
Figure 2-19 – (a) Schematic diagram of the conversion process. (b) Optical image of a MoSe₂ flake after conversion. Inset: A pristine MoSe₂ flake. (c) Raman spectra and (d) PL spectra of the weak-color area and normal-color area, indicating they are 2H MoTe₂ and MoSe₂, respectively.

Figure 2-20 (b) and (c) are Raman intensity mappings at A_{1g} and E_{2g}^1, respectively. Since the A_{1g} intensity of MoSe₂ is much higher than the E_{2g}^1 intensity of 2H MoTe₂, the color contrast in Figure 2-20 (c) is not strong enough to distinguish these two materials. Therefore, another mapping using the intensity ratio of E_{2g}^1/A_{1g} is presented in Figure 2-20 (e). Since SiO₂/Si doesn't have any Raman peak at A_{1g} or E_{2g}^1, the ratio of E_{2g}^1/A_{1g} is close to 1. The only region in the triangle showing a high ratio of E_{2g}^1/A_{1g} is in the weak-color area, indicating that MoSe₂ has been converted

to MoTe₂ there. Figure 2-20 (b) and (e) clearly show the spatial distribution of MoTe₂ and MoSe₂, which is supported by the PL intensity mapping at 822 nm in Figure 2-20 (d).
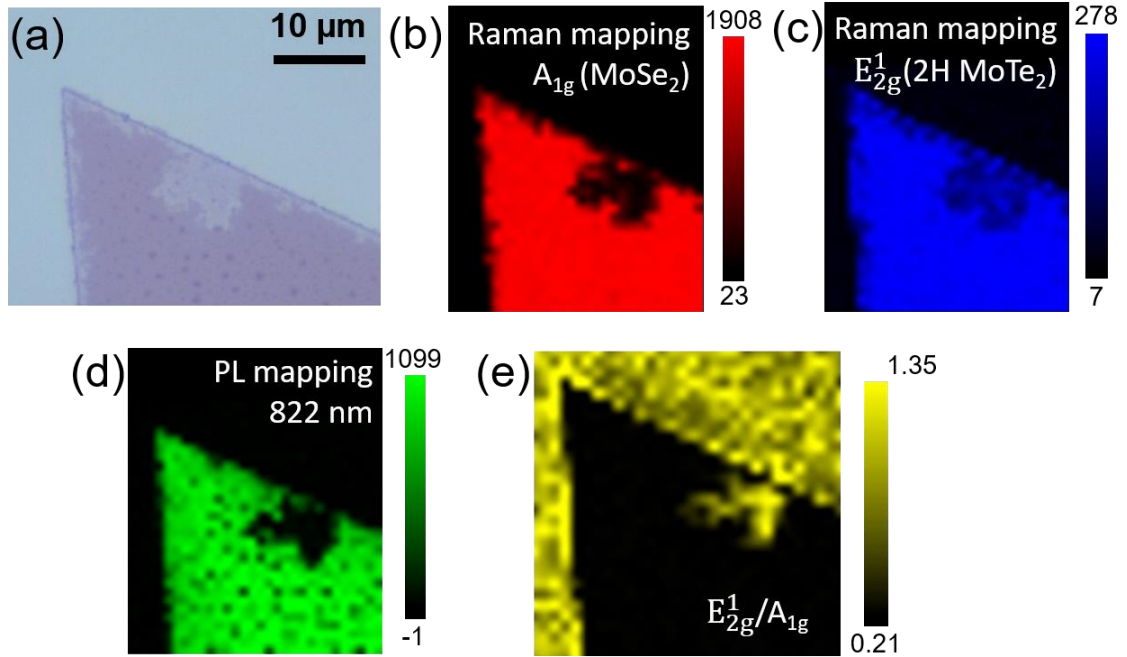
Figure 2-20 – (a) Optical image of the converted area in MoSe₂. Raman intensity mapping at (b) A_{1g} for MoSe₂, and (c) E_{2g}^1 for MoTe₂. (d) PL mapping at 822 nm. (e) Intensity ratio mapping of E_{2g}^1/A_{1g}.

To shed light on the influence of reaction temperature on the conversion, a series of experiments have been performed with the reaction time fixed at 30 min. Figure 2-21 shows the optical images of MoSe₂ flakes after reaction at 550 ℃, 600 ℃, 650 ℃, 700 ℃, and 750 ℃, respectively. The flake in Figure 2-21 (a) doesn't show any difference compared to the pristine MoSe₂, implying the conversion hasn't taken

place at 550 ℃. From 600 ℃ to 700 ℃, one can clearly observe that MoSe$_2$ flakes have been partially converted. With the increase of temperature, the converted area is expanding too. Figure 2-21 (e) shows that the MoSe$_2$ has been completely converted at 750 ℃. The results of temperature independent experiment indicate that reaction temperature plays a significant role in the proportion of conversion.
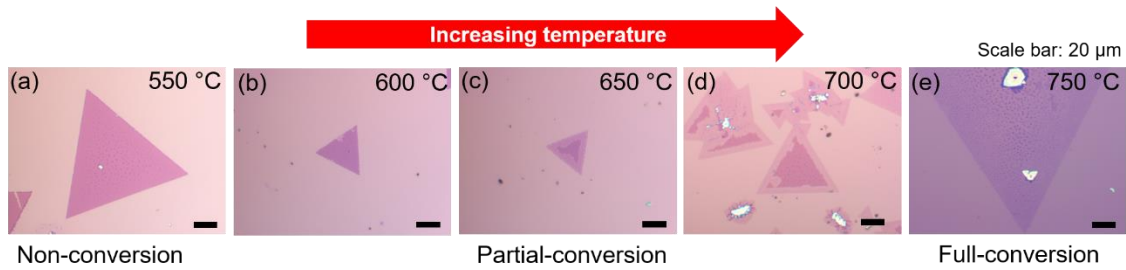
Figure 2-21 – (a-e) Optical images of MoSe$_2$ flakes after conversion at 550 ℃, 600 ℃, 650 ℃, 700 ℃, and 750 ℃, respectively.

The Raman and PL spectra of the converted area are demonstrated in Figure 2-22, where a pristine MoSe$_2$ and a 10 nm thick 2H MoTe$_2$ grown by tellurizing Mo film are used as references. Raman spectra of the pristine MoSe$_2$ (black curve) shows only one mode A$_{1g}$, while the E$_{2g}^1$ mode of 2H MoTe$_2$ appears in partially converted MoSe$_2$ (red curve), indicating that MoSe$_{2-x}$Te$_x$ alloy has been formed. As the increasing of x, the peak intensity of E$_{2g}^1$ becomes higher too (blue curve), with the appearance of B$_{2g}^1$, another Raman mode of 2H MoTe$_2$. The fully converted MoSe$_2$ or 2H MoTe$_2$ has a shifted E$_{2g}^1$ mode, a stronger B$_{2g}^1$ mode and a weaker A$_{1g}$ mode compared to the 10 nm thick 2H MoTe$_2$ film, which can be attributed to the difference in thickness and

grain size. In Figure 2-22 (b), the intensity of the PL peak of pristine $MoSe_2$ decreases in $MoSe_{2-x}Te_x$ alloy, and the position has a blue shift at the same time. In the fully converted $MoSe_2$ or 2H $MoTe_2$, the PL signal is completely suppressed. The Raman spectra and corresponding PL spectra suggest that $MoSe_{2-x}Te_x$ alloy has been formed during the conversion.
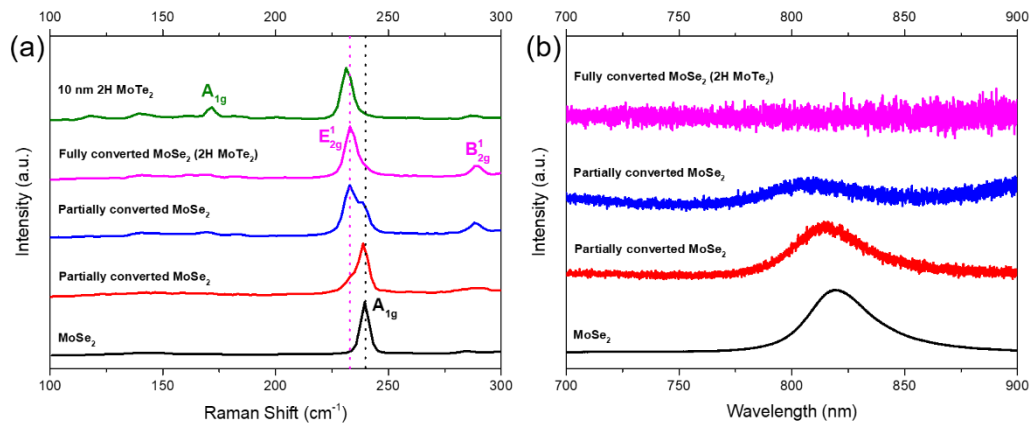
Figure 2-22 – (a) Raman and (b) PL spectra of pristine MoSe₂, partially converted MoSe₂, and fully converted MoSe₂, or 2H MoTe₂.

In addition to using $MoSe_2$ as the precursor material, we have also studied the conversion from MoS_2 to $MoTe_2$. Similarly, the formation of $MoS_{2-x}Te_x$ alloy was observed during conversion. Interestingly, we found that the fully converted MoS_2 transform to 1T' $MoTe_2$, and 2H/1T' mixed-phase $MoTe_2$. Figure 2-23 shows the Raman and PL spectra of pristine MoS_2 and converted MoS_2. The converted 1T' $MoTe_2$ has a B_g Raman mode, and the 2H/1T' mixed-phase $MoTe_2$ has both B_g and E_{2g}^1 modes.

The PL signals of them are all suppressed, compared to the PL peak of the pristine

MoS_2 at 675 nm.
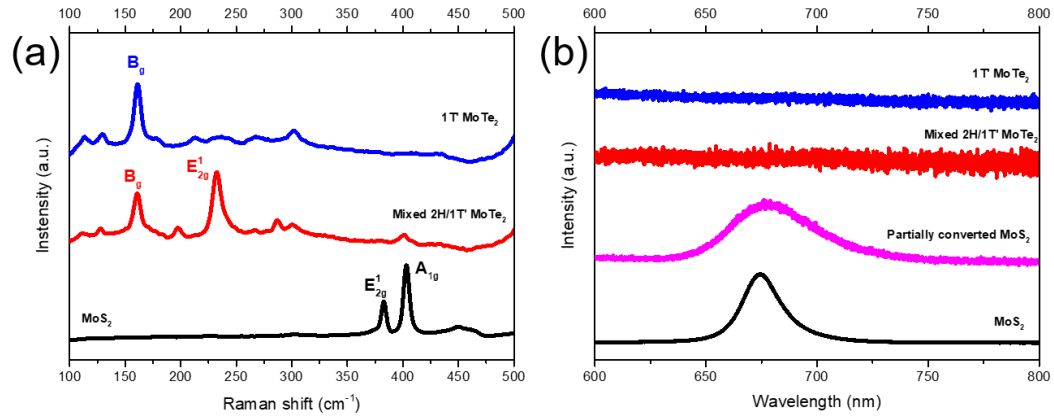
Figure 2-23 - (a) Raman and (b) PL spectra of pristine MoS₂, mixed 2H/1T'
MoTe₂ and 1T' MoTe₂ converted from MoS₂.

The difference in the phase of converted $MoTe_2$ from $MoSe_2$ and MoS_2 can be explained by comparing the lattice structure between the precursor material and the converted material. During the conversion, Te replaces Se or S, causing the strain in the lattice. Since the difference in size between Te and S is larger than that between Te and Se, the strain generated by replacing S with Te is also stronger. As introduced previously, $MoTe_2$ tends to form 1T' phase under large strain. Therefore, 1T' $MoTe_2$ can be formed during MoS_2 conversion.

2.5. Conclusion

In conclusion, we report the synthesis of large-area $MoTe_2$ films through tellurizing thin Mo films by CVD method. The phase of $MoTe_2$ can be controlled by reaction temperature and time. Characterization techniques including Raman spectroscopy, SEM, AFM, UV-vis spectroscopy, TEM, XPS, XRD have been used to examine the properties of $MoTe_2$ films systematically. Another approach by converting $MoSe_2$ or MoS_2 to $MoTe_2$ is also discussed. $MoSe_2$ is found to convert to 2H' $MoTe_2$, and $MoSe_{2-x}Te_x$ alloy. MoS_2 can be converted to 1T' MoTe2, 2H/1T' mixed-phase $MoTe_2$, and $MoS_{2-x}Te_x$ alloy.

<div align="right">

Chapter 3

</div>

Low-contact Barrier in 2H/1T' MoTe$_2$ in-plane Heterostructure

3.1. Introduction

Atomically thin 2D materials have drawn significant attention since the discovery of graphene.[58,59] The 2D materials family consists of a variety of members that carry a wide range of novel properties.[59–63] Interesting optical, mechanical and electrical phenomena have been frequently reported.[64–69] In addition, 2D materials can be further combined to form van der Waals (vdWs) heterostructures with structural complexity as well as property diversity. The techniques consist of stacking distinct 2D materials vertically or laterally, and they have been achieved by physical manipulation as well as chemical synthesis. These vdWs heterostructures include semiconductor-semiconductor junctions, such as WS$_2$/MoS$_2$,[70–72] WSe$_2$/MoSe$_2$,[73,74] metal-insulator junctions, such as graphene/hexagonal boron nitride (h-BN),[75–77] and metal-semiconductor junctions. Among them, 2D metal-semiconductor junctions have been recently extensively studied because they show potential to resolve the

issue of the existence of contact resistance at the interface between the 2D semiconducting channel and the deposited metal electrodes like Au or Ti due to the Schottky barrier.[78–82] Low contact resistance is essential for improving the performance of 2D electronic devices.

Figure 3-1 demonstrates different types of metal-semiconductor junction, which can be classified as top contact and edge contact. Unlike the covalent bonds between metal and bulk semiconductor, a van der Waals (vdW) gap is usually formed at the interface between metal and 2D semiconductor. The vdW gap plays the role as a tunnel barrier in addition to the inherent Schottky barrier, resulting in increasing the total contact resistance. Therefore, edges contacting is more beneficial to 2D materials, due to the stronger orbital overlaps and the reduction of tunnel barriers.[78]
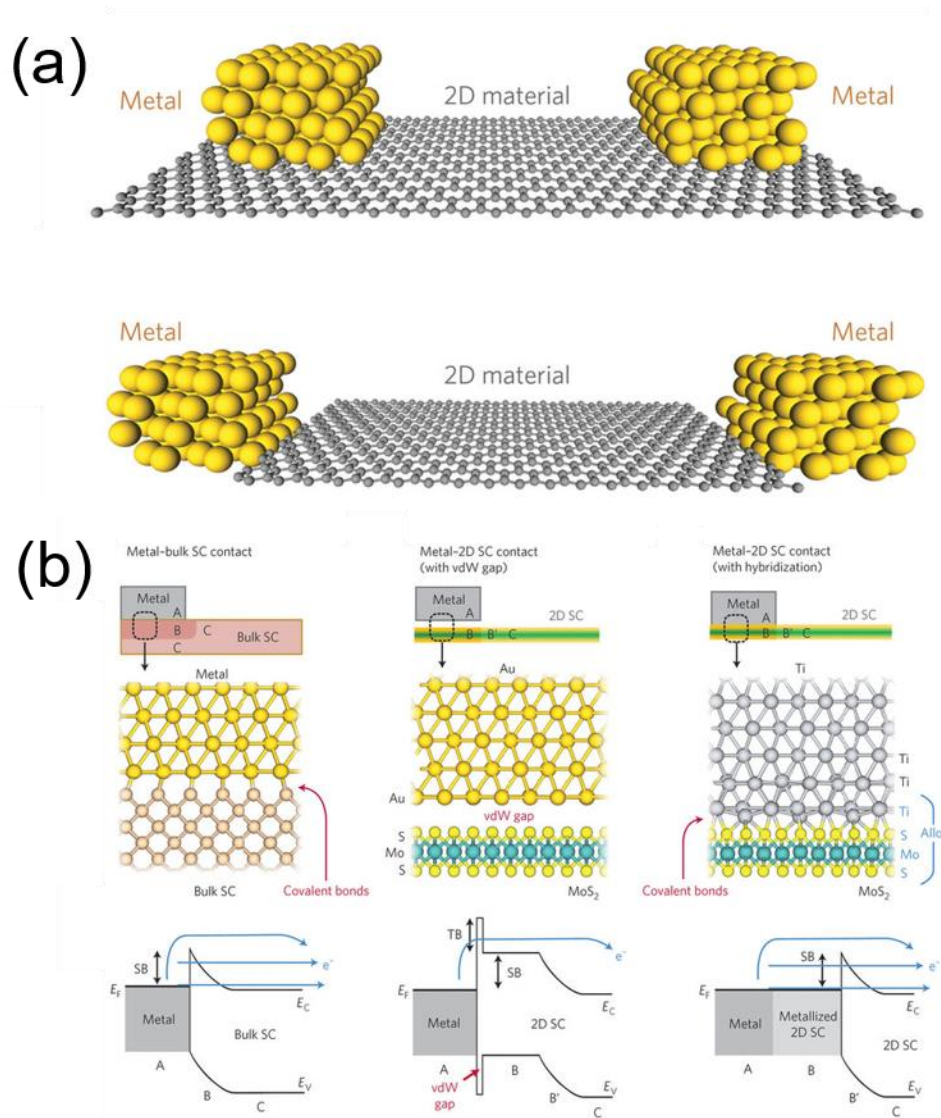
Figure 3-1 – Different types of metal-semiconductor junction. (a) Top contact and edge contact between metal and 2D material. (b) Different types of top-contacted metal and semiconductor and their respective band diagrams.[78]

A few approaches have been proposed to reduce the contact resistance such as using graphene contacts,[83–89] contact doping,[90–92] and phase-engineering[42,93,94].

Graphene contact has proven difficult to be directly synthesized with transition metal dichalcogenides (TMDs) due to its lattice mismatch and incompatible synthesis methods. The physical transfer is the most common fabrication method, yet it requires complex steps and it can be difficult to create a clean and sharp interface. The latter two chemical methods remain insufficient for large-scale application and chemical stability. Therefore, direct growth of large-area, seamless-bonding 2D metal-semiconductor junctions with industrial compatibility plays a critical role in the future of vdWs integrated circuits.

Here is an example of reducing the Schottky barrier at the interface between metal and semiconductor by adding a mixed transition layer. Kim et al.[91] investigated the Pd/WSe$_2$ (MS) junction and the NbSe$_2$/W$_x$Nb$_{1-2}$Se$_2$/WSe$_2$ (M-vdW) hybridized heterojunction in the back-gate FET devices. A longer hot-carrier lifetime and more superior electrical stability were observed in M-vdW-junctioned device. It can be attributed to the absence of dangling bonds and fewer trap states at the interface of M-vdW junction.
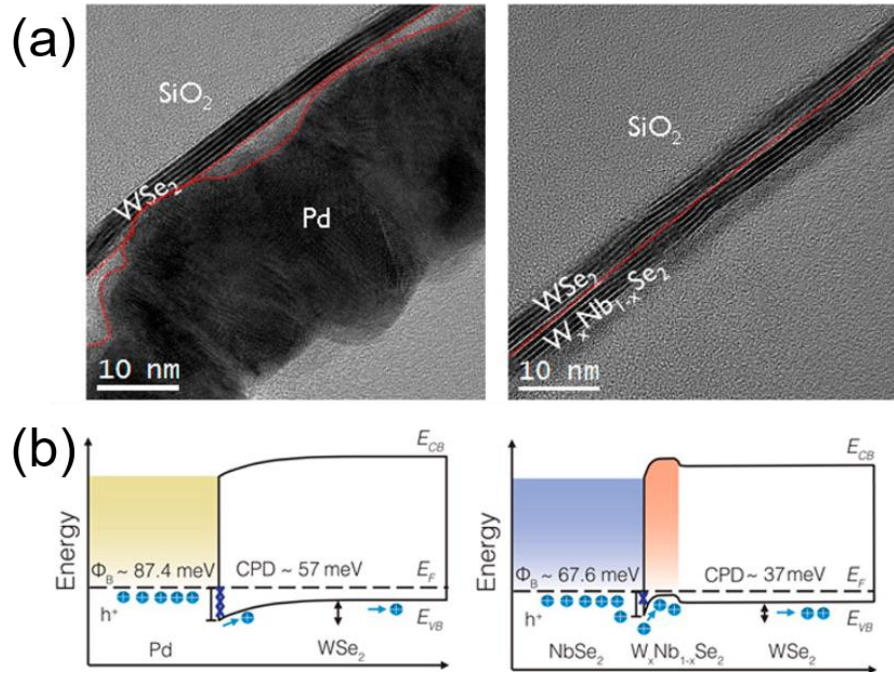
Figure 3-2 – (a) Cross-sectional HRTEM images of MS junction and M-vdW junction. (b) The schematic energy band diagrams of MS junction and M-vdW junction with Schottky contact.[91]

Another example is a few-layer WSe_2 FET contacted by graphene, reported by Chuang et al.[87] Figure 3-3 shows the schematic illustration of the FET structure, where the work function of graphene can be modulated by an ionic liquid gate. The extremely high field-effect mobility values show that highly doped graphene is an excellent contact electrode material for TMD FETs.
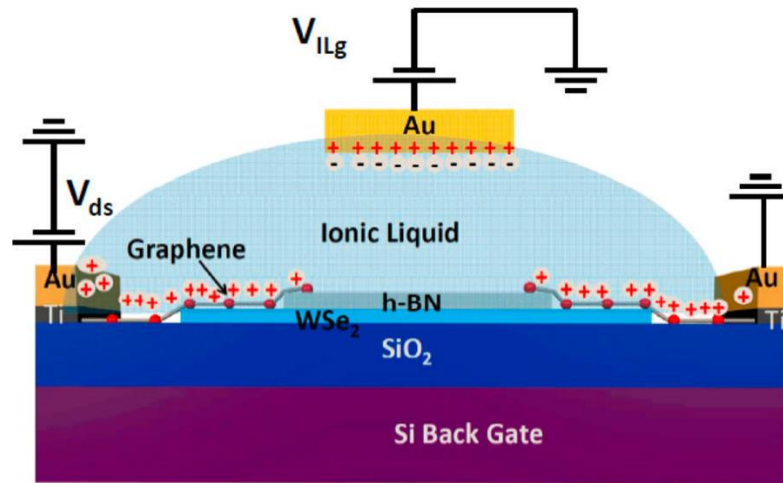
Figure 3-3 - Schematic diagram of the WSe$_2$ FET with ionic-liquid-gated graphene contacts.[87]

Recent research efforts in 2D materials have shown an increasing focus on molybdenum ditelluride (MoTe$_2$). Unlike other TMDs, MoTe$_2$ has two stable phases, hexagonal 2H phase, and monoclinic 1T' phase, both of which can be synthesized directly.[48,49,51,55,95–97] Monolayer 2H MoTe$_2$ is a semiconductor with a direct band gap of 1.1 eV, while bulk 2H MoTe$_2$ has an indirect band gap of 1 eV.[32] These numbers are close to that of Si, which makes 2H MoTe$_2$ promising for electronic devices and optoelectronic applications.[34,98–100] 1T' MoTe$_2$ is a type-II Weyl semimetal and has been reported to have large magnetoresistance and pressure-driven superconductivity. Due to the small energy difference between these two phases,[19] the 2H-1T' phase transition has been achieved by using laser irradiation[42] or tensile strain[101]. It is worth noting that 1T' phase and 2H phase MoTe$_2$ can form a metal-

semiconductor junction, where 1T' MoTe$_2$ can be used as a contact material to solve the contact issue. MoTe$_2$ thus not only possesses a myriad of physical properties to further unravel but also shows great potential towards various industrial applications such as analog circuits and spintronics. Previous reports have shown various methods to synthesize MoTe$_2$: mechanical exfoliation,[32,34,42] chemical vapor transport (CVT)[36,29] and chemical vapor deposition (CVD)[48,49,51,55,102] have been the most studied. Compared to other methods, CVD method is the most promising for large-scale synthesis and thickness control, making MoTe$_2$ a candidate for wafer-scale integration of devices. It has been reported that monolayer MoTe$_2$ tends to oxidize in air.[103] Thus, few-layer MoTe$_2$ films should be more suitable for practical applications.

In this chapter, several types of MoTe$_2$ based devices are fabricated and measured. In a field-effect transistor (FET) device, 2H phase MoTe$_2$ channel shows p-type semiconducting behavior and exhibits exponentially higher sheet resistance than 1T' MoTe$_2$. We also demonstrate a decreased contact resistance through using the 1T' phase as the contact electrodes for 2H phase-based transistor by observing improved drain-source current compared to Ti/Au metal contacts. Theoretical simulations further confirm that the contact barrier of 2H/1T' MoTe$_2$ in-plane heterostructure is lower than that of 2H MoTe$_2$/Ti vertical junction.

3.2. Experimental results

To study the electrical properties of the large MoTe$_2$ films, several types of electrical devices have been fabricated. Figure 3-4 (a) shows a schematic of the two kinds of MoTe$_2$ devices measured and Figure 3-4 (b) shows the optical image of a typically fabricated device. CVD grown MoTe$_2$ film is first patterned into ribbons by lithography and reactive ion etching (RIE), followed by a second lithography step to deposit metal contacts by electron beam evaporation (Ti/Au, 5 nm/45 nm). Due to the apparent visual difference between 1T' and 2H MoTe$_2$, the two phases can be easily identified for separate device fabrication. We first study the electrical properties of 1T' and 2H MoTe$_2$ ribbons respectively. The transfer length method (TLM) is used to extract the contact resistance between the Ti/Au- MoTe$_2$ interface as well as the intrinsic sheet resistance of MoTe$_2$.[104,105]

TLM assumes contact resistance independent of device length and enables extraction of contact resistance (R_c in a unit of $\Omega \cdot um$) as well as intrinsic sheet resistance (R_S in a unit of $\Omega/\square$) by combined studies on I-V curves from devices of varied channel lengths as displayed in Figure 3-4 (c) and (d).
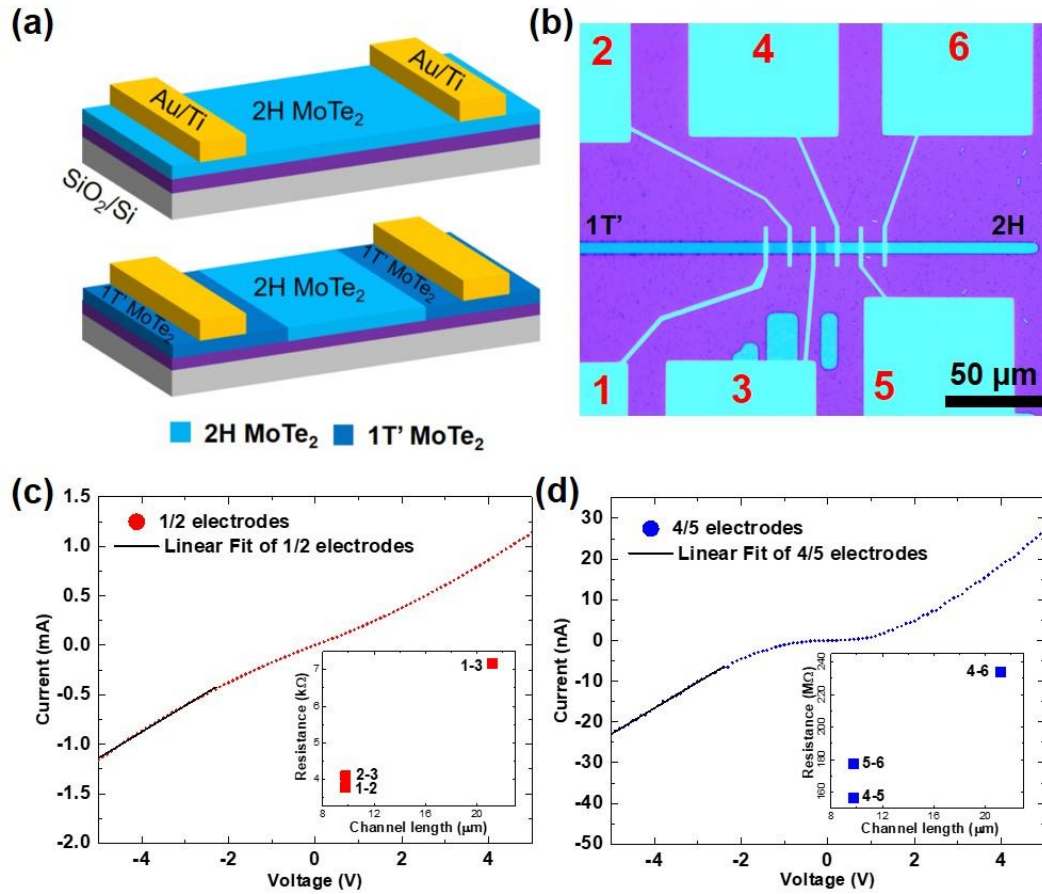
Figure 3-4 - Electrical measurement of MoTe₂ devices. (A) Schematic illustration of two types of MoTe₂ devices. For the device on op, a 2H MoTe₂ channel is directly contacted by metal electrodes. For the device on the bottom, 1T' MoTe₂ interconnects a 2H MoTe2 channel and metal electrodes. (B) An optical image of a MoTe₂ ribbon contacted by metal electrodes labeled 1 to 6. Electrodes 1 to 3 are in contact with the 1T' phase, while electrodes 4 to 6 are in contact with the 2H phase. I_{ds}-V_{ds} curves of the 1T' phase and 2H phase

are shown in (C) and (D) respectively. Inset: Resistance obtained from different pairs of electrodes and channel lengths.

R_c and R_S can be extracted by the following equation

Equation 3-1

$$R_{tot} = \sum \frac{R_c}{W} + \sum R_S \cdot \frac{L}{W}$$

Where R_{tot} refers to the total device resistance, L, W refers to the device channel length and width respectively.

R_s and R_c of MoTe₂ have been extracted as follows

Equation 3-2

$$R_{C,1T'} = 3.26 \ k\Omega \cdot \mu m \qquad R_{S,1T'} = 1.71 \ k\Omega/\square$$

Equation 3-3

$$R_{C,2H} = 326.5 \ M\Omega \cdot \mu m \qquad R_{S,2H} = 35.2 \ M\Omega/\square$$

We can see an apparent differential sheet resistance in an order of ~20,000 between 2H and 1T' MoTe$_2$, and the differential contact resistance between 2H/metal and 1T'/metal is in an order of 100,000. In addition, another device has been characterized with similar electrical characteristics, shown in Figure 3-5.
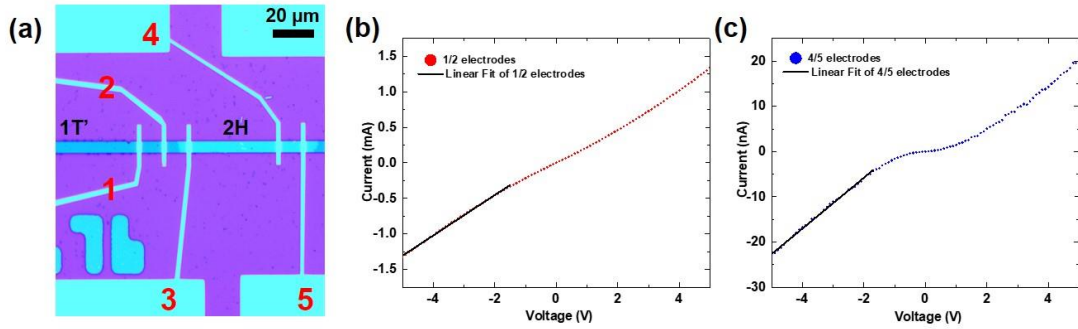
Figure 3-5 - Electrical measurement of another MoTe$_2$ device. (A) An optical image of a MoTe2 ribbon contacted by Au/Ti electrodes labeled as 1 to 5. Electrodes 1 to 2 are in contact with 1T' phase. Electrodes 3-5 are in contact with 2H phase. I$_{ds}$-V$_{ds}$ curves of 1T' phase and 2H phase are shown in (B) and (C) respectively. The electrical characteristics between electrodes 1 and 2, and electrodes 4 and 5 correspond well with numbers in (eq. 2), and (eq. 3) respectively.

2H MoTe$_2$ has been transferred and studied in a back-gated FET geometry, where Ti/Au is used as the contact metal (Figure 3-6 (a) inset). 2H-MoTe$_2$ shows field-effect behavior, which is not observed for 1T'-MoTe$_2$. The typical transfer characteristics of the back-gated devices are shown in Figure 3-6 (a) and (b). P-type behavior is observed on 2H-MoTe$_2$ FET devices, consistent with previous theoretical

and experimental results.[34,51] The field-effect mobility can be calculated by using the equation

Equation 3-4

$$\mu=[dI_d/dV_{bg}]\times[L/(WC_gV_d)]$$

where L and W are the channel length and width. $C_g=\varepsilon_0\varepsilon_r/d$ is the gate capacitance per unit area, where d=285 nm is the SiO_2 layer thickness, $\varepsilon_0=8.854\times10^{-12}$ F/m is the free-space permittivity and $\varepsilon_r=3.9$ is the relative permittivity of SiO_2. dI_d/dV_{bg} is estimated from the slope of the linear fit of the data I_d-V_{bg}. From the data in Figure 3-6 (a), the on/off ratio is estimated to be around 126 at V_{bg}=-80V, while the electron mobility of ~0.5 $cm^2V^{-1}s^{-1}$, a number comparable to the highest performing CVD grown $MoTe_2$ reported so far.[51,95] The mobility could be underestimated due to the relatively high contact resistance. Figure 3-6 (b) demonstrates the monotonic behavior of the I-V curve at back gate voltages sweeping from 0 V to -80 V.
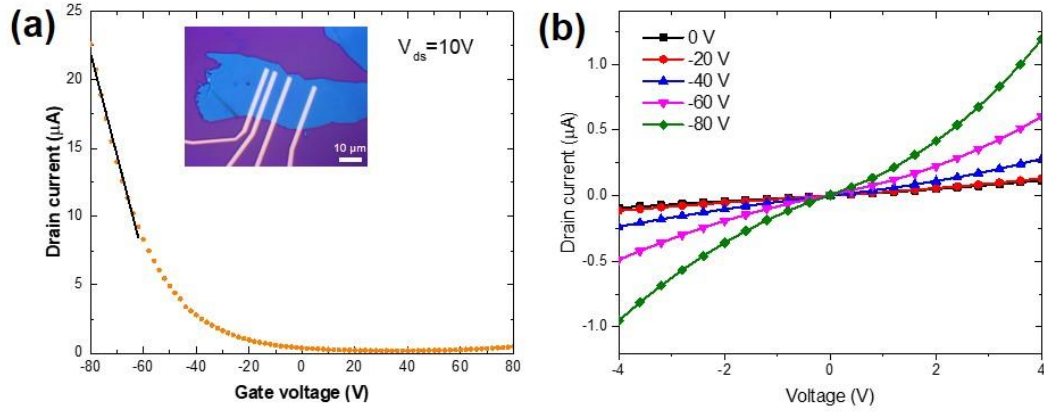
Figure 3-6 - Transfer characteristics of 2H MoTe$_2$ FET. (A) Room-temperature field effect transfer characteristic for the 2H MoTe$_2$ FET at 10 V drain-source voltage. Inset: an optical image of the 2H MoTe$_2$ FET. (B) I$_{ds}$-V$_{ds}$ curves acquired for the back-gate voltage V$_{bg}$ values at 0, -20, -40, and -80 V.

In addition to studying the electrical performance of phase pure 1T' and 2H MoTe$_2$, we examine the electrical properties of the 1T'-2H junction. Based on our measurement, CVD grown 1T'-2H-1T' structure provides a low resistance contact for 2H-MoTe$_2$. An optical image of a metal/1T'/2H/1T'/metal MoTe$_2$ device is shown in Figure 3-7 (a), in which a 2H-MoTe$_2$ channel is planarly sandwiched by two 1T'-MoTe$_2$ strips, which are contacted by Ti/Au electrodes for measurement. A Raman intensity mapping of 2H phase E_{2g}^1 mode (232 cm^{-1}) (Figure 3-7 (b)), and 1T' phase B_g mode (161 cm^{-1}) (Figure 3-4 (c)), is conducted over the device, revealing the spatial distribution of 1T'/2H/1T' MoTe$_2$ heterostructure. The I-V curve of the 1T' contacted 2H MoTe$_2$ device is shown in Figure 3-7 (d). Compared with Figure 3-4 (c),

I-V curve in Figure 3-7 (d) appears to be more linear, indicating smoother increasing of drift carriers cause by increasing drain-source voltage, overcoming the problem caused by the Schottky barrier between 2D materials and common metals. To compare the electrical characteristics of the device with 1T'-phased electrodes and with Ti/Au on the 2H phase, I-V curves of electrodes 7-8 and electrodes 4-5, normalized by the dimension of the 2H channel ($I_{normalized} = I \cdot \frac{L}{W}$), are co-plotted in Figure 3-7 (e). By using metal-1T' as the electrodes for 2H MoTe$_2$ channel, the slope of the I-V curve is increased by 7-8 times compared with the device with metal-2H geometry, implying that more current can be collected through this device, and lower contact resistance is formed at the interface. Low resistance contact on 2D vdWs materials has always been a challenge, not only for physical studies on 2D materials but also for high-performance 2D electronics. The CVD-grown 1T'-2H interface provides a natural and simple solution for contacting semiconducting 2H-MoTe$_2$.
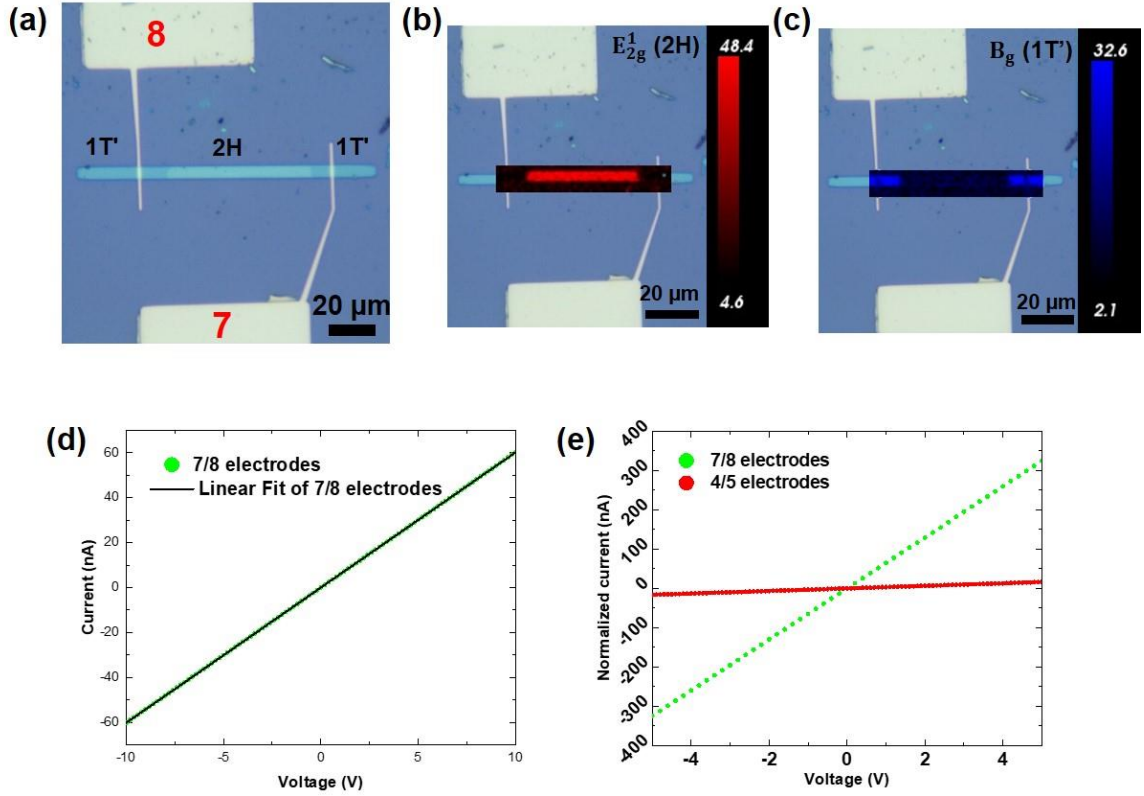
Figure 3-7 - (a) An optical image of a 1T'/2H/1T' MoTe₂ ribbon, where metal electrodes 7 and 8 are in contact with the 1T' phase. Raman intensity maps using (b) 2H MoTe₂ E_{2g}^1 mode at 232 cm^{-1} and (c) 1T' MoTe₂ B_g mode at 161 cm^{-1} confirm the spatial distribution of 1T'/2H/1T' MoTe₂ heterostructure. (d) I$_{ds}$-V$_{ds}$ curve measured by electrodes 7-8. (e) Normalized I$_{ds}$-V$_{ds}$ curves acquired by electrodes 4-5 and 7-8.

3.3. Theoretical simulation

To reveal the mechanism of transport phenomena in MoTe₂ with different phases, density functional theory (DFT) calculations are carried out to compare the

Schottky barriers of 2H MoTe$_2$/Ti vertical junction and MoTe$_2$ 2H/1T' in-plane heterostructure. Since our experiment shows that 2H MoTe$_2$ prepared by CVD method is a p-type semiconductor, we focus on the Schottky barrier for holes Φ_h, which is determined by the energy difference between the Fermi level and the valence band maximum (VBM) of the semiconductor in the junction: [106]

Equation 3-5

$$\Phi_h = E_F - E_{VBM}$$

where E$_F$ and E$_{VBM}$ are the energy of the Fermi level and VBM of the semiconductor in the junction, respectively.

MoTe$_2$ 2H/1T' in-plane heterostructure is modeled by in-plane splicing of MoTe$_2$ with 2H and 1T' phases as shown in Figure 3-8 (a), while 2H MoTe$_2$/Ti vertical junction is constructed by a vertical stacking of three layers of MoTe$_2$ with 2H phase and six layers of titanium as shown in Figure 3-8 (c), and the lattice mismatch is less than 3.5% for each junction. Structural optimization and self-consistent total energy calculations were performed adopting generalized gradient approximation (GGA), with the Perdew-Burke-Ernzerhof (PBE) exchange-correlation functional, along with the projector-augmented wave (PAW) potentials, using the Vienna Ab initio Simulation Package (VASP)[107]. Electronic wavefunctions are expanded in a plane wave basis set with the kinetic energy cutoff of 280 eV and for the Brillouin zone integration 1 × 5 × 1 and 3 × 5 × 1 Monkhorst-Pack k-point mesh are used for MoTe$_2$

2H/1T' in-plane heterostructure and 2H $MoTe_2$/Ti vertical heterostructure, respectively. The energy convergence criterion for electronic wave-function is set to be 10^{-5} eV. A vacuum layer of about 10 Å is chosen to guarantee no spurious interaction between layers in monolayer simulations using periodic boundary conditions. The projected electronic bands onto Mo of $MoTe_2$ with 2H phase in $MoTe_2$ 2H/1T' in-plane heterostructure and Mo in 2H $MoTe_2$/Ti vertical junction are plotted in Figure 3-8 B and D, respectively.
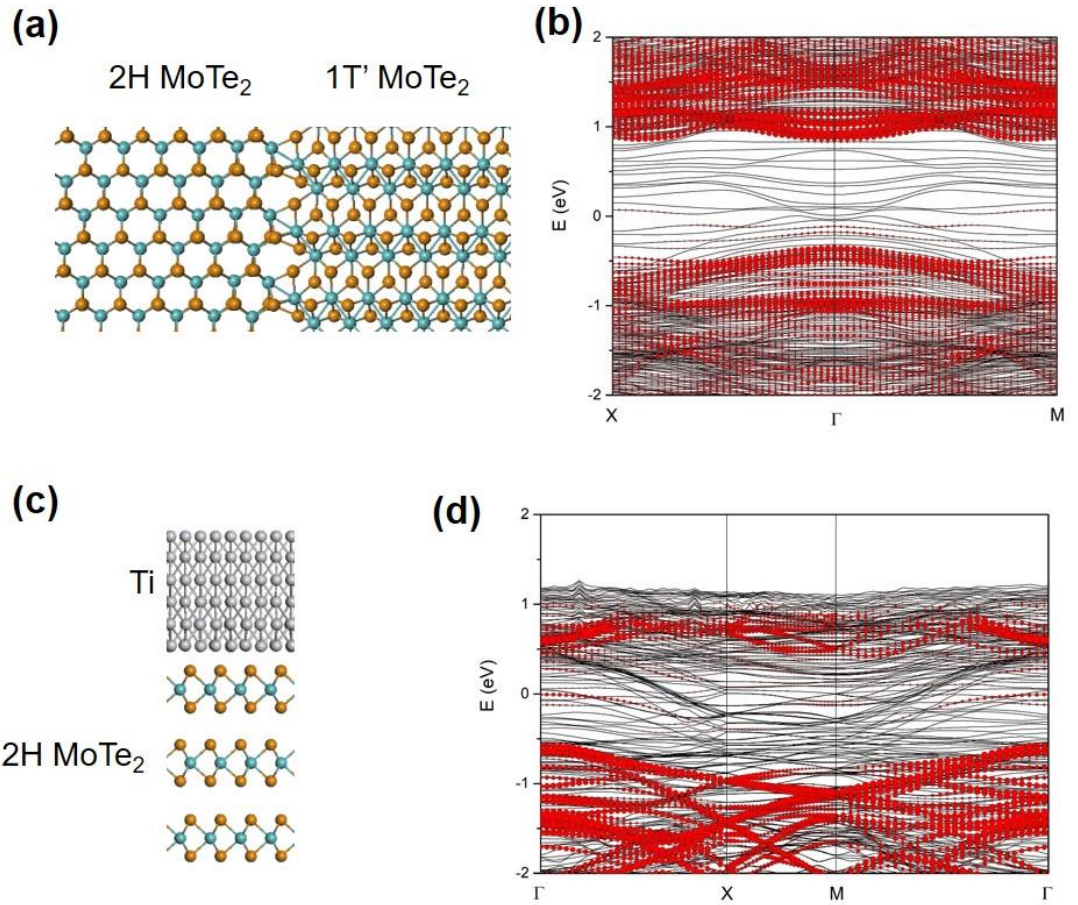
Figure 3-8 - Band alignments of 2H/1T' MoTe$_2$ in-plane heterostructure and 2H MoTe$_2$-Ti vertical junction. (A) Structure and (B) the projected electronic bands onto Mo of MoTe$_2$ with 2H phase in MoTe$_2$ 2H-1T' in-plane heterostructure. (C) Structure and (D) the projected electronic bands onto Mo in 2H MoTe$_2$-Ti vertical junction.

For a comprehensive analysis, the projected electronic bands onto Mo of MoTe$_2$ with 1T' phase in MoTe$_2$ 2H/1T' in-plane heterostructure, and Mo in 1T' MoTe$_2$/Ti vertical junction are shown in Figure 3-9 (a) and (b), respectively. In Figure

3-8 (b) the VBM of MoTe$_2$ with 2H phase is folded to the Γ point and 0.25 eV lower than Fermi level in MoTe$_2$ 2H/1T' in-plane heterostructure, while that in 2H MoTe$_2$/Ti vertical junction is also folded to the Γ point but 0.5 eV lower than Fermi level as in Figure 3-8 (d). Besides, MoTe$_2$ with 1T' phase remains metallic in both MoTe$_2$ 2H/1T' in-plane heterostructure and 1T' MoTe$_2$/Ti vertical junction. The electronic bands of the heterostructure can be projected into respective 2H and 1T' phases that are the same as the isolated phases, implying the validity of the MoTe$_2$ 2H/1T' in-plane heterostructure.[108] These DFT results indicate that the contact barrier of MoTe$_2$ 2H/1T' in-plane heterostructure is 0.25 eV lower than that of 2H MoTe$_2$/Ti vertical junction, as sketched in Figure 3-9 (c), confirming that 1T'/2H/1T' MoTe$_2$ structure has much lower contact resistance than Ti/2H MoTe$_2$/Ti structure.
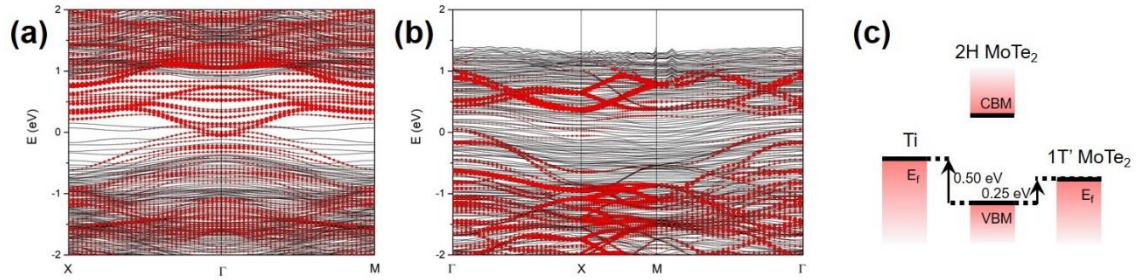
Figure 3-9 - Band alignments of 2H/1T' MoTe$_2$ in-plane heterostructure and 1T' MoTe$_2$-Ti vertical junction. (A) The projected electronic bands onto Mo of MoTe$_2$ with 1T' phase in MoTe$_2$ 2H-1T' in-plane heterostructure. (B) The projected electronic bands onto Mo in 1T' MoTe$_2$-Ti vertical junction. (c)

Sketch of the band alignment for 2H MoTe$_2$-Ti vertical junction and MoTe$_2$ 2H--1T' in-plane heterostructure.

3.4. Conclusion

Several types of MoTe$_2$-based devices were fabricated and measured in this chapter. We demonstrate an electrical device based on direct-grown semiconductor-metal heterostructure 2H/1T' MoTe$_2$, where 1T' phase serves as the electrode contacts for the 2H phase channel. The normalized current density through this device is higher than that measured by using metal contacts directly on 2H phase. Both experimental results and DFT calculations indicate the sharp and seamless bonded 2H/1T' MoTe$_2$ heterostructure provides a lower contact resistance than 2H MoTe$_2$/Ti vertical junction. This work provides a strategy to achieve low contact resistance in 2D electronic devices. This novel contact method can improve the performance of 2D electronic and optoelectronic devices, laying the groundwork for large-scale manufacturing.

<div align="right">Chapter 4</div>

Raman Enhancement on 2H and 1T′ MoTe₂

4.1. Introduction

4.1.1. History and mechanism of SERS

After the discovery of Raman scattering in 1928 by Raman and Krishnan,[109] researchers have been using Raman spectroscopy as a powerful analytical tool to provide a structural fingerprint of analytes.

The first surface Raman from pyridine was observed on roughened silver in 1974.[110] In 1977, Jeanmaire and Van Duyne demonstrated that the enhanced signal intensity was not affected by the concentration of the scattering molecule.[110] Instead, the roughened noble-metal surface provided an enhanced electric field which increased the Raman scattering cross-section of adsorbed pyridine molecules. This surface-sensitive technique that enhances Raman scattering process is called surface-

enhanced Raman spectroscopy or surface-enhanced Raman scattering (SERS). Since then, the SERS field has grown dramatically.

There are two proposed mechanisms of SERS process, electromagnetic enhancement, and chemical enhancement. In electromagnetic theory, when the incident light strikes the surface of plasmonic materials such as noble metals with nanoscale features, localized surface plasmons are excited. The Raman intensity of absorbed molecule can be enhanced by up to 6 to 8 orders of magnitude, which plays a predominant role in the SERS process.[111] The chemical enhancement mechanism involves charge transfer between the metal and adsorbed molecules. This charge transfer state provides a pathway for resonant excitation, which can increase Raman intensity by around 100.[111] Electromagnetic enhancement is a long-range effect decaying exponentially with distance between the adsorbed molecule and metallic substrate, while chemical enhancement is a short-range effect with a direct interaction on the angstrom scale.[112]
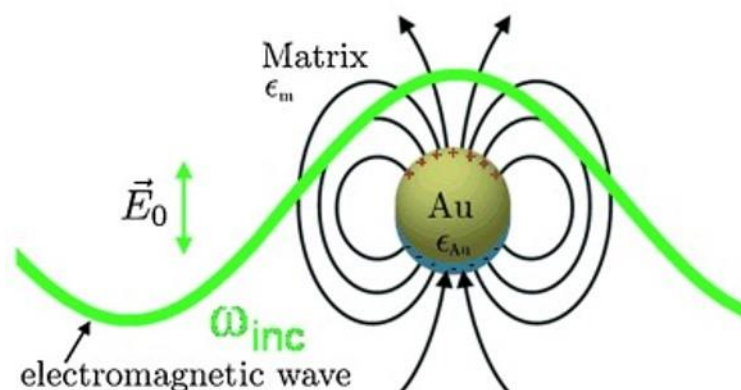
Figure 4-1 – Electromagnetic enhancement in SERS. A gold nanoparticle plays the role as a nanoantenna by excitation of a dipolar localized surface plasmon resonance.[113]

For example, Tian et. al[114] studied the influence of gold nanoparticles shape on SERS enhancement. SERS spectra of the organic dye, rhodamine 6G (R6G) with differently shaped gold nanoparticle were compared in Figure 4-2. It can be observed that all the Raman modes of R6G were strongly enhanced on gold nanostars, whereas a few of them were able to be detected in the R6G solution alone. In addition, gold nanostars showed the highest SERS enhancement of R6G compared to nanotriangles and nanospheres. Because the surface plasmon resonance (SPR) of nanospheres, nanotriangles, and nanostars are located at 560 nm, 800 nm, 600/785 nm. The results are consistent with the absorbance of the nanoparticles at the Raman source wavelength (785 nm), indicating that increasing the number of local field hotspots can optimize the SERS enhancement.
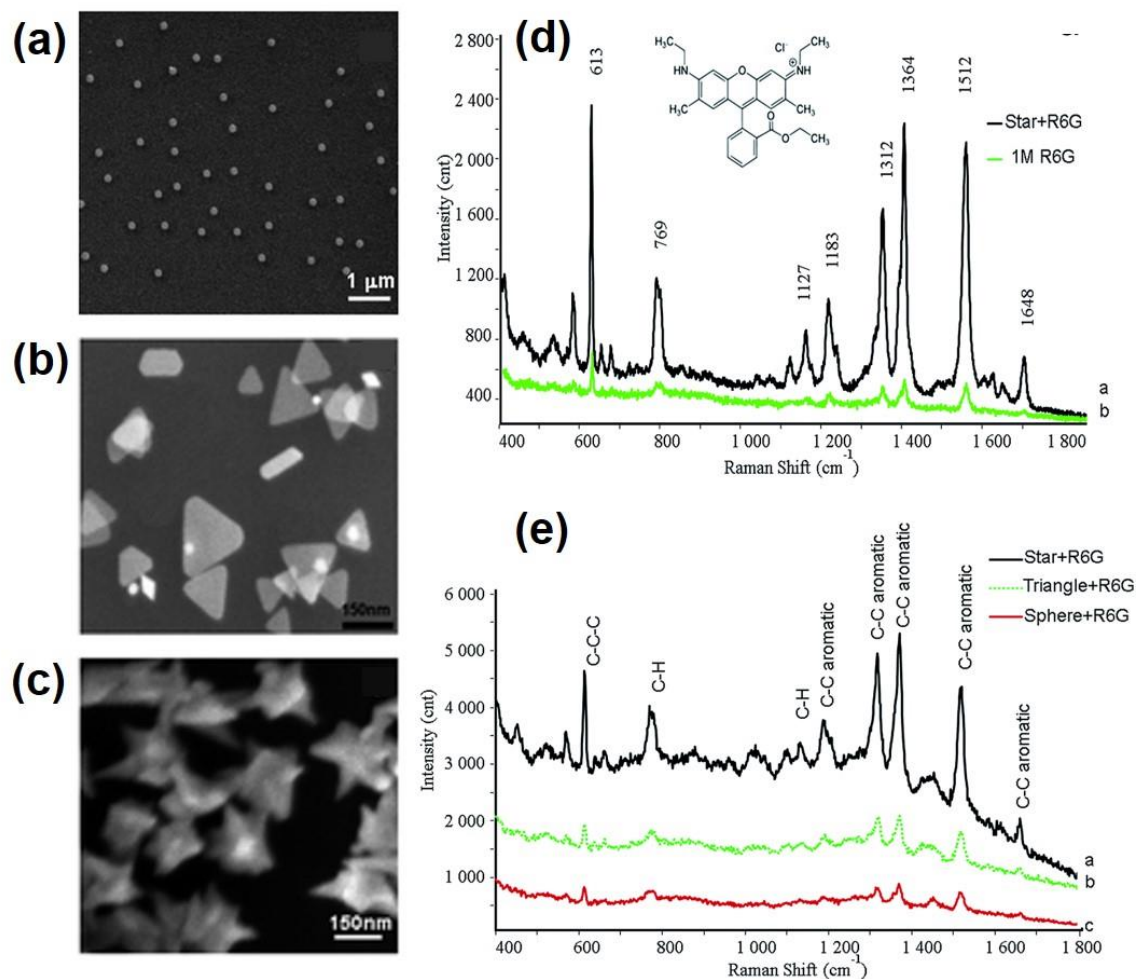
Figure 4-2 – (a-c) SEM images of differently shaped gold nanoparticles. (a) Nanospheres. (b) Nanotriangles. (c) Nanostars. (d) Comparision of SERS spectra of 5 µM R6G in gold nanostar solution and 1 M R6G alone. (e) Comparision of SERS spectra of 5 µM R6G in solution of differently shaped gold nanoparticles. All the spectra were measured by 785 nm laser.[114]

Since SERS technique has many advantages, it has demonstrated a lot of applications in a broad range of fields, such as electrochemistry, biochemistry and biosensing, single-molecule detection.

4.1.2. SERS on 2D materials

Due to the huge enhancement of the electromagnetic mechanism, roughened noble metals such as Au, Ag and Cu have been widely used in SERS application. However, there still exist some limitation to these traditional metal substrates. Chemical adsorption-induced vibrations, metal-catalyzed side reactions, photocarbonization, photobleaching, molecular deformation, and distortion may all hinder the practical application of SERS.[115] Therefore, exploring nonmetallic materials as the substrates for SERS become significantly important in overcoming the disadvantages of metal substrates.

2D materials have attracted increasing attention and are expected to be strong candidates as the substrates for Raman enhancement. 2D materials have a flat and clean surface without dangling bonds, providing an ideal platform for SERS analyses. The enhancement mechanism of 2D materials-based substrates is dominated by chemical mechanism, which makes it easier to study the enhancement theory. The interaction between the probe molecule and 2D materials substrates mainly results from a van der Waals interaction and free from direct chemical bonding. Because 2D materials have an ultra-thin thickness, they can be used as flexible substrates. Besides, the molecular orientation is more convenient to be controlled on 2D materials. 2D materials can be also combined with traditional metal substrates to take advantages of both.

Different type of 2D materials have been studied as SERS substrates, such as graphene, h-BN, MoS_2, WSe_2.[115–120] Copper phthalocyanine (CuPc) and R6G are commonly used as the probe molecules. CuPc has strong Raman scattering and negligible disturbance by the PL background.[116] Due to the diverse structures and properties of 2D materials, the enhancement mechanisms are also different among them. In addition to charge transfer interaction, the dipole-dipole interaction should be also considered.[119] For example, graphene mainly depends on the ground-state charge transfer at the interface, because it is nonpolar.[118,119] TMDs own more complex band structures and abundant electronic states.[118] h-BN has negligible charge transfer interaction but strong dipole interaction at the interface.[119] Figure 4-3 demonstrates the Raman enhancement ability of CuPc on graphene, h-BN, and MoS_2, compared to SiO_2/Si.
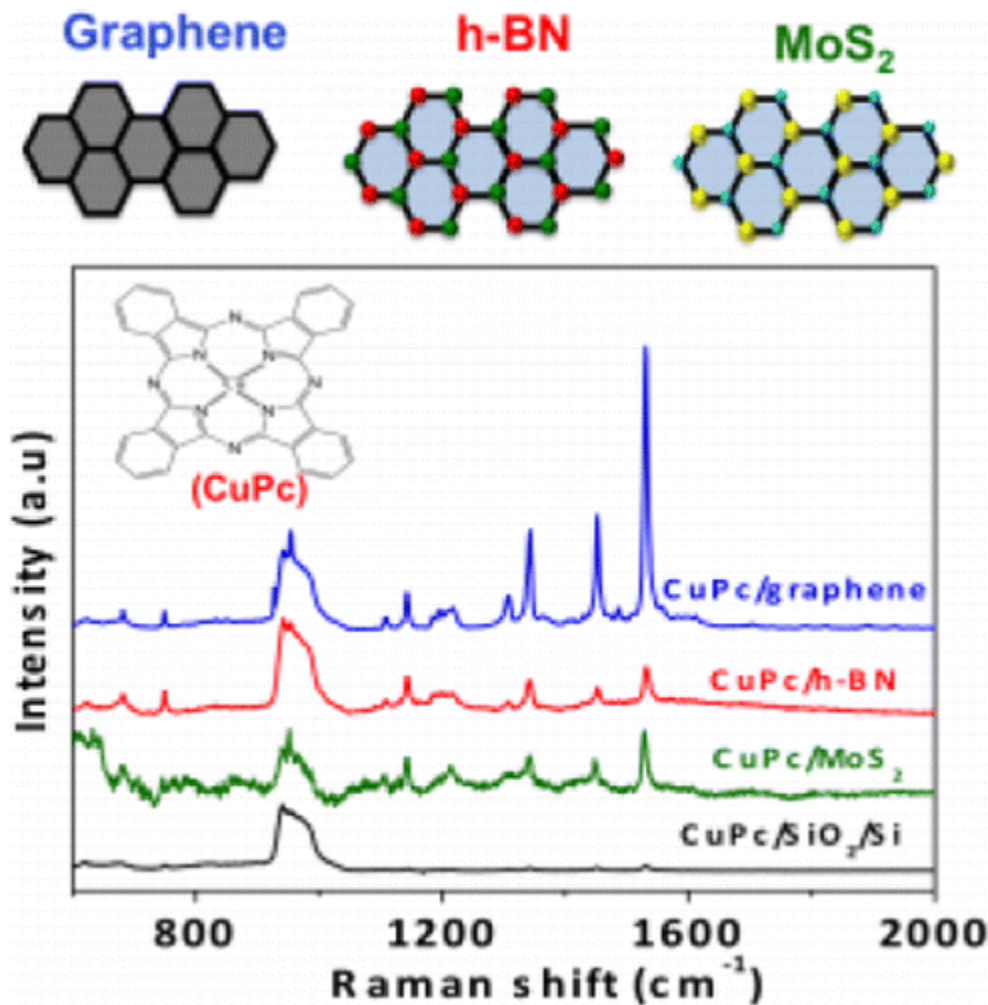
Figure 4-3 – Raman spectra of CuPc molecule on SiO_2/Si substrate, on graphene, on h-BN, and on MoS_2 substates. The Raman signal was excited by a 632.8 nm laser.[119]

In addition to work alone as the substrates, 2D materials can be also functionalized or treated to improve SERS performance. These function groups and surface treatments can modify the doping level of graphene and thus change the Raman enhancement intensity of probe molecules. For example, fluorinated and 4-

nitrophenyl functionalized graphene substrates have been reported to exhibit stronger SERS enhancement for R6G than pristine graphene.[121]

Recently 2D materials based heterostructures have demonstrated their ability as novel Raman enhancement platform. Since the 2D materials are assembled together via the van der Waals force, the electronic structure can be artificially designed due to the interlayer electronic tunneling. For instance, a monolayer graphene was transferred onto a monolayer WSe_2 to form a heterostructure illustrated in Figure 4-4. The SERS enhancement of CuPc molecule was observed on graphene, WSe_2 and graphene/WSe_2 heterostructure, and the enhancement factor is 4.7, 9.9, and 28.6 respectively. Graphene/WSe_2 heterostructure exhibits the highest enhancement factor than the sum of graphene and WSe_2. These results can be attributed to the different interlayer coupling in the heterostructure.[118]
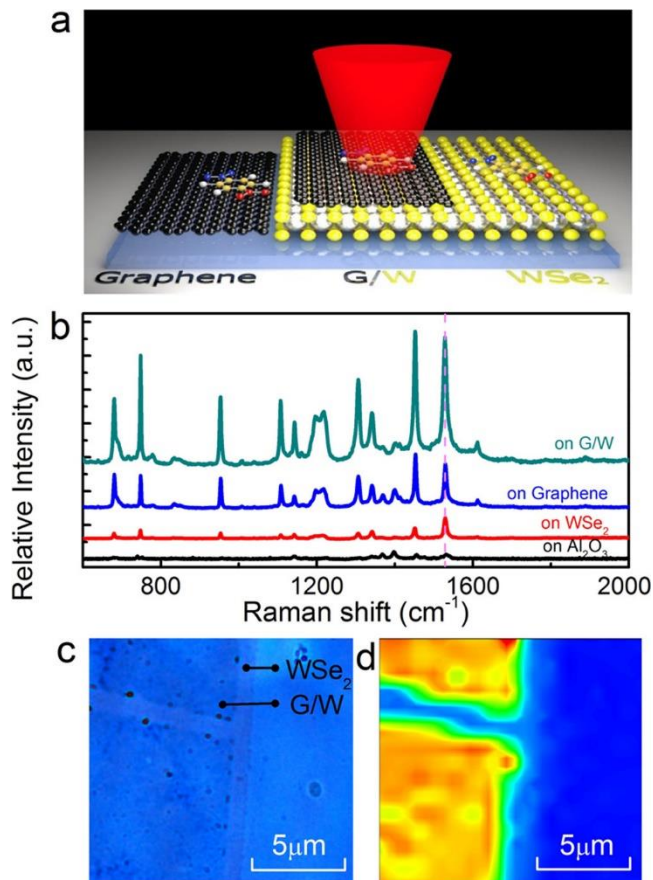
Figure 4-4 – (a) Schematic illustration of the measurement. (b) Raman spectra of CuPc on Al$_2$O$_3$, WSe$_2$, graphene and graphene/WSe$_2$ heterostructure. (c) Optical image of graphene/WSe$_2$ heterostructure. (d) Raman mapping for the CuPc at 1528.3 cm^{-1}.[118]

2D materials can be also combined with a metal substrate to form hybrid SERS substrate. 2D materials can protect metal from oxidation or photoinduced damage, improving the stability and repeatability of analysis. Besides, 2D materials can help map out the hot spots of metal substrates due to their atomic thin thickness and transparency.[122] SERS analysis of these hybrid structures combines chemical

enhancement and electromagnetic enhancement, which is expected to have higher enhancement.

4.2. Experimental results

We have demonstrated in the previous chapter that centimeter-scale $MoTe_2$ films with high uniformity can be synthesized by CVD method. The electrochemical properties of 2H semiconducting phase and 1T' metallic phase are different, which may result in different SERS performance of these two phases. Studying the application of $MoTe_2$ in SERS would be interesting and also can help understand the properties of $MoTe_2$.

$MoTe_2$ films were synthesized by using the same method described in the previous chapter as illustrated in Figure 4-5. To compare the SERS enhancement of $MoTe_2$ with different thickness, 1 nm, 2 nm, 4 nm and 5 nm Mo films were deposited onto sapphire substrates by e-beam evaporation.
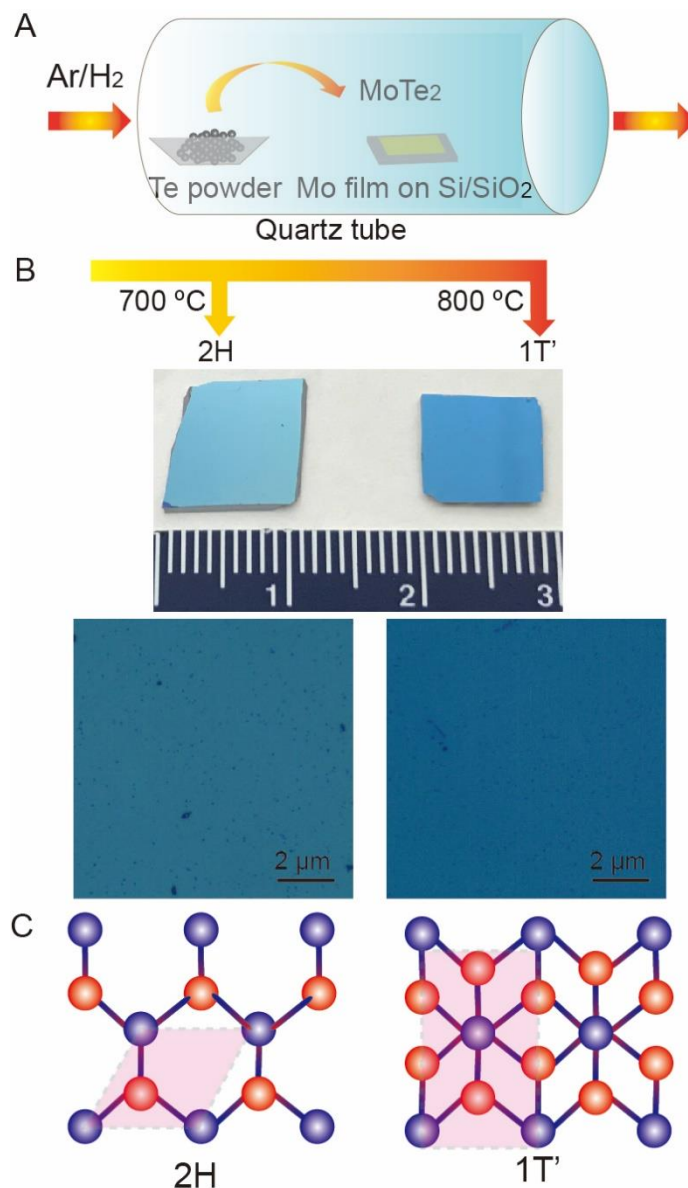
Figure 4-5 – (a) Schematic illustration of the phase-control synthesis of MoTe$_2$ films by CVD methods. (b) Optical images of 2H and 1T' MoTe$_2$. (c) Schematic diagrams of 2H and 1T' MoTe$_2$ structures.

After growth, AFM measurement was conducted on $MoTe_2$ films. Figure 4-6 shows that the thickness of $MoTe_2$ films is 4 nm, 8 nm, 12 nm, and 14 nm. Considering that the interlayer spacing $MoTe_2$ is 0.7 nm, the grown films contain 5, 11, 17 and 20 layers of $MoTe_2$ respectively.
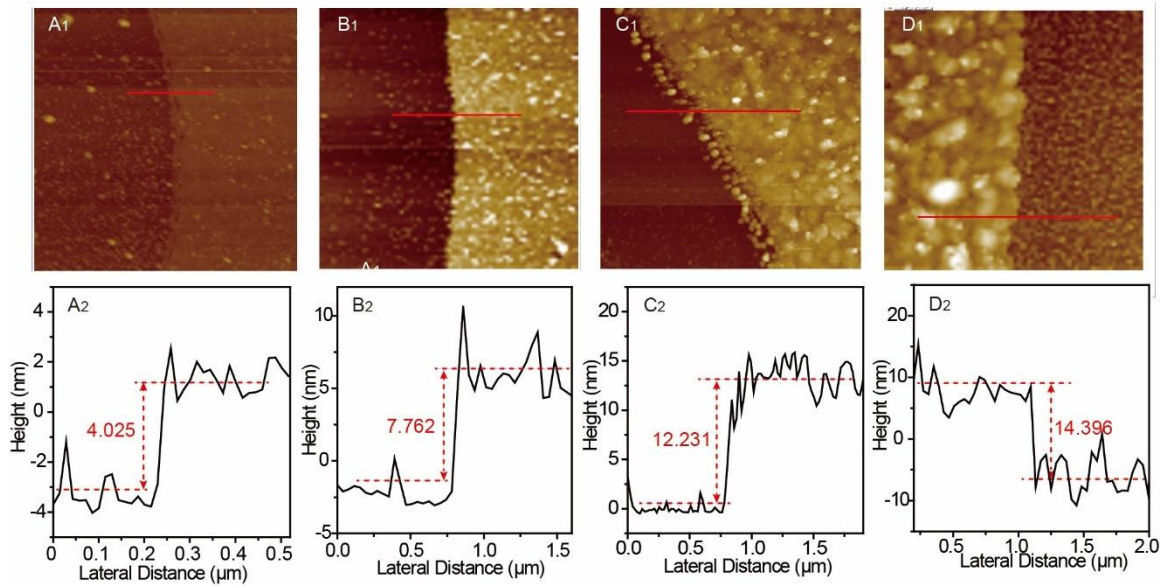
Figure 4-6 - AFM measurement of $MoTe_2$ films with different thickness.

Figure 4-7 exhibits Raman spectra collected on these $MoTe_2$ films using a 532 nm excitation laser.
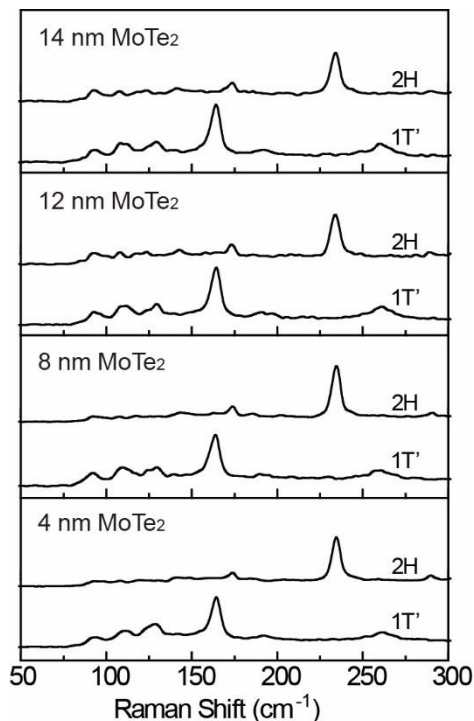
Figure 4-7 – Raman spectra of 2H and 1T' MoTe$_2$ with different thickness.

CuPc was selected as the probe molecule and was deposited onto 2H and 1T' MoTe$_2$ films by e-beam evaporation. The evaporation current is 70 A and the time is controlled as 5 s. Raman spectra were collected by using a 633 nm excitation laser. SERS signals of the CuPc molecule can be detected both on 1T' phase and 2H phase, as displayed in Figure 4-8. It can be clearly observed that the Raman enhancement is different in these two phases, indicating that the crystal structure has a significant impact on SERS performance. Raman enhancement on 1T' MoTe$_2$ is higher than that on 2H MoTe$_2$, while the SERS signal of CuPc on SiO$_2$/Si is weakest.

In the Raman spectra, 1341 cm^{-1} and 1527 cm^{-1} can be attributed to the in the plane full symmetric N-C stretching and ring C-C stretching vibration. Taking CuPc on

SiO$_2$/Si substrate as the reference sample and the peak intensity at 1341 cm^{-1} as the index, the absolute Raman enhancement factors on 1T' MoTe$_2$ and 2H MoTe$_2$ are 9 and 4, respectively. 1T' MoTe$_2$ has an enhancement factor that is two times of magnitude higher than of 2H MoTe$_2$.
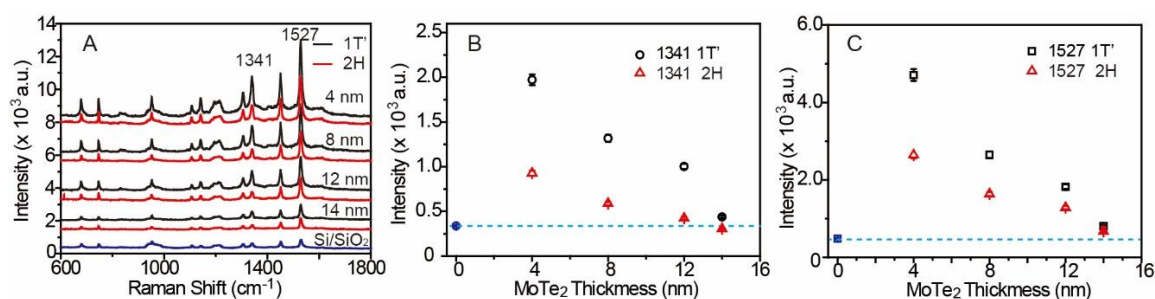
Figure 4-8 – (a) SERS spectra of CuPc molecule on 2H and 1T' MoTe$_2$ with different thickness. (b)(c) Relative intensities of SERS signals from CuPc corresponding to the layer number of the MoTe$_2$ film. Black circles and red triangles represent 1T' and 2H MoTe$_2$, respectively.

To investigate the influence of MoTe$_2$ thickness on SERS enhancement, the intensities of vibrational modes at 1341 cm^{-1} and 1527 cm^{-1} on 2H and 1T' MoTe$_2$ with different thickness are plotted in Figure 4-8 (b) and (c). It can be observed that Raman intensity decreases when the MoTe$_2$ film becomes thicker. The SERS effect is nearly negligible as the thickness of MoTe$_2$ film reaches 14 nm. Both of 2H phase and 1T' phase have the similar thickness-dependent SERS behavior.

To further confirm the SERS enhancement on 1T' and 2H MoTe$_2$ substrates, we also measured the Raman spectra of R6G by immersing the substrates in 10^{-6} M R6G

solution for 30 min. SERS signals of the R6G molecule were detected both on 1T' phase and 2H phase, as displayed in Figure 4-9. Similarly, it can be observed that SERS enhancement on 1T' $MoTe_2$ is stronger than that on 2H $MoTe_2$. The intensities of vibrational modes at 613 cm^{-1} and 1648 cm^{-1} on 2H and 1T' $MoTe_2$ with different thickness are plotted in Figure 4-9 (b) and (c). Raman intensity decreases quite fast with the film thickness increasing. The SERS effect is nearly negligible at 12 nm and 4 nm thick $MoTe_2$. Again, both of 2H phase and 1T' phase have the similar thickness-dependent SERS behavior.
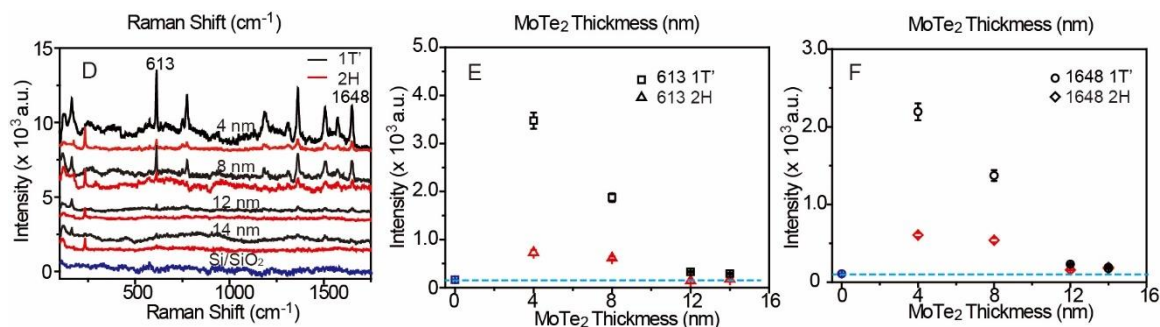
Figure 4-9 - (a) SERS spectra of the R6G molecule on 2H and 1T' $MoTe_2$ with different thickness. (b)(c) Relative intensities of SERS signals from R6G corresponding to the layer number of the $MoTe_2$ film. Black circles and red triangles represent 1T' and 2H $MoTe_2$, respectively.

Since 1T' $MoTe_2$ showed a higher Raman signal enhancement, we further investigated its SERS sensitivity. 1T' $MoTe_2$ films were soaked into the R6G solution at a different concentration from 10^{-5} M to 10^{-8} M for 20 min. The concentration-dependent SERS spectra of R6G on 1T' $MoTe_2$ were displayed in Figure 4-10. It is

thrilling to see the possibility of detecting the R6G molecule at a concentration of 10^{-8} M on 1T' MoTe$_2$, which is comparable to some previous reported metallic substrates.
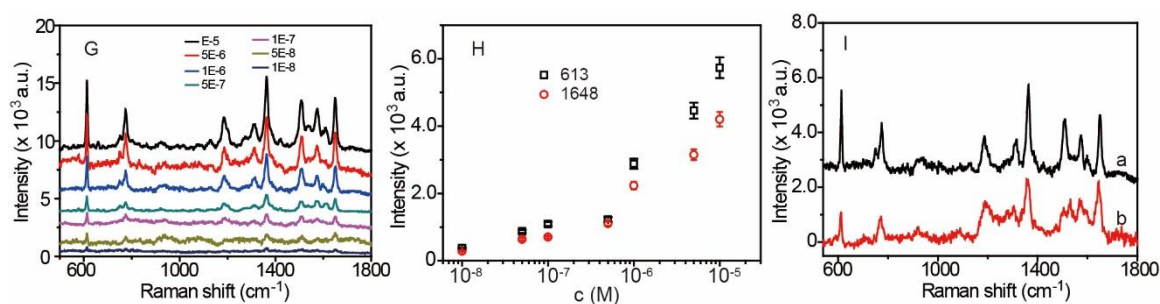
Figure 4-10 - (a) Raman spectra of R6G deposited on 1T' MoTe$_2$ substrate with different concentrations from 10^{-8} M to 10^{-5} M. (b) Raman signal intensity as a function of the R6G concentration. (c) SERS spectra of R6G (10^{-6} M) on 1T' MoTe$_2$ substrate, and Raman spectrum of R6G in solid state excited by 532 and 633 nm laser.

To compare the Raman enhancement ability of MoTe$_2$ and graphene, monolayer graphene was transferred onto 12 nm-thick MoTe$_2$ to form MoTe$_2$/graphene heterostructures. The samples were annealed with H$_2$/Ar as the carrier gas before measurement. The SERS signals of CuPc molecule on graphene and MoTe$_2$/graphene heterostructures are illustrated in Figure 4-11. It can be found that Graphene alone exhibits obvious Raman enhancement of CuPc compared to 1T' and 2H MoTe$_2$. Once graphene is transferred onto MoTe$_2$, the enhancement factor can be improved compared to MoTe$_2$ alone. Interestingly, 1T' MoTe$_2$/graphene shows the best enhancement at 1527 cm^{-1} among all the substrates.
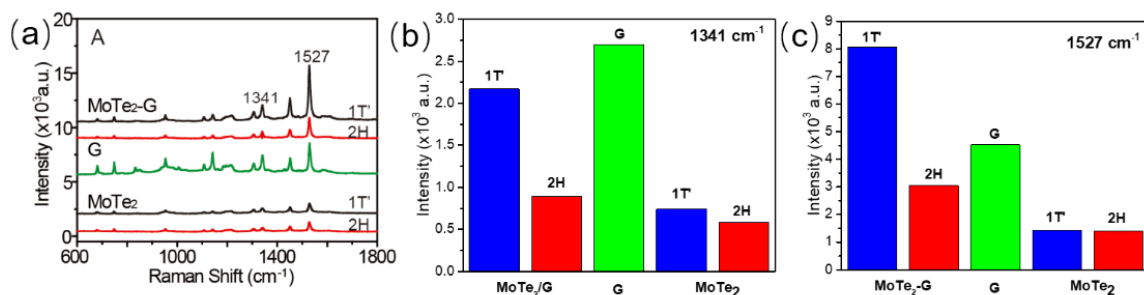
Figure 4-11 - (a) SERS spectra of CuPc on graphene, MoTe₂, and MoTe₂/graphene heterostructures. Comparision of Raman intensities at (b) 1341 cm⁻¹ and (c) 1527 cm⁻¹ on different substrates.

In addition to studying MoTe₂/graphene heterostructure, we also transferred h-BN onto MoTe₂ to explore the SERS performance of an insulating layer on MoTe₂ substrates. The Raman spectra of CuPc molecule on MoTe₂ and MoTe₂/h-BN heterostructures are demonstrated in Figure 4-12. It is very interesting to observe that the SERS enhancement of MoTe₂/h-BN heterostructures is even better than MoTe₂ alone.
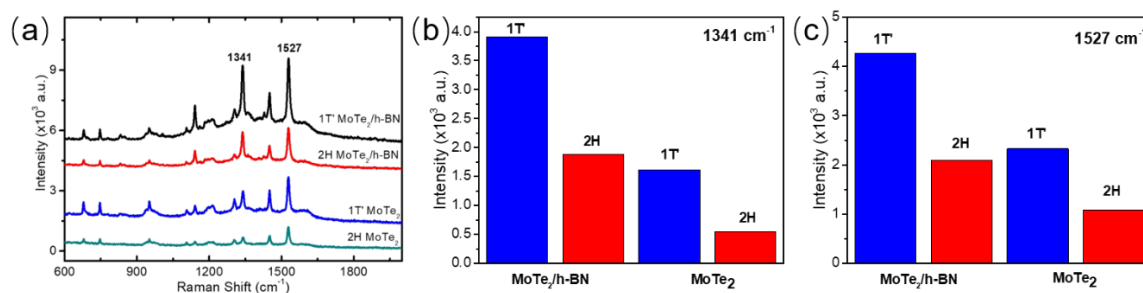
Figure 4-12 – (a) SERS spectra of CuPc on MoTe$_2$ and MoTe$_2$/h-BN heterostructures. Comparision of Raman intensities at (b) 1341 cm^{-1} and (c) 1527 cm^{-1} on different substrates.

MoTe$_2$/graphene and MoTe$_2$/h-BN heterostructures not only improve the Raman enhancement of MoTe$_2$, but also can prevent MoTe$_2$ from damage or degradation.

4.3. Theoretical simulation

To explain the SERS enhancement results, DFT calculation of the band structures of the substrates have been conducted. The crystal structures of MoTe$_2$, graphene on MoTe$_2$ and h-BN on MoTe$_2$ are illustrated in Figure 4-13 (a-c). Their electrical structures (black line) and Fermi levels (red line) are demonstrated in Figure 4-13 (d) together with the conduction band and valence band (green line) of CuPc. Since 1T' MoTe$_2$ is metallic and 2H MoTe$_2$ is semiconducting, the charge transfer interaction between CuPc and 1T' phase is stronger than that between CuPc and 2H phase. Thus 1T' MoTe$_2$ exhibits better SERS performance than 2H MoTe$_2$.

When graphene is transferred onto MoTe$_2$, the CuPc molecule has the surface interaction with graphene. However, the electronic state density of graphene is modified by MoTe$_2$ through the interlayer coupling. The modified Fermi levels of graphene/2H MoTe$_2$ and graphene/1T' MoTe$_2$ both increase compared to those of 2H MoTe$_2$ and 1T' MoTe$_2$, respectively. However, the interaction between graphene and 2H MoTe$_2$ opens a small gap, making the graphene behave like a semiconducting. Therefore, the sequence of enhancement factor of these substrates is Graphene/1T' MoTe$_2$ > Graphene>Graphene/2H MoTe$_2$.
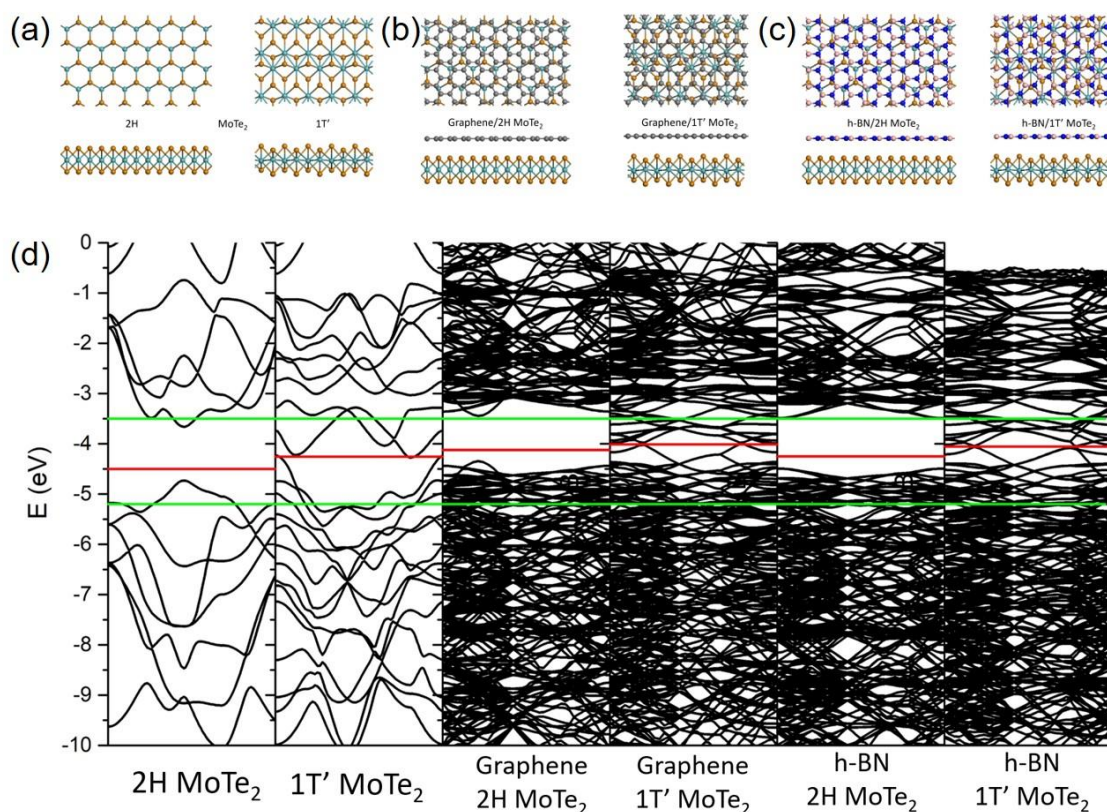
Figure 4-13 – (a-c) Crystal structures of MoTe$_2$, graphene/MoTe$_2$ and h-BN/MoTe$_2$. Both 2H phase and 1T' phase of MoTe$_2$ have been considered. (d)

Band structure (black) and Fermi level (red) of all the substrates. The conduction band and valence band (green) of CuPc are also displayed.

4.4. Conclusion

In this work, we studied the Raman enhancement on CVD-synthesized large-scale thin 2H and 1T' MoTe2 films. By using CuPc as the probe molecule, the SERS signals become stronger significantly with a phase-transition from 2H phase to 1T' phase and with a decreasing number of layers of $MoTe_2$. We also explored the $MoTe_2$ based heterostructures as novel platforms for SERS enhancement. After transferring monolayer graphene on relatively thick 2H and 1T' $MoTe_2$, the surface Ramen enhancement signals recovered, and the band at 1527 cm^{-1} recorded from 1T' $MoTe_2$/Graphene was two times stronger than that of graphene alone, whereas other bands were weaker than these on graphene. After transferring monolayer h-BN, the SERS performance of $MoTe_2$/h-BN was surprisingly better than that of $MoTe_2$. The reason for these phenomena was explained by the DFT calculation. This work not only reveals the origin of the Raman enhancement and identifies large-scale $MoTe_2$ films as potential enhancement substrates, but also paves a way for designing new 2D SERS substrates via phase-transition engineering.

Chapter 5

Spatial Phase-targeted Synthesis of 2H and 1T' MoTe$_2$

5.1. Introduction

In the previous chapters, we have demonstrated a series of interesting properties and applications of MoTe$_2$. The CVD method makes it possible to grow large-scale MoTe$_2$ with controlled phase. However, the current synthesis methods are still insufficient for practical application. The distribution of 2H and 1T' phase on an as-synthesized MoTe$_2$ film is basically random, which can't be predicted before growth. Therefore, a spatial phase control method becomes significant to this field. In this chapter, I will first review the current research progress on phase engineering of TMDs. Next, I will demonstrate our strategy to selectively synthesize 2H and 1T' MoTe$_2$.

TMDs would have a phase transformation from 2H phase to 1T phase through alkali metal intercalation. Dines[123] first reported that n-Butyllithium in hexane solution can serve as a reagent to realize the intercalation of lithium into Group IV

and V TMDs. Py and Haering[124] further studied the structural transformation induced by lithium intercalation in MoS_2. The driving mechanism was found to be a charge transfer from the lithium solution to the structure of MoS_2. As a result, the electron density of the d orbital of Mo increases. The reaction is

$$MX_2 + xLiC_4H_9 \rightarrow Li_xMX_2 + \frac{x}{2}C_8H_{18}$$
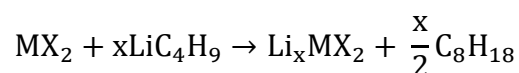
The lithium intercalation process was achieved by immersing MoS_2 in n-butyllithium solution in hexane for a certain period of time in Ar atmosphere, and a series of steps to remove extra lithium and other byproducts.[93,125] Figure 5-1 shows a monolayer MoS_2 that has been partially converted to 1T phase. The interface between 2H and 1T phases is found to be sharp. Before the conversion, PMMA was spin-coated onto the sample. The PMMA on the desired phase-transition region was removed by e-beam lithography.
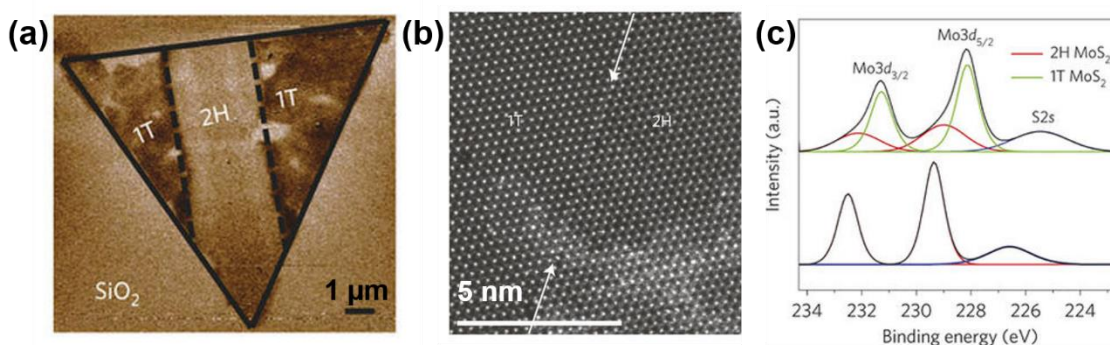
Figure 5-1 – (a) Electrostatic force microscopy phase image of a monolayer MoS_2. (b) High-resolution transmission electron microscope image of a phase

boundary. (c) XPS spectra of the Mo3d and S2s peaks of the 1T and 2H phases of MoS$_2$.[93]

In situ observations of the phase transformation from 2H phase to 1T phase was reported by Lin et al.[126] The MoS$_2$ sample doped with 0.6 at% Re was transferred to a TEM grid, which was then heated at high temperature to promote the phase transition. Figure 5-2 demonstrates that the phase of MoS$_2$ changes over the irradiation time. The initial MoS$_2$ shows 2H phase, while two identical band-like structure or α phase appears at 100 s. When two non-parallel α phases gradually grow and come across, a triangular 1T phase forms at 110 s. The size of 1T phase becomes larger with continuous e-beam irradiation. Meanwhile, β phase and γ phase appear at the edges of the 1T phase.
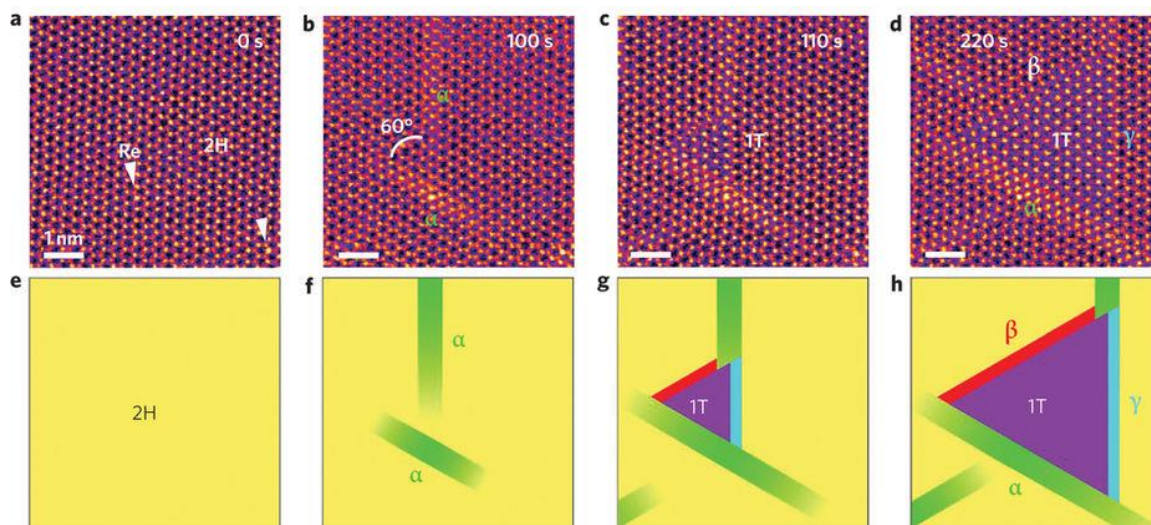
Figure 5-2 – (a) Re doped MoS$_2$ has the initial 2H phase. (b) α phases form with an angle of 60° at 100s. (c) 1T phase appears at 110s. (d) Transformed 1T

phase becomes larger. α phase, β phase, and γ phase are found at the edges between 2H and 1T phase. (e-h) Schematic illustrations of the 2H to 1T phase transition.[126]

E-beam irradiation can precisely introduce the phase transition in the desired areas with accurate size. However, these structures have been fabricated only in an electron microscope. Transferring the samples to other substrates, preventing the surface from contamination are still waiting to be solved.

As introduced in the previous chapter, laser-induced phase patterning of $MoTe_2$ has been investigated by Cho el at.[42] 2H $MoTe_2$ was exposed to the laser with a power of 26 mW for 10 s. The laser irradiation can decrease the flake thickness and further achieve a phase transition from 2H to 1T' in the irradiated region. STEM detected Te vacancies in the transformed 1T' $MoTe_2$, indicating that the phase transition originates from the Te vacancies.
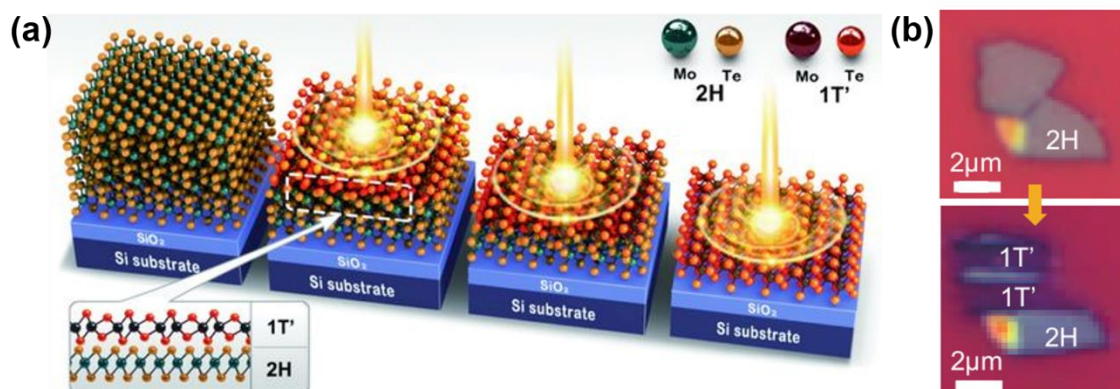
Figure 5-3 - (a) Schematic illustration of the laser irradiation process. (b) Optical images of an exfoliated 2H MoTe₂ flake before and after laser irradiation.[42]

It has been predicted in theory that phase transition can be achieved by applying strain on the TMD structure.[19] Song et al.[101] reported the 2H to 1T' phase transition is observed on MoTe₂, which is reversible after the release of strain (Figure 5-4). 2H MoTe₂ was transferred onto a Si substrate with cavities, where a contact force of 200 nN corresponding to 0.2% of strain was applied. The Raman spectra taken at the suspended regions shows 1T' peaks, while the supported region still remains 2H phase. It turned out that the phase transition is not uniform in the partially suspended regions. The authors further found that the required contact force can be reduced by increasing the temperature.
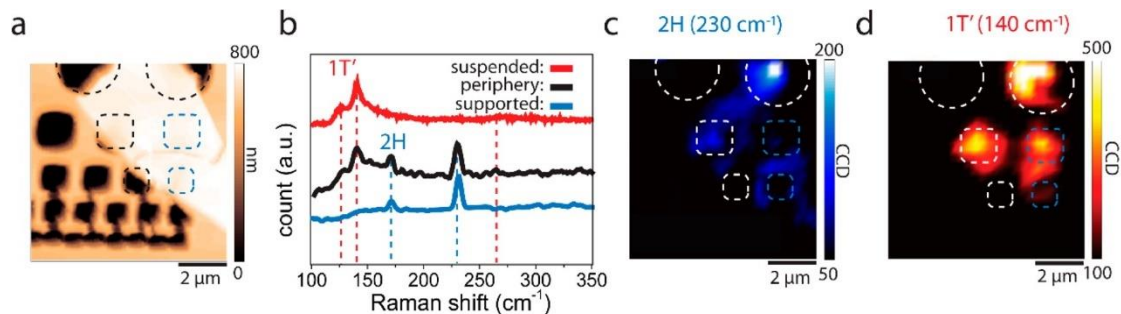
Figure 5-4 – (a) AFM image of the suspended 2H MoTe$_2$ flake. Circles (squares) outline the cavities partially (fully) covered by MoTe$_2$. (b) Raman spectra were taken at the suspended regions, periphery, and the supported regions. Raman intensity mapping near (c) 230 cm^{-1} (2H) and 140 cm^{-1} (1T').[101]

It has been proven that MoTe$_2$ is more stable in the 2H structure under ambient conditions, whereas WTe$_2$ is stable as the semimetallic 1T' phase at a charge neutral condition. Therefore, an appropriate mixing of MoTe$_2$ and WTe$_2$ is expected to achieve a state where either 2H phase or 1T' phase of the alloy is more stable.

Duerloo et al.[127] presented the stable or diffusional phase diagram, and the metastable or diffusionless diagram of Mo$_{1-x}$W$_x$Te$_2$ alloy, as displayed in Figure 5-5 (a) and (b). The first diagram follows the thermodynamically stable convex hull, while the second diagram is valid when W diffusion is quenched. In Figure 5-5 (a), point 1 shows a single phase 2H and point 2 exists in 1T' phase. Two phases can coexist between point 1 and 3. In Figure 5-5 (b), point 2 is the transition point between single phase 2H and single phase 1T'. Zhang et al.[128] calculated the formation energy of Mo$_{1-x}$W$_x$Te$_2$ alloy at various concentration x. A crossing point in Figure 5-5 (c) is located

at x = 0.333. Thus, when x < 0.333, 2H phase is more stable, while x > 0.333, T phase is more stable.
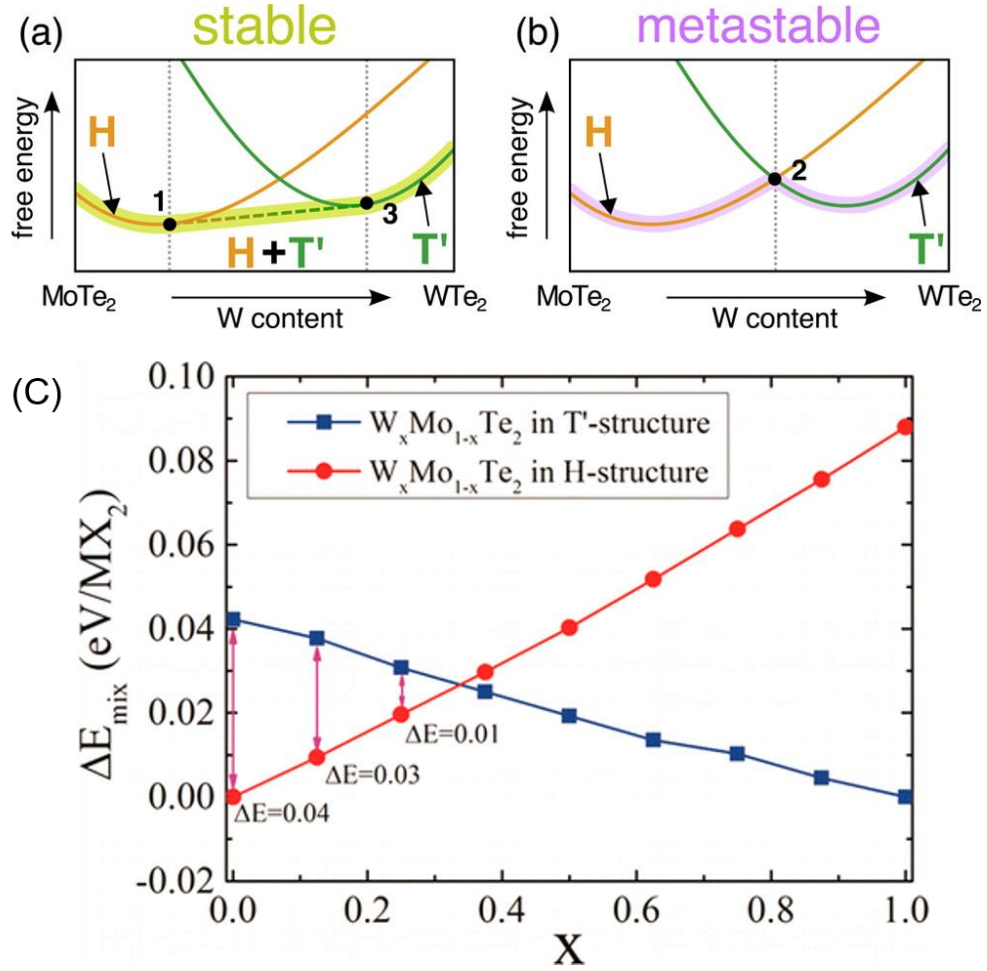
Figure 5-5 - (a) The stable or diffusional phase diagram and (b) the metastable or diffusionless phase diagram of Mo$_{1-x}$W$_x$Te$_2$ alloy.[127] (c) Formation energy of Mo$_{1-x}$W$_x$Te$_2$ alloy in 2H phase (red) and in 1T' phase (blue).[128]

Experimentally, Rhodes et al[129] synthesized bulk crystals of Mo$_{1-x}$W$_x$Te$_2$ alloys by chemical vapor transport technique and characterized their structure of a various

composition. Figure 5-6 (a) and (b) show the Raman spectra of $Mo_{1-x}W_xTe_2$ for various values of x. A structural phase transition is observed in the spectrum when x = 0.09, indicating that 1T' phase becomes more stable than 2H phase after x > 0.09. In addition, the authors didn't observe any phase coexistence in alloy samples.
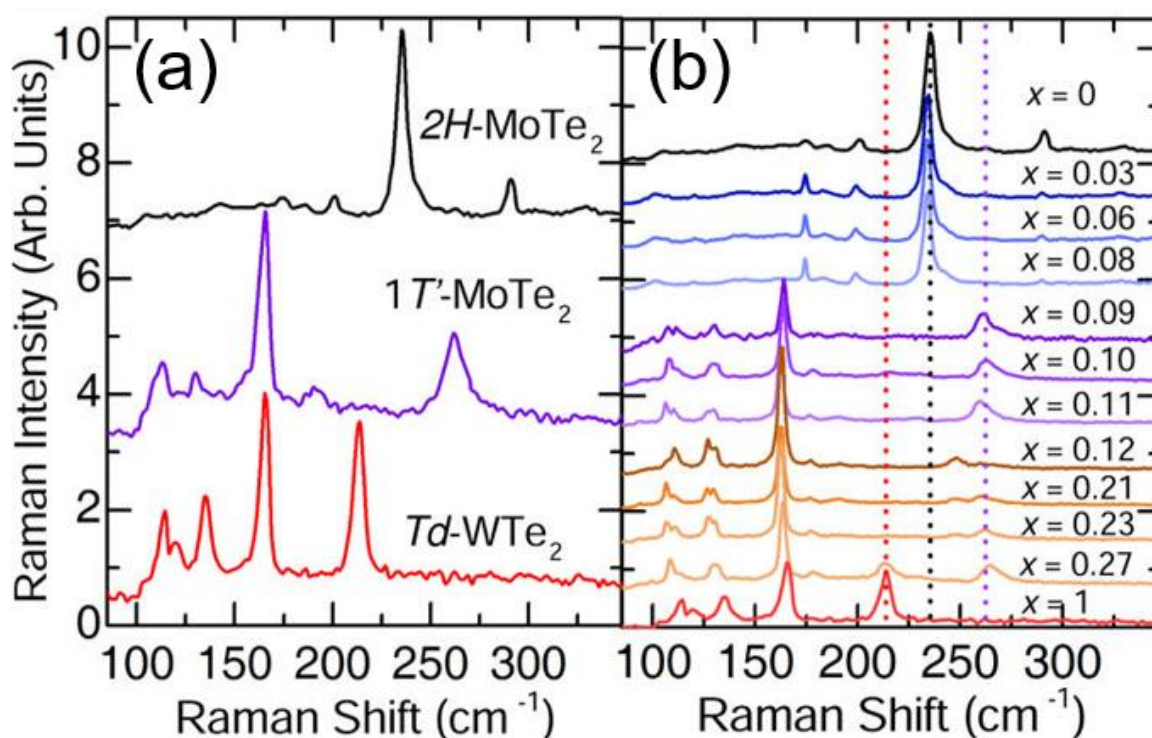
Figure 5-6 – (a) Raman spectra of bulk 2H MoTe₂, 1T' MoTe₂ and Td WTe₂. (b) Raman spectra of $Mo_{1-x}W_xTe_2$ for various values of x.[129]

We also studied the phase evolution of $Mo_{1-x}W_xTe_2$ by tellurizing Mo and W superlattice films. Mo and W superlattice films displayed in Figure 5-7 (a) were deposited by e-beam evaporation. The total film thickness is 5 nm. The thickness of Mo and W layer repeats every 1 nm. The simplified percentage of W can be calculated

as the value of W thickness in every 1 nm. For example, if 0.95 nm Mo and 0.05 nm W are deposited periodically, the simplified percentage of W is 5%.

Mo and W superlattice films with various W percentage were tellurized at the same condition, 600 °C for 2 hours. The Raman spectra obtained at synthesized $Mo_{1-x}W_xTe_2$ films was demonstrated in Figure 5-7 (b). It can be observed that 2H phase dominates in $Mo_{0.96}W_{0.04}Te_2$, whereas 2H/1T' mixed-phase appear in $Mo_{0.95}W_{0.05}Te_2$. As the W percentage increases to 10% and 25%, only 1T' phase is detected. Our experimental results confirm that W doping plays a significant role in phase engineering. The critical percentage of W here is 5%, at which 2H and 1T' phase coexist. When W percentage is less than 5%, only 2H phase can be formed. When W percentage is larger than 5%, only 1T' can be formed.
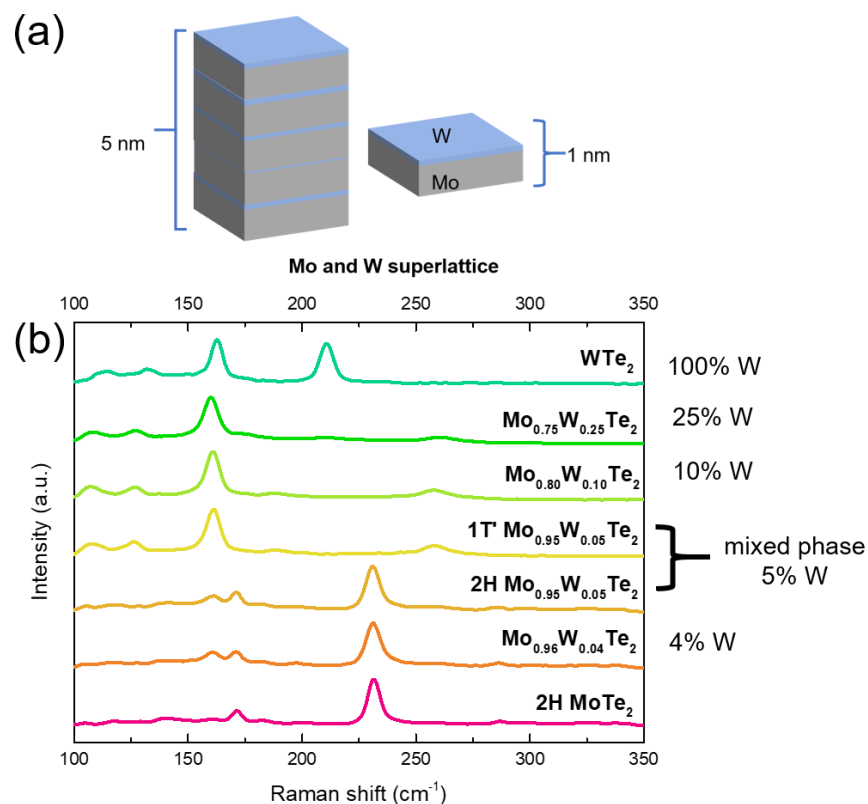
Figure 5-7 – (a) Schematic illustration of Mo and W superlattice structure. (b) Raman spectra obtained at synthesized $Mo_{1-x}W_xTe_2$ films, x are 0, 4%, 5%, 10%, 25% and 100%.

In summary, chemical interaction, e-beam irradiation, laser irradiation and strain engineering can be categorized as the post-patterning methods. All of them modify the phase of materials after synthesis. Although they have been proved to be effective, the drawbacks are also obvious. Lithium intercalation requires the immersion of samples in solution in Ar atmosphere or glove box. E-beam irradiation can be only manipulated in the electron microscope. The sample transfer after

irradiation remains difficult. Laser irradiation and strain engineering don't need demanding conditions. But it is challenging for them to create uniform and precise features. Another disadvantage of all these methods above is that they are only designed to change the phase locally, but not suitable for large-scale application. Doping or alloying method has already been adopted to produce bulk crystals. However, the location of each phase is not controllable, or the phase coexistence may not exist. Thus, it is of great importance to developing a practical way to pattern the phase of $MoTe_2$ spatially.

5.2. Synthesis method

Our strategy for phase patterning of 2H and 1T' $MoTe_2$ is quite simple, which is illustrated in Figure 5-8. The photoresist was spin-coated on a SiO_2/Si substrate, followed by UV light exposure that allows the photoresist on the selected region to be removed during the developing process. A very thin W layer (0.5 - 1 nm) was deposited on the substrate by sputtering. The lift-off process removed unwanted W from the substrate. After that, a layer of Mo (2 nm) was sputtered to the entire substrate.

The Mo/W pattern was loaded to the center of a quartz tube in a tube furnace, where a ceramic boat containing Te power was placed upstream. Carrier gas 15% H_2/Ar was kept flowing for the entire synthesis process and opened 20 min before

furnace turning on. The quartz tube was heated up to 600 ℃ and remained at 600 ℃

for 2 h before cooling down.
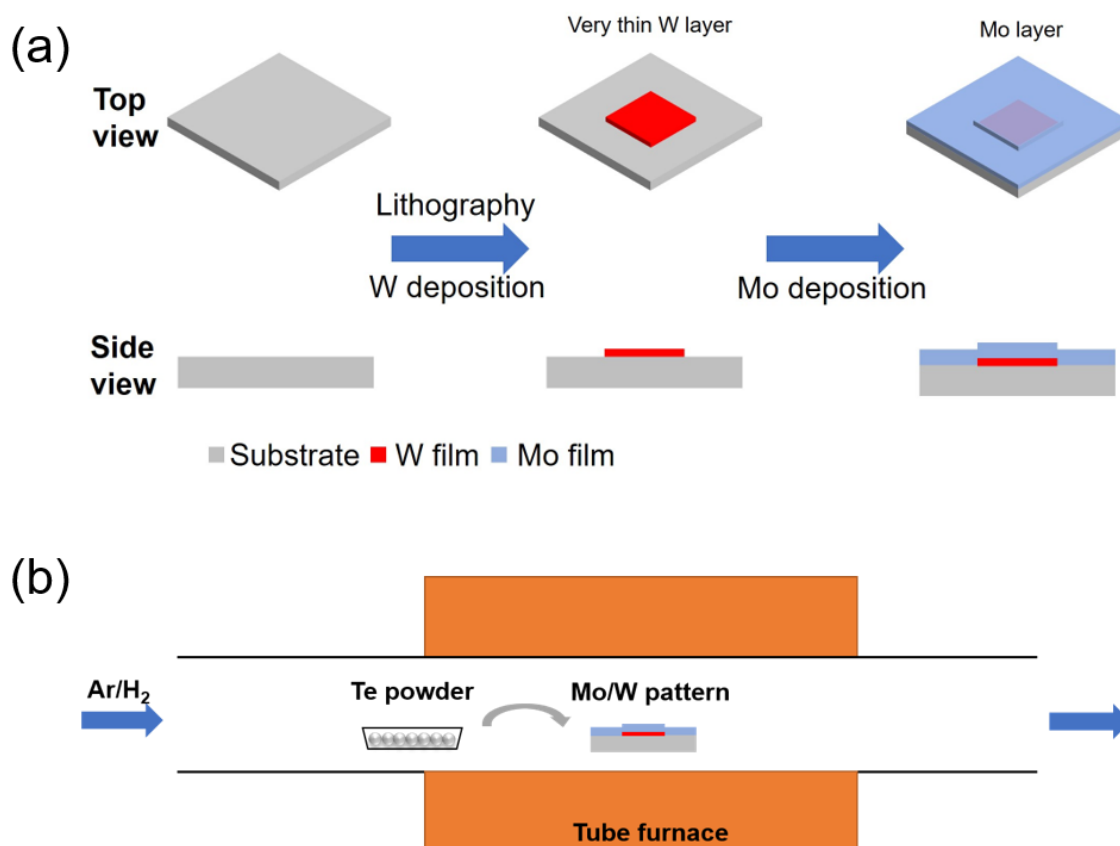
Figure 5-8 - Schematic diagram of spatially phase patterning. (a) With the help of lithography, a very thin W layer was deposited onto the selective area. Mo film was then sputtered to cover the entire substrate. (b) The Mo/W pattern and a boat containing Te powder were placed into a quartz tube in a furnace.

H₂/Ar was used as the carrier gas and kept flowing for the entire synthesis process.

5.3. Characterization

Synthesized films were characterized by Raman spectroscopy, AFM, SEM, XRD, XPS, TEM, high-angle annular dark field (HAADF), and energy-dispersive X-ray spectroscopy (EDX).

Figure 5-9 (a) shows an optical image of Mo/W pattern substrate. The square area is the center contains Mo on top of W, while all the other area in the image is covered only by Mo. After growth, the same region is displayed in Figure 5-9 (b), where the color contrast between the square area and other area is more visible than before. Raman spectrum taken at point 1 and point 2 shows different modes, which are demonstrated in Figure 5-9 (c) and (d), respectively. A_u (~109 cm^{-1}), A_g (~128 cm^{-1}), B_g (~160 cm^{-1}), and A_g (~263 cm^{-1}) are observed in the Raman spectra of point 1, indicating 1T' phase MoTe₂ is formed. E_{1g} (~118 cm^{-1}), A_{1g} (~170 cm^{-1}), E_{2g}^1 (~231 cm^{-1}), and B_{2g}^1 (~286 cm^{-1}) are observed in the Raman spectra of point 2, indicating 2H phase MoTe₂ is formed.
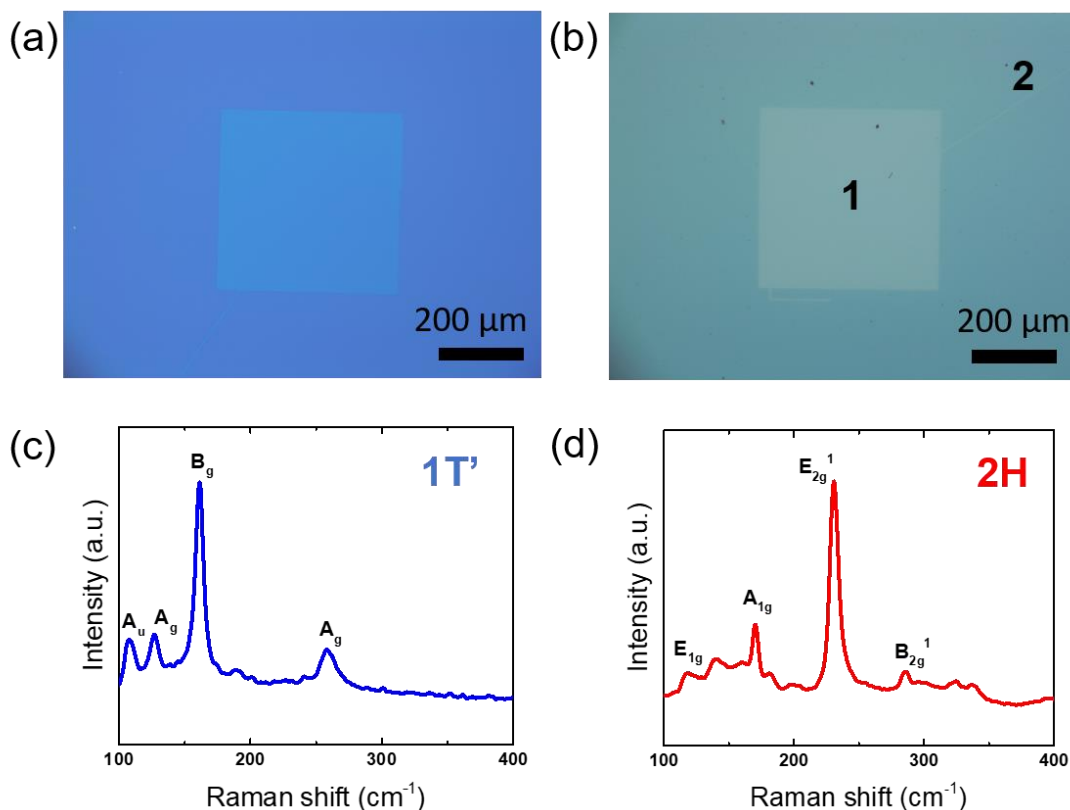
Figure 5-9 – Optical images of a region (a) before growth and (b) after growth. (c) Raman spectra were taken at point 1 in (b) shows characteristic peaks of 1T' MoTe₂. (d) Raman spectra taken at point 2 in (b) shows characteristic peaks of 2H MoTe₂.

To further examine the uniformity of the distribution of 2H and 1T' phase, Raman intensity mappings at 231 cm^{-1} (E_{2g}^1 for 2H) and 160 cm^{-1} (B_g for 1T') were carried out at the edge of the square area, as displayed in Figure 5-10. It is clear that the area inside the square has the strongest and uniform signal for 1T' phase, while the area out of square exhibits the strongest and also a uniform signal for 2H phase.
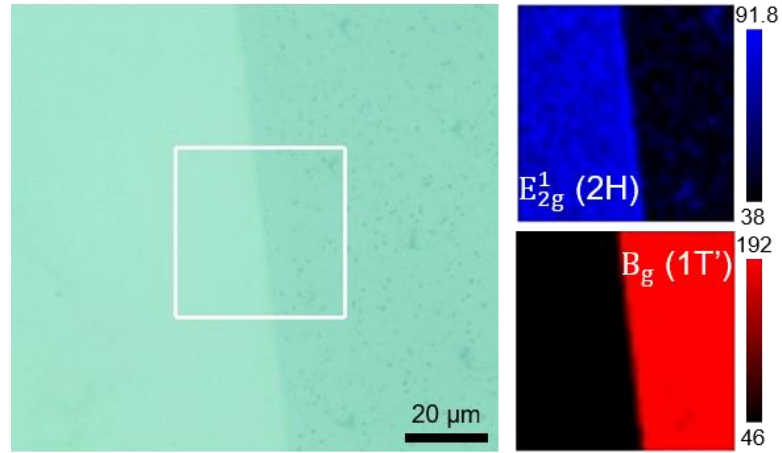
Figure 5-10 – Raman intensity mapping at the edge of the square.

To characterize the thickness of the film, AFM measurement was performed near the edge of the square along the green line in Figure 5-11 (a). Since there is a small pinhole on the line, the thickness of the 2H phase area can be measured to be 7 nm as shown in Figure 5-11 (b). The 1T' phase area is thicker and also has higher surface roughness than the 2H phase area, which should be attributed to the W layer deposited on the bottom. The AFM profile shows that the interface between 2H and 1T' phase is sharp in micro-scale, which can be further confirmed by SEM image in Figure 5-11 (c).
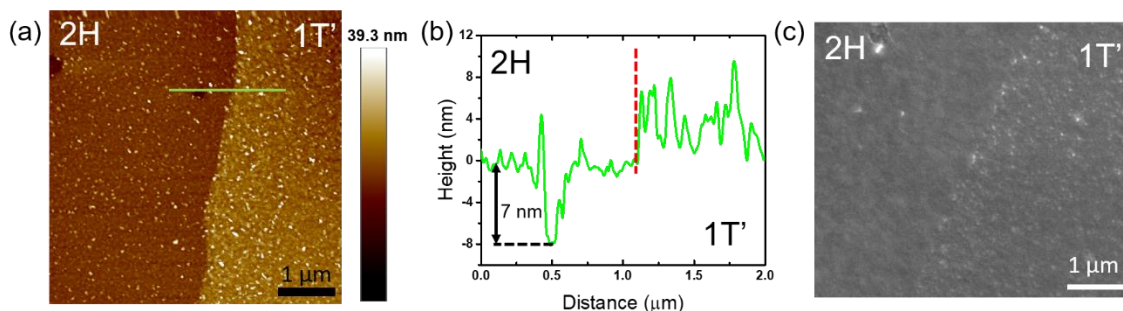
Figure 5-11 – (a) AFM measurement at the edge of the square. (b) The thickness of 2H area is around 7 nm, while the 1T' area is a few nm thicker. 1T' area also has a rough surface. (c) SEM image of the interface between 2H and 1T' regions.

In addition to fabricating these patterned films above, two films without any pattern were also prepared by the same method, one is a complete 2 nm Mo on 0.5 nm thick W film, another is a complete 2 nm thick Mo film. The CVD synthesis process was kept consistent. The synthesized film from Mo/W structure was observed to have the Raman characteristic of 1T' $MoTe_2$, the same as the spectra in Figure 5-9 (c). Besides, the $MoTe_2$ film grown from the complete Mo film exhibits 2H phase. These films were checked with XRD to examine the crystal structures.

Figure 5-12 shows normalized XRD patterns of the 1T' and 2H $MoTe_2$ films. Only the (002), (004), (006), and (008) planes were detected, indicating that both of them are highly textured along the c axis. Besides, the 2θ angles of all the planes of 2H phase are slightly smaller than those of 1T' phase, implying that inter-planar distance

of 2H phase is larger than that of 1T' phase. These results agree well with previous studies on pure $MoTe_2$.[48,49,55]
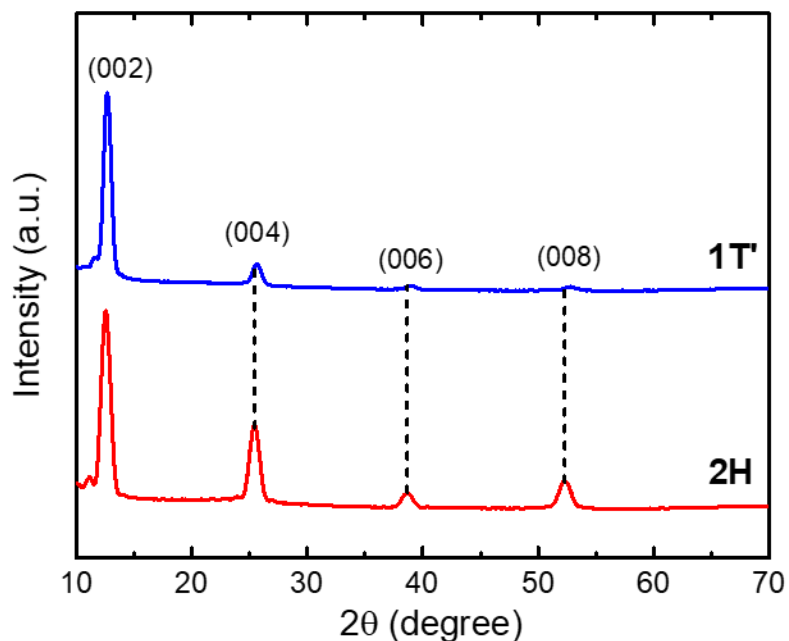
Figure 5-12 – XRD patterns of 1T' and 2H MoTe$_2$. (002), (004), (006), and (008) planes were detected on both samples.

XPS was used to study the elemental composition of the synthesized films. Figure 5-13 shows Mo 3d and Te 3d peaks detected from the surface of 2H and 1T' $MoTe_2$ films. The XPS peaks for 2H phase were observed at 228.4 eV (Mo $3d_{5/2}$), 231.6 eV (Mo $3d_{3/2}$), 573.1 eV (Te $3d_{5/2}$), and 583.4 eV (Te $3d_{3/2}$). For 1T' phase, these peaks were observed at 228.2 eV (Mo $3d_{5/2}$), 231.4 eV (Mo $3d_{3/2}$), 572.8 (Te $3d_{5/2}$), and

583.2 eV (Te 3d$_{3/2}$). The peak binding energy of 2H phase is 0.2~0.3 eV higher than that of 1T' phase.
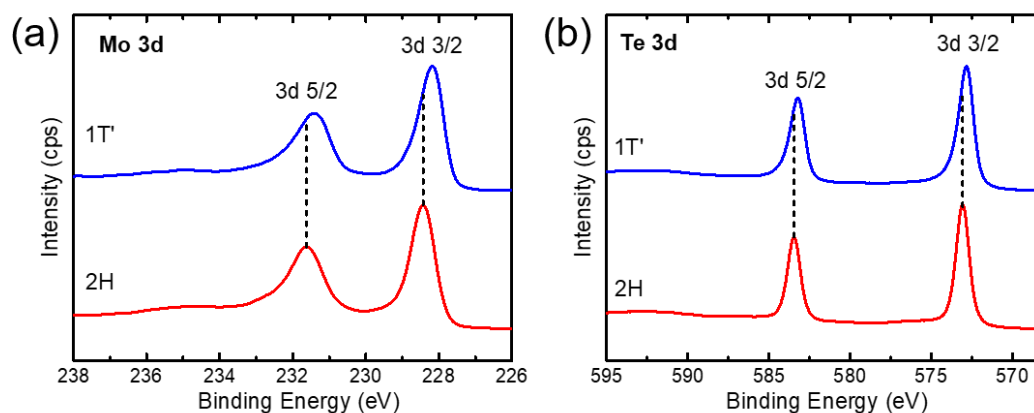
Figure 5-13 – Mo 3d and Te 3d in the XPS spectra of 2H and 1T' MoTe$_2$ films.

To shed light on the element composition of the film, an XPS depth profiling was performed on the 1T' MoTe$_2$ film with the assist of Ar ion etching. Figure 5-14 shows Mo 3d, Te 3d, and W 4d peaks detected at three points, A, B and C. A is on the surface, B is in the middle, while C is at the bottom. It can be observed that the amount of W atom is really small on the surface (point A), becomes larger in the middle (point B) and at the bottom (point C). Most of Mo and Te atoms stay on the surface (point A) and in the middle (point B). Very few of them were detected on the bottom (point C). The results indicate that the distributions of Mo, Te, and W atom are different from surface to bottom.
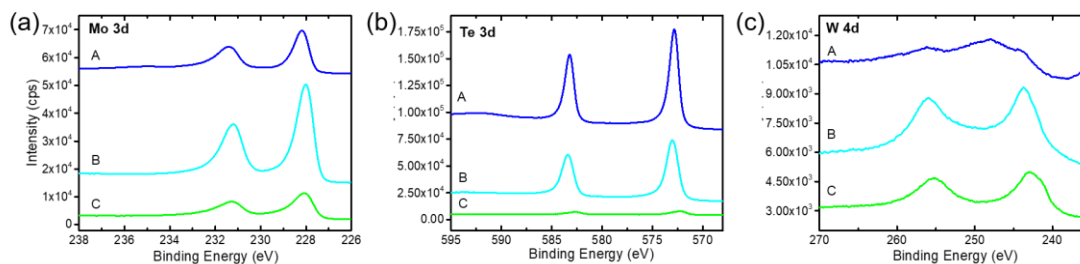
Figure 5-14 – XPS depth profiling study of a 1T' MoTe$_2$ film. Point A, B, C are located on the surface, in the middle and at the bottom, respectively. Mo, Te and W atoms display different distribution.

The crystallographic structure of the synthesized 2H/1T' MoTe$_2$ heterostructure was studied with TEM. Figure 5-15 (a) shows a low magnification high-angle annular dark field (HAADF) image taken at the interface between 2H and 1T' phases. The 1T' area looks rougher than the 2H area, which is consistent with our previous results measured by AFM and SEM. Figure 5-15 (b) and (c) are high-resolution TEM (HRTEM) images of 2H and 1T' phase areas, respectively. Spatially resolved elemental EDX mappings of Mo, Te and W are presented in Figure 5-15 (d-f), respectively. The distributions of Mo and Te are uniform in both 2H phase area and 1T' phase area. The density of W in 1T' phase area is higher than that in 2H phase area. Although W layers were only deposited on the selective regions or the 1T' phase areas, there are still some W atoms existing in the 2H phase area, which can be attributed to lateral diffusion.
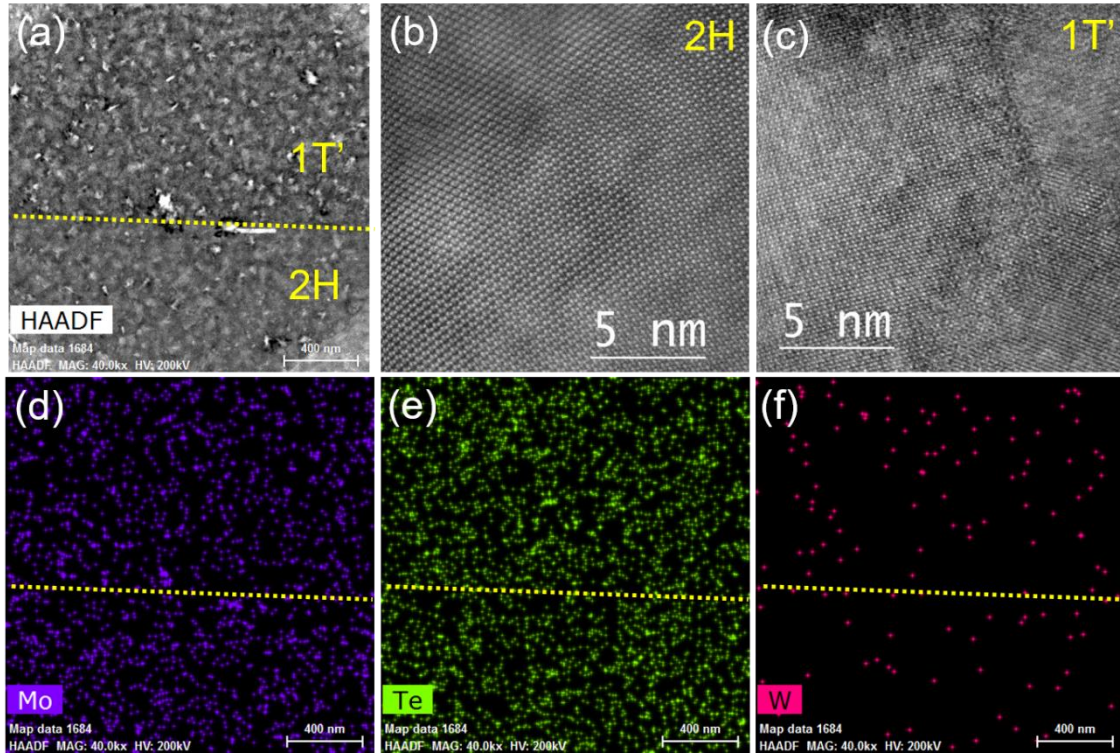
Figure 5-15 – TEM analysis of 2H/1T' MoTe₂ heterostructure. (a) a low magnification high-angle annular dark field (HAADF) image taken at the interface between 2H and 1T' phases. (b) HRTEM image of a 2H phase area. (c) HRTEM image of a 1T' phase area. (d) (e) (f) HAADF-EDX mappings for MO, Te, and W, respectively

5.4. Application

The characterization results above have confirmed that our strategy for spatially phase patterning of 2H and 1T' MoTe₂ is reliable. Next, we will make use of this technique and explore more applications.

Since the phase configuration is defined by lithography, a variety of masks were used to create different patterns. Figure 5-16 (a) presents an optical image of a millimeter-sized sketch of an owl (the symbol of Rice University). The owl contour (point 1) is designed with Mo on W, and the remainder (point 2) is Mo. After synthesis, the optical image is displayed in Figure 5-16 (b). The Raman spectra taken at point 1 and point 2 indicate that 1T' phase and 2H phase have been formed respectively. Figure 5-16 (c) is a higher magnification optical image taken near the tip of owl's nose. Raman intensity maps at B_g for 1T' phase and E_{2g}^1 for 2H phase are demonstrated in Figure 5-16 (d) and (e) respectively, implying the distribution of 1T' and 2H phases has been well-controlled.
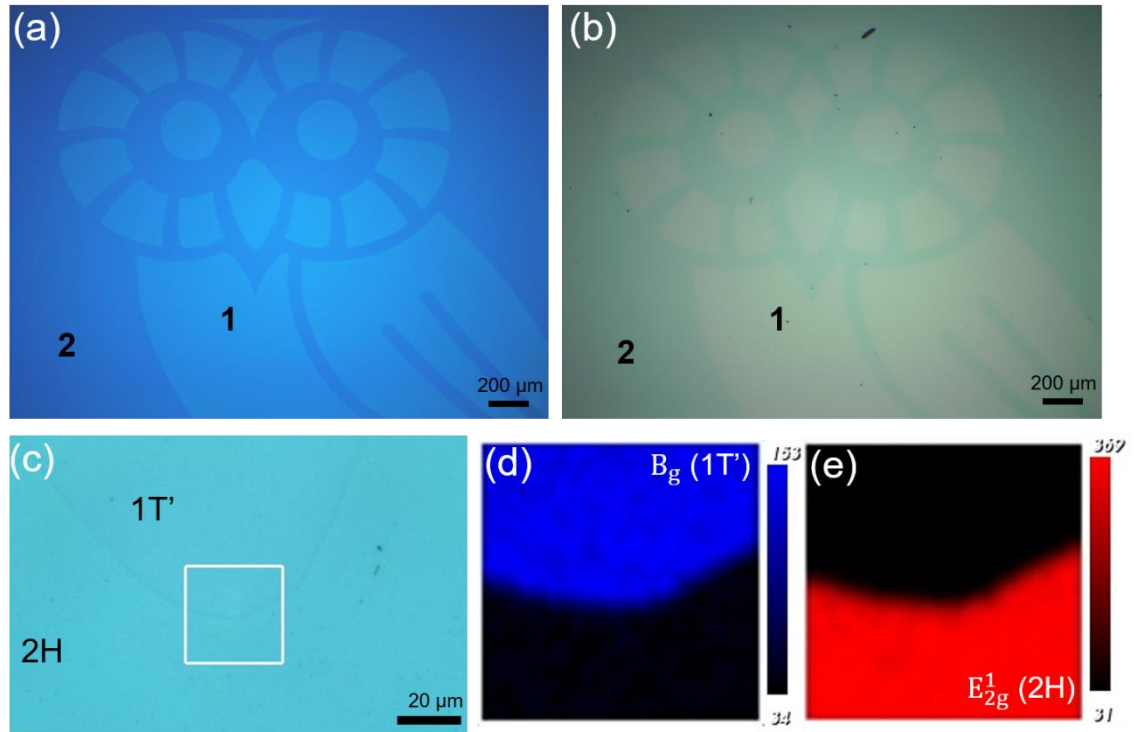
Figure 5-16 – Optical images of a millimeter-sized owl pattern (a) before and (b) synthesis. The owl contour is deposited by Mo on W, which forms 1T' phase. The rest of the area is deposited by Mo, which forms 2H phase. (c) Optical image was taken near the tip of the Owl's nose. Raman intensity maps in the white-side square at (d) B_g for 1T' phase and (e) E^1_{2g} for 2H phase.

Figure 5-17 shows a 2H/1T' MoTe$_2$ strip structure. The spatial distribution of 2H phase and 1T' phase is confirmed by Raman intensity mapping. The 1T' phase has a width of 4 µm.
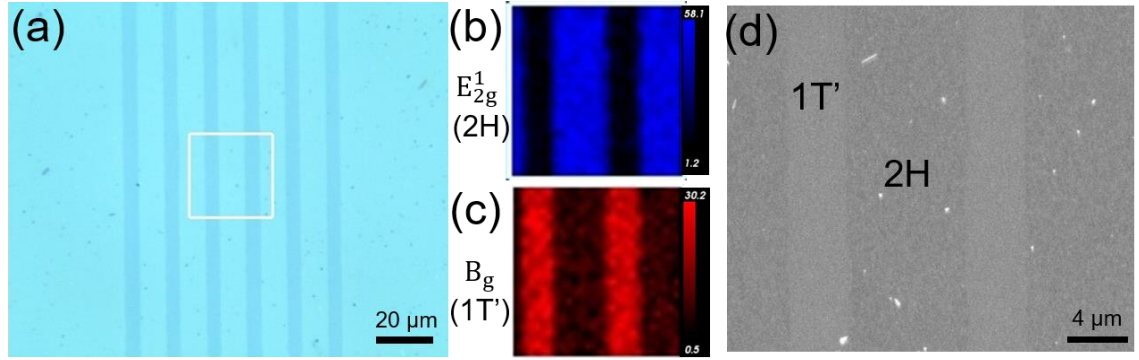
Figure 5-17 – (a) Optical image of a 2H/1T' MoTe$_2$ strip structure. Raman intensity maps in the white-side square at (d) E$_{2g}^1$ for 2H phase and (c) B$_g$ for 1T' phase. (d) SEM image of the strip structure.

We also tried to apply our method to small-scale patterns. In Figure 5-18, the 2H phase gap between two 1T' phase pads is around 1 um wide. Besides, the width of the 1T' phase strip in the center of the gap is around hundreds of nm.
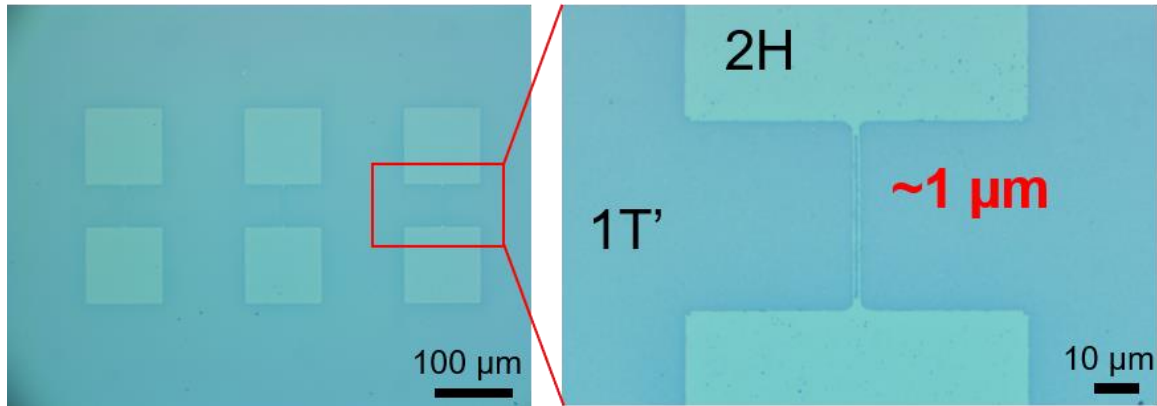
Figure 5-18 – Delicate structure of 2H/1T' MoTe₂.

All the results above show that our method for spatial synthesis of 2H and 1T' MoTe₂ doesn't only work for large-scale patterns, but also work for small features.

These patterns demonstrated above were fabricated by covering W patterns completely with a layer of Mo. This method can grow large films but the synthesized films are continuous conductive, which may not be suitable for some applications such as chip-scale electronic devices. Therefore, we modified the synthesis method by adding another step of lithography before Mo deposition. As a result, Mo is only deposited on the selective area and the 2H/1T' MoTe₂ patterns can be isolated from each other.

The modified strategy is displayed in Figure 5-19 (a). Square W patterns were deposited on SiO₂/Si first by lithography and sputtering. During the second lithography, a dumbbell-shaped mask was used and aligned precisely to the W squares. Therefore, after Mo deposition and lift-off process, a Mo channel was formed

in-between two Mo/W squares. Figure 5-19 (b) shows an optical image of an as-fabricated pattern. Thin W layer with light blue color can be observed due to a little mismatch derived from two lithography steps. These structures were then loaded into the furnace for synthesis.
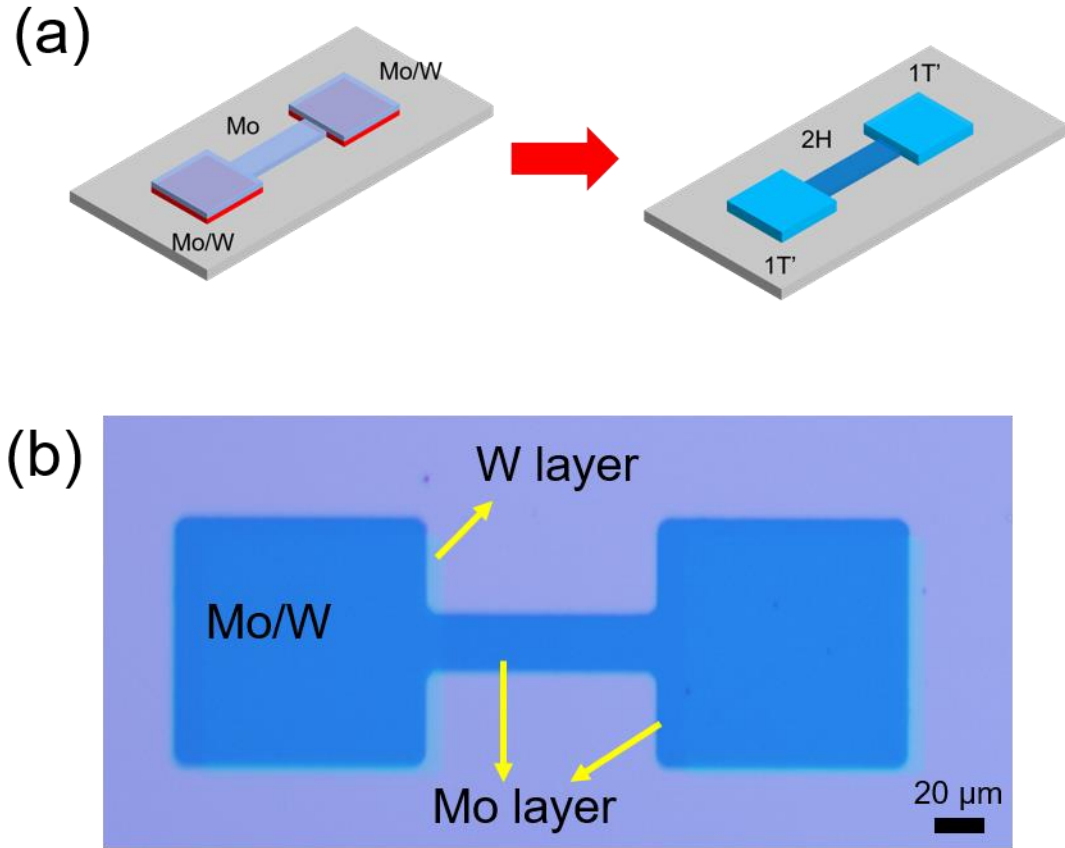
Figure 5-19 - (a) Schematic illustration of modified phase patterning strategy. (b) Optical image of the as-fabricated dumbbell-shaped pattern, where Mo channel connects two Mo/W square pads.

Optical images, Raman spectra, SEM image and Raman intensity maps of a synthesized pattern are presented in Figure 5-20. The difference of color contrast between the channel and the squares is visible in Figure 5-20 (a). There are clear boundaries formed at the ends of the channel. Raman spectra taken at the channel, squares, and the W layer shows that 2H phase $MoTe_2$, 1T' phase $MoTe_2$ and 1T' phase

WTe₂ have been formed, respectively, as displayed in Figure 5-20 (c). Figure 5-20 (d)(e)(f) are Raman intensity maps at E_{2g}^1 (2H MoTe₂), B_g (1T' MoTe₂), and A_1^2 (1T' WTe₂) at the intersection of the channel and the square. They clearly suggest that 2H MoTe₂ forms only in the channel, 1T' MoTe₂ forms only in the square, and 1T' WTe₂ forms only at the edge of the square, where W layer exposes. The spatial distribution of 2H MoTe₂, 1T' MoTe₂, 1T' WTe₂ agrees well with our expectation, implying our modified strategy is effective.
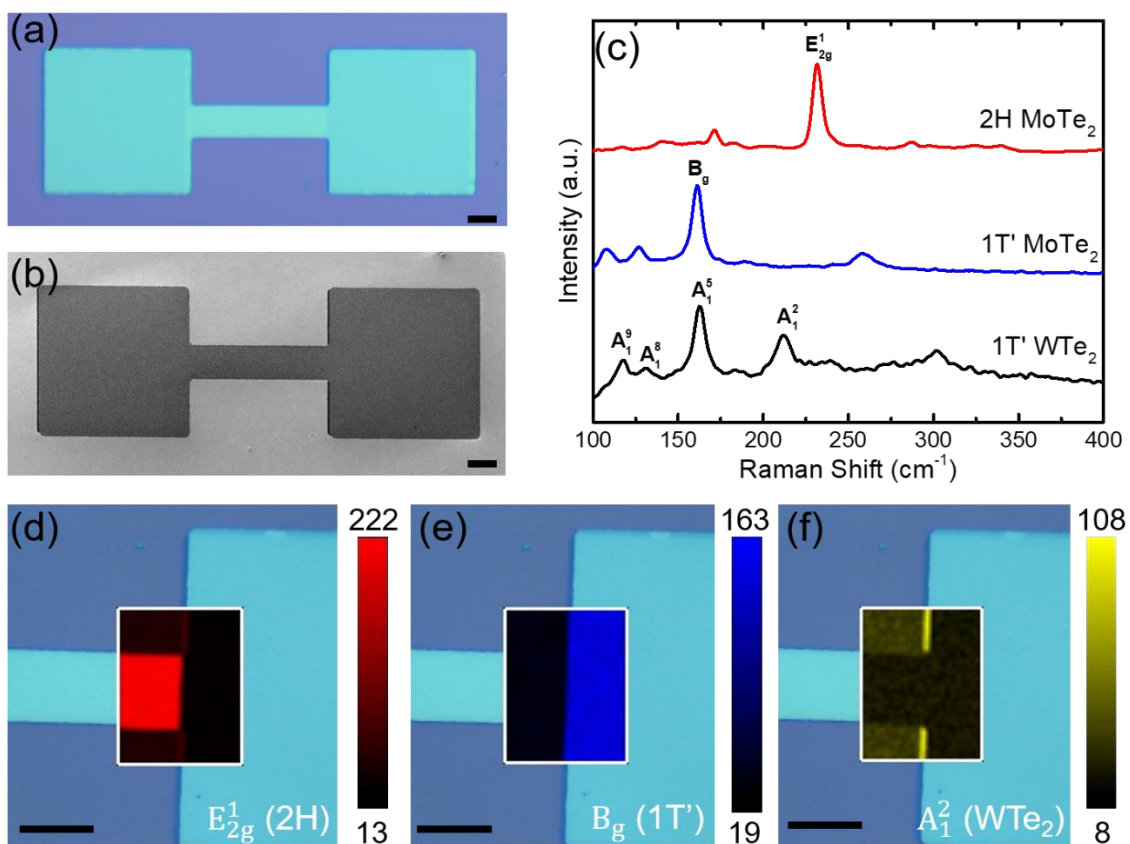
Figure 5-20 – (a) Optical image and (b) SEM image of a dumbbell-shaped pattern synthesized by the modified strategy. (c) Raman spectra show that 2H

MoTe2, 1T' MoTe2, and 1T' WTe2 have been formed in the channel area, in the square area, and near the edge of the square, respectively. (d)(e)(f) Raman intensity mappings at E_{2g}^1, B_g, and A_1^2 demonstrate the spatical distribution of 2H MoTe2, 1T' MoTe2, and 1T' WTe2.

In addition to making a single device, this method also has the ability to fabricate a large number of devices on the same substrate. Figure 5-21 (a) shows an optical image of nearly 60 devices on SiO_2/Si, each of which has a 2H phase channel and two 1T' phase squares.

Since the 2H/1T' MoTe2 dumbbell-shaped structure has been successfully synthesized, we were wondering if the 1T' phase can serve as the electrodes to measure the electrical properties of 2H phase channel. Gold electrical probes were directly contacted to the 1T' phase squares. A voltage from -5 V to 5 V was applied at five different devices, and the corresponding current was collected in Figure 5-21 (b). It can be observed that the I-V characteristics of all the five devices have very similar behavior and appear to be linear. This suggests that 2H channel and 1T' square has formed a nice contact with a low barrier.
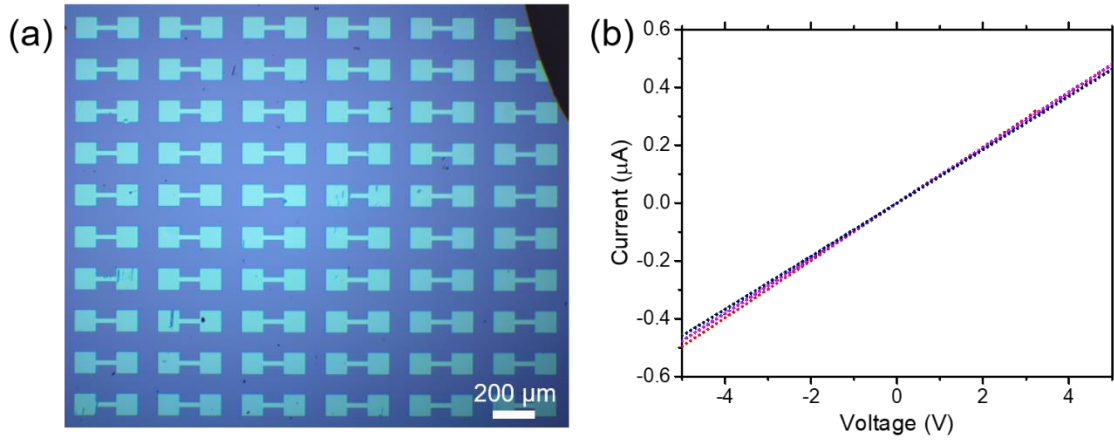
Figure 5-21 – I-V curves measured at five different devices.

5.5. Conclusion

In this chapter, we demonstrated a strategy to spatially pattern the phase of MoTe$_2$ films. A series of technique has been adapted to characterize 2H and 1T' MoTe$_2$ synthesized by this novel method. We also showed that this strategy is suitable not only for large-scale patterns but also for tiny features. A substrate with tens of dumbbell-shaped devices has been successfully fabricated, each of which has a 2H phase channel connected by a 1T' phase square on each side. This work further increases the possibility of the large-scale application of MoTe$_2$.

<div align="right">

Chapter 6

</div>

Ultrafast Electron Diffraction on 2H MoTe$_2$

6.1. Introduction

6.1.1. Pump-probe experiment

Pump-probe experiment is a time-resolved measurement used to study ultrafast electronic dynamics. Figure 6-1 shows a schematic illustration of the pump-probe experiment. One laser pulse is used as a pump to move the sample into an excited state, while another delayed and weaker laser pulse is used to measure the spectrum and monitor the kinetics of the excited state. Pulse duration and bandwidth are the important features of the experiment. Because the temporal resolution of the experiment is limited by the duration of the pump and probe pulses, an ultrafast laser such as picosecond or femtosecond laser is always used as the light source.
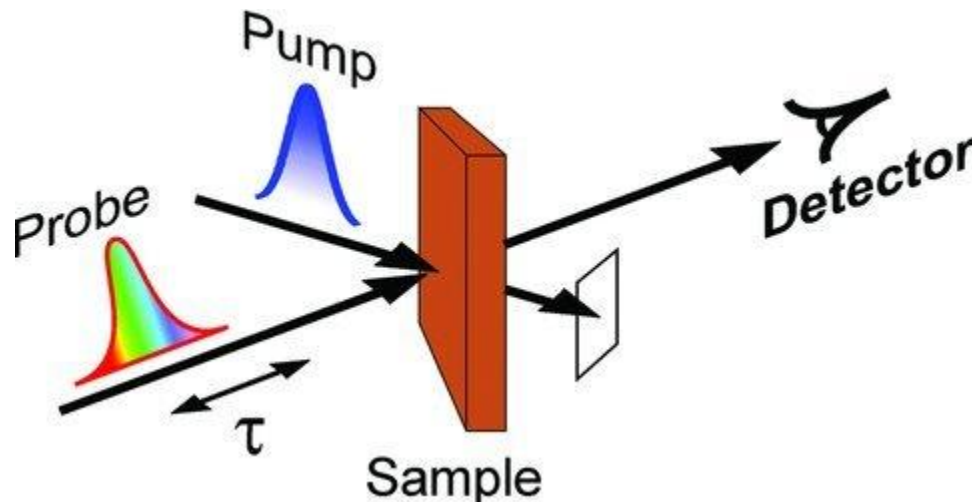
Figure 6-1 – Basic schematic illustration of a pump-probe experiment.[130]

Pump-probe spectroscopy is a useful technique to study atomic motion during chemical reactions, molecular vibrations, photon absorption and emission, and many scattering phenomena which occur on fast time scale.

6.1.2. Ultrafast electron diffraction

The conventional ultrafast optical spectroscopy can only provide indirect information about structural dynamics and the spatial resolution is limited to micron scales due to the diffraction limit. Ultrafast electron diffraction (UED) is a pump-probe experiment method based on electron diffraction from ultrafast electron pulses, which can provide sub-angstrom spatial resolution together with sub-picosecond temporal resolution.

The principle of UED is similar to pump-probe spectroscopy, which is shown in Figure 6-2. The pump laser pulse is used to excite the sample to create a non-equilibrium state, while another UV laser hits a photocathode to generate electron pulses via the photoelectric effect. These electron pulses are then accelerated through a high voltage and pass through the sample to form diffraction patterns on a detector. Recording the diffraction patterns as a function of the time delay between the pump laser and UV laser provides the structural information and dynamics of charge carriers.
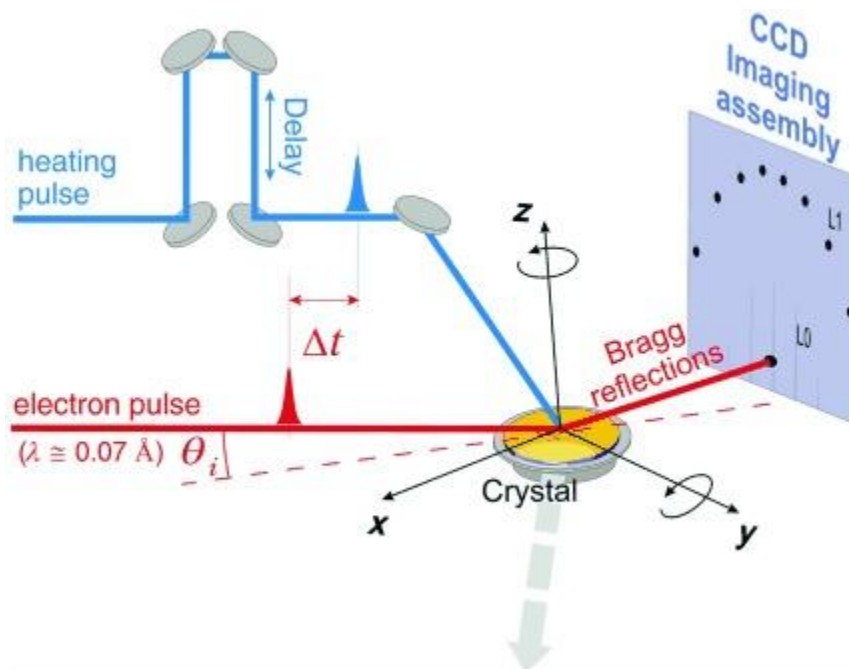
Figure 6-2 - Schematic illustration of an ultrafast electron diffraction experiment.[131]

Lin et al.[132] studied the probing the subpicosecond conversion of photoenergy to lattice vibrations in a bilayer $MoSe_2$ by UED. It was found that when creating a high charge carrier density, the energy is efficiently transferred to $MoSe_2$ lattice within 1 ps. A representative electron diffraction pattern and intensity profile are demonstrated in Figure 6-3. Each image is accumulated over ~7000 pulses from multiple scans. According to Debye-Waller equation,

Equation 6-1

$$I = I_0 e^{-\Delta<u^2>_{\Delta T}\times Q^2}, \text{ or In } \left(\frac{I_0}{I}\right) = \Delta<u^2>_{\Delta T}\times Q^2$$

Where I is the diffraction intensity, I_0 is the value of the initial diffraction intensity, $\Delta<u^2>_{\Delta T}$ is the mean-square displacements, Q is a reciprocal lattice vector 2π over interplanar spacing d. $\Delta<u^2>_{\Delta T}$ can be obtained by plotting In $\left(\frac{I_0}{I}\right)$ vs. Q^2.
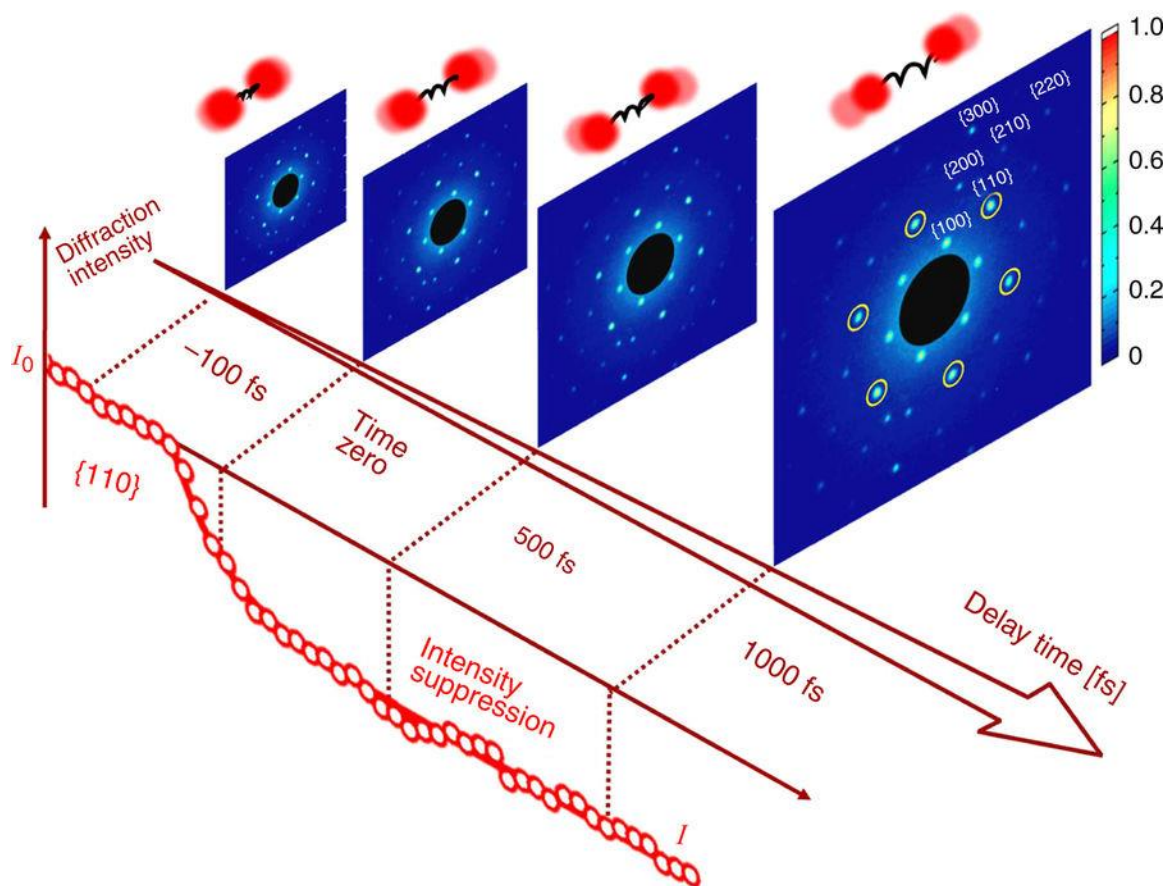
Figure 6-3 - Snapshots of electron diffraction of MoSe$_2$ bilayer for Debye-Waller factor (DWF) measurements.[132]

6.2. Method

To investigate the nonradiative process in multilayer 2H MoTe$_2$, a 9 nm thick 2H MoTe$_2$ was transferred to a 10 nm thick Si$_3$N$_4$ membrane TEM grid. UED experiments with a temporal resolution of ~200 fs were performed at MeV-UED facility at SLAC National Accelerator Laboratory.[133] The 2H MoTe$_2$ was photoexcited by 400 nm (3.1 eV) and 800 nm (1.5 eV) laser respectively. The light-induced energy created a high carrier density, resulting in a temperature increase of tens of kelvin in ~100 fs. Electron-phonon coupling further transformed the electronic energy to vibrational energy, which might cause a structural phase transition.

6.3. Experimental results

Figure 6-4 shows collected diffraction images at different delay time, from -5.0 ps to 18.2 ps. Negative delay times mean the electron probe pulse precedes the optical pump pulse on the sample. A series of diffraction planes can be observed, the color of which indicate the Bragg peak diffraction intensities. Red color represents a relatively high intensity, while blue color represents a relatively low intensity.
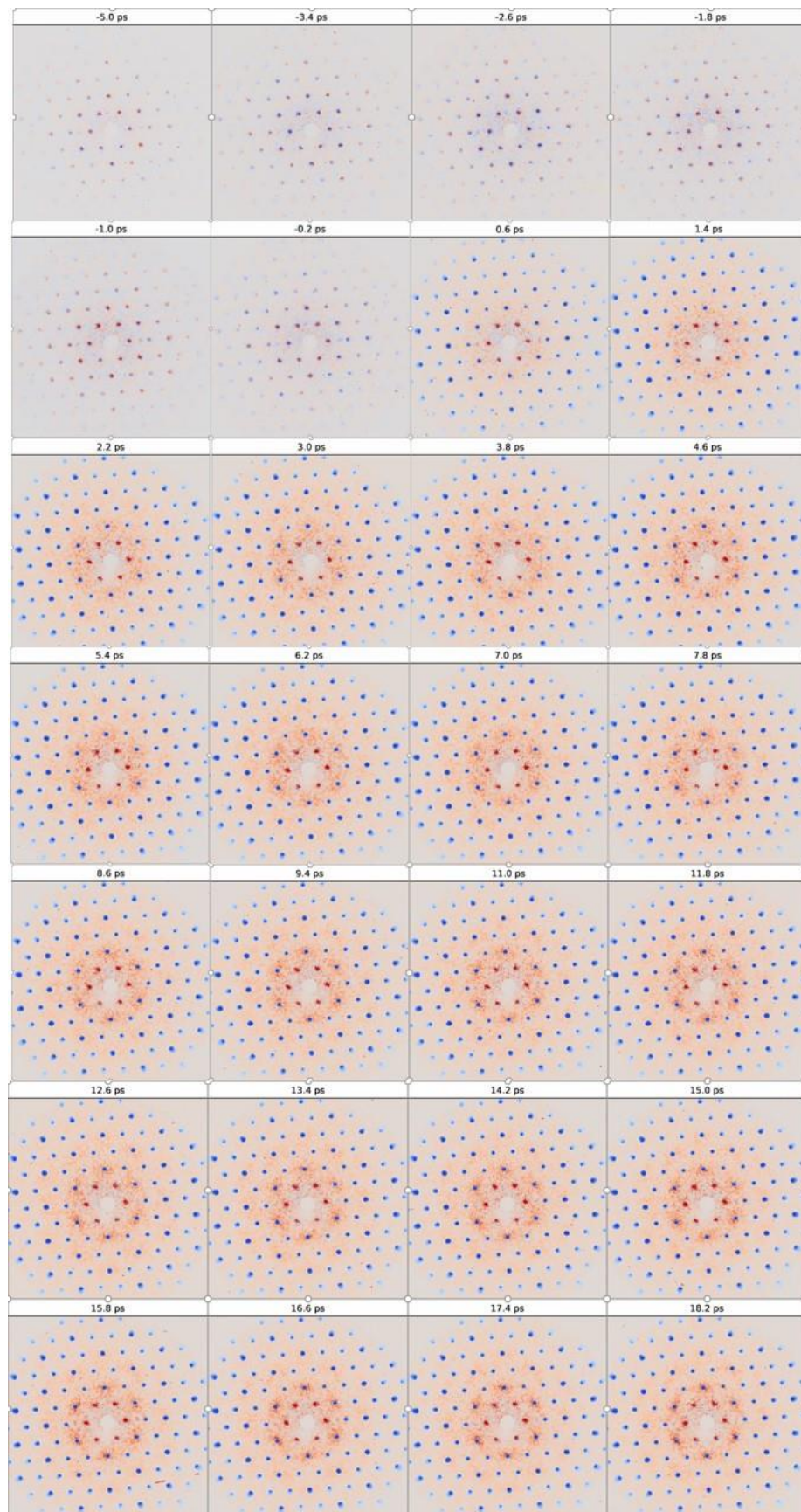
Figure 6-4 – The evolution of Bragg peak diffraction intensities of different planes over delay time.

Diffuse scattering arising from inelastic scattering was observed between Bragg peaks. Figure 6-5 shows collected diffuse scattering images at different delay time, from -5.0 ps to 18.2 ps.
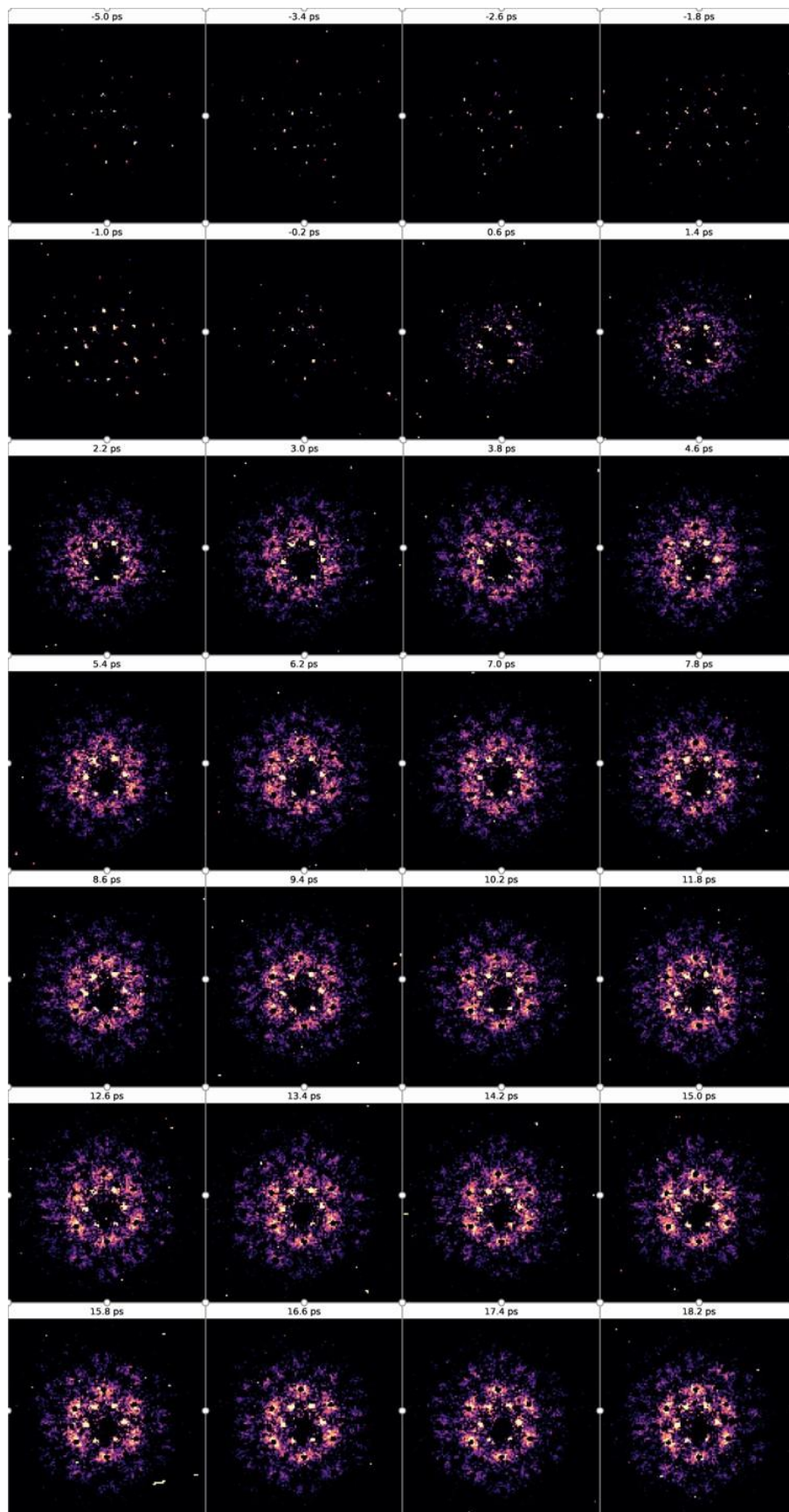
Figure 6-5 - The evolution of diffusing scattering over delay time.

Pump-probe kinetic plots of 12 diffraction planes by 400 nm excitation with pump fluence 0.25 mJ/cm^2 are displayed in Figure 6-6 (a). All the pump-probe kinetics have been normalized to one at the negative delay time I$_0$. Figure 6-6 (b) demonstrates lifetimes of all the kinetic plots. The average lifetime is ~1.3 ps.
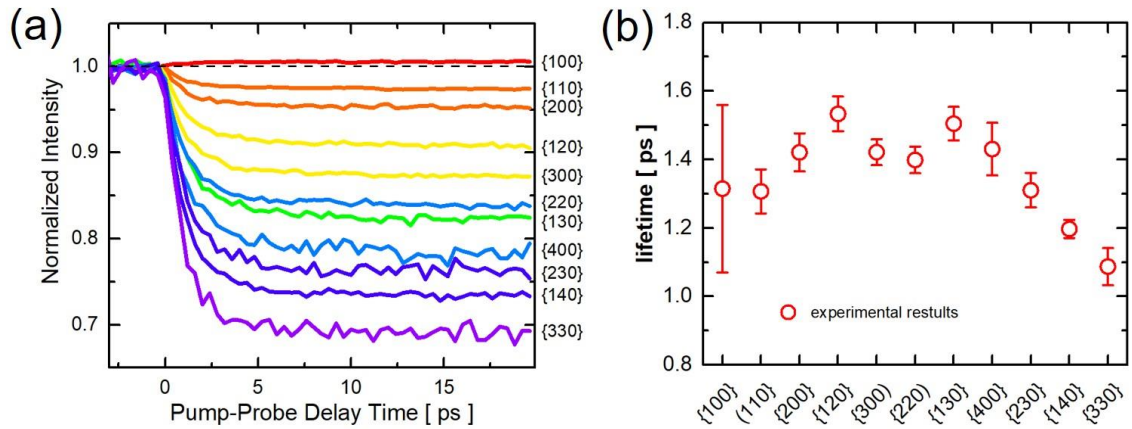
Figure 6-6 – (a) Pump-probe plots of diffraction planes excited by 400 nm pump. (b) Lifetimes of each kinetic plot.

Figure 6-7 (a) shows photon distribution in momentum space, where several points are labeled. The momentum-dependent kinetic plots of these points are demonstrated in Figure 6-7 (b). Each curve has been fitted to an exponential function and the lifetime of each is calculated. An anisotropic population of phonon branches specifically located at M-point is observed.
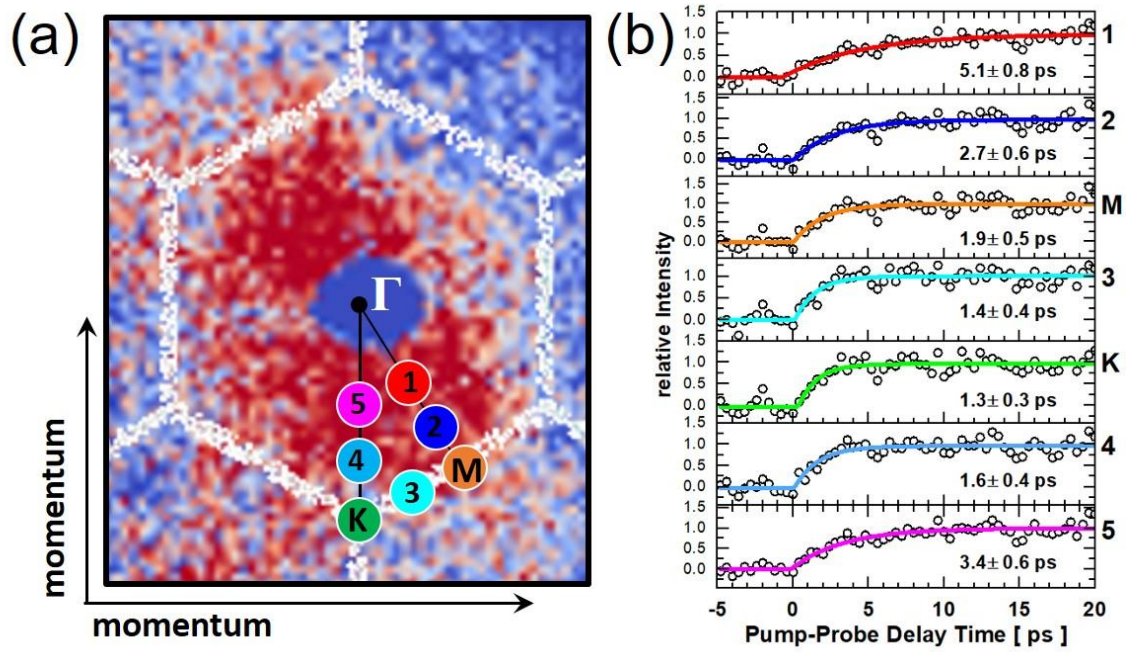
Figure 6-7 – (a) Photon distribution in momentum space. (b) Momentum-dependent kinetic plots of different points.

In addition, 800 nm excitation was also used to pump the sample. The momentum dependent kinetic plots of different points are displayed in Figure 6-8. It can be observed that the lifetimes of these traces are closer compared to those excited by 400 nm.
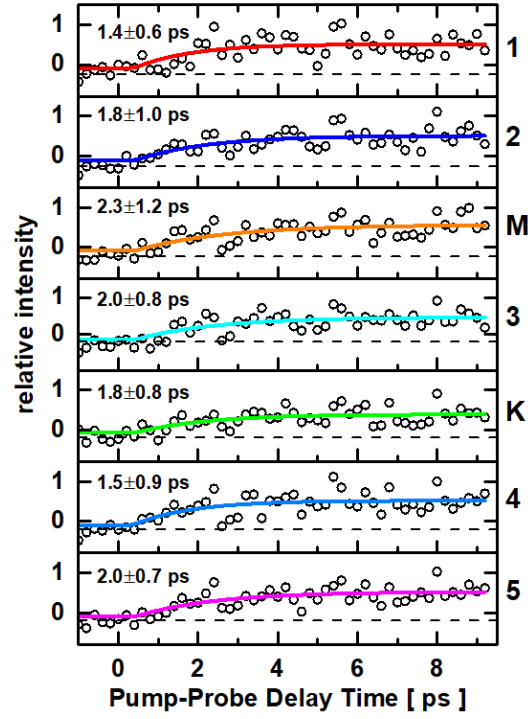
Figure 6-8 - Momentum-dependent kinetic plots of different points by 800 nm pump excitation.

6.4. Conclusion

We investigated the nonradiative process in 2H MoTe$_2$ by using ultrafast electron diffraction. The pump-probe kinetics and momentum-dependent kinetics were studied and the lifetimes were calculated. The experimental results need to be further explained by theoretical simulations.

<div align="right">

Chapter 7

</div>

Summary and Outlook

7.1. Thesis summary

MoTe$_2$ is such a unique material with two stable phases and a lot of interesting properties, which has attracted many researchers including me to study.

Synthesis is the foundation for materials science, so we started our study from MoTe$_2$ growth in Chapter 1. Large-area MoTe$_2$ films were successfully synthesized by CVD method. The phase could be controlled by reaction temperature and time. We further demonstrated a method for spatial phase-patterning of 2H and 1T' phase in Chapter 5. This method worked both for large-scale patterns and for microscale features.

To better understand the structural differences and properties of 2H and 1T' MoTe$_2$, systematic characterizations were performed by using a variety of techniques in Chapter 1 and 5. Raman spectroscopy, SEM, AFM, XPS, XRD, TEM, UV-vis

spectroscopy, MExS, HAADF and EDX provided a wealth of information about these two phases.

In addition to synthesis and characterization, we also explored the applications of $MoTe_2$. In Chapter 3 and 5, $MoTe_2$-based electrical devices have been fabricated and measured. 1T' phase was found to provide a natural edge contact to 2H phase, reducing the contact resistance and improving the device performance. Besides, Raman enhancement on $MoTe_2$ films and their heterostructures were studied in Chapter 4. The results indicated that they could be used as novel SERS substrates.

Last but not least, we studied the fundamental physics in 2H $MoTe_2$ by UED. As presented in Chapter 6, the electron diffraction patterns recorded the light-induced structural transitions at a short time scale, which also provided opportunities to study the nonradiative process such as electron-phonon interaction.

In summary, this thesis doesn't only explore the fundamental properties of $MoTe_2$ but also paves the way towards the large-scale application of $MoTe_2$ in different areas, such as electronic and optoelectronic devices.

7.2. Outlook and future work

There are still a lot of room and many interesting topics to be explored in $MoTe_2$.

Synthesizing single-layer MoTe$_2$ in-plane heterostructure is still challenging. Besides, researchers also need to pay attention to preventing MoTe$_2$ from oxidation. The direct synthesis of the vertical heterostructures of 2H and 1T' MoTe$_2$ hasn't been reported yet.

The mechanism of the phase transition between 2H phase and 1T' phase is still not very clear. In situ measurement and observation would be really helpful to explain the formation and transition of these two phases.

We already showed the ability to phase-patterning of 2H and 1T' phases. Next, we will make use of it and fabricate more complex devices with advanced functions.

We will explore more properties and applications of MoTe$_2$, such as catalytic performance, optics and plasmonics, mechanical properties, doping techniques and band structure engineering.

References

(1)   Novoselov, K. S.; Geim, A. K.; Morozov, S. V.; Jiang, D.; Zhang, Y.; Dubonos, S. V.; Grigorieva, I. V.; Firsov, A. A. *Science (80-.).* **2004**, *306* (5696), 666–669.

(2)   Geim, A. K.; Grigorieva, I. V. *Nature* **2013**, *499* (7459), 419–425.

(3)   Novoselov, K. S.; Geim, A. K.; Morozov, S. V; Jiang, D. A.; Zhang, Y.; Dubonos, S. V; Grigorieva, I. V; Firsov, A. A. *Science (80-.).* **2004**, *306* (5696), 666–669.

(4)   Yi, M.; Shen, Z. *J. Mater. Chem. A* **2015**, *3* (22), 11700–11715.

(5)   Miao, C.; Zheng, C.; Liang, O.; Xie, Y.-H. In *Physics and Applications of Graphene - Experiments*; 2011; pp 37–54.

(6)   Shen, J.; He, Y.; Wu, J.; Gao, C.; Keyshar, K.; Zhang, X.; Yang, Y.; Ye, M.; Vajtai, R.; Lou, J.; Ajayan, P. M. *Nano Lett.* **2015**, *15* (8), 5449–5454.

(7)   Ni, Z. H.; Wang, H. M.; Kasim, J.; Fan, H. M.; Yu, T.; Wu, Y. H.; Feng, Y. P.; Shen, Z. X. *Nano Lett.* **2007**, *7* (9), 2758–2763.

(8)   Geim, A. K.; Novoselov, K. S. *Nat. Mater.* **2007**, *6* (3), 183–191.

(9)   Katsnelson, M. I. *Mater. Today* **2007**, *10* (1), 20–27.

(10) Nair, R. R.; Blake, P.; Grigorenko, A. N.; Novoselov, K. S.; Booth, T. J.; Stauber, T.; Peres, N. M. R.; Geim, A. K. *Science (80-.).* **2008**, *320* (5881), 1308.

(11) Balandin, A. A.; Ghosh, S.; Bao, W.; Calizo, I.; Teweldebrhan, D.; Miao, F.; Lau, C. N. *Nano Lett.* **2008**, *8* (3), 902–907.

(12) Lee, C.; Wei, X.; Kysar, J. W.; Hone, J. *Science (80-.).* **2008**, *321* (5887), 385–388.

(13) Ferrari, A. C. *Solid State Commun.* **2007**, *143*, 47–57.

(14) Zhang, B.; Lee, W. H.; Piner, R.; Kholmanov, I.; Wu, Y.; Li, H.; Ji, H.; Ruoff, R. S. *ACS Nano* **2012**, *6* (3), 2471–2476.

(15) Lin, Y.; Connell, J. W. *Nanoscale* **2012**, *4* (22), 6908–6939.

(16) Gupta, A.; Sakthivel, T.; Seal, S. *Prog. Mater. Sci.* **2015**, *73*, 44–126.

(17) Gorbachev, R. V.; Riaz, I.; Nair, R. R.; Jalil, R.; Britnell, L.; Belle, B. D.; Hill, E. W.; Novoselov, K. S.; Watanabe, K.; Taniguchi, T.; Geim, A. K.; Blake, P. *Small* **2011**, *7* (4), 465–468.

(18) Choi, W.; Choudhary, N.; Han, G. H.; Park, J.; Akinwande, D.; Lee, Y. H. *Mater. Today* **2017**, *20* (3).

(19) Duerloo, K. A. N.; Li, Y.; Reed, E. J. *Nat. Commun.* **2014**, *5*, 4214.

(20) Lee, C.; Yan, H.; Brus, L. E.; Heinz, T. F.; Hone, J.; Ryu, S. *ACS Nano* **2010**, *4* (5), 2695–2700.

(21) Tonndorf, P.; Schmidt, R.; Böttger, P.; Zhang, X.; Börner, J.; Liebig, A.; Albrecht, M.; Kloc, C.; Gordan, O.; Zahn, D. R. T.; Michaelis de Vasconcellos, S.; Bratschitsch, R. *Opt. Express* **2013**, *21* (4), 4908.

(22) Gong, Y.; Lei, S.; Ye, G.; Li, B.; He, Y.; Keyshar, K.; Zhang, X.; Wang, Q.; Lou, J.; Liu, Z.; Vajtai, R.; Zhou, W.; Ajayan, P. M. *Nano Lett.* **2015**, *15* (9), 6135–6141.

(23) Radisavljevic, B.; Radenovic, A.; Brivio, J.; Giacometti, V.; Kis, A. *Nat. Nanotechnol.* **2011**, *6* (3), 147–150.

(24) Huang, X.; Zeng, Z.; Fan, Z.; Liu, J.; Zhang, H. *Adv. Mater.* **2012**, *24* (45), 5979–6004.

(25) Kim, K. K.; Hsu, A.; Jia, X.; Kim, S. M.; Shi, Y.; Dresselhaus, M.; Palacios, T.; Kong, J. *ACS Nano* **2012**, *6* (10), 8583–8590.

(26) Voiry, D.; Salehi, M.; Silva, R.; Fujita, T.; Chen, M.; Asefa, T.; Shenoy, V. B.; Eda, G.; Chhowalla, M. *Nano Lett.* **2013**, *13* (12), 6222–6227.

(27) Zhang, H. *ACS Nano* **2015**, *9* (10), 9451–9469.

(28) Xiong, P.; Peng, L.; Chen, D.; Zhao, Y.; Wang, X.; Yu, G. *Nano Energy* **2015**, *12*, 816–823.

(29) Deng, K.; Wan, G.; Deng, P.; Zhang, K.; Ding, S.; Wang, E.; Yan, M.; Huang, H.; Zhang, H.; Xu, Z.; Denlinger, J.; Fedorov, A.; Yang, H.; Duan, W.; Yao, H.; Wu, Y.; Fan, S.; Zhang, H.; Chen, X.; Zhou, S. *Nat. Phys.* **2016**, *12* (12), 1105–1110.

(30) Dawson, W. G.; Bullett, D. W. *J. Phys. C Solid State Phys.* **1987**, *20*, 6159.

(31) Hughes, H. P.; Friend, R. H.; E, B. B.; Clarke R, M. E. and H. H. P.; S, K.; F, M. L.; C, M. H.; J, van der P. L.; J, van der P. L.; Vellinga M B, de J. R. and H. C.; Wilson J A, D. S. F. J. and M. S.; D, W. J. A. and Y. A. *J. Phys. C Solid State Phys.* **1978**, *11* (3), L103–L105.

(32) Ruppert, C.; Aslan, O. B.; Heinz, T. F. *Nano Lett.* **2014**, *14* (11), 6231–6236.

(33) Zoaeterb, M.; Morsia, M.; Comma Bonneta, A. A. *Synth. Met.* **1995**, *71*, 2041–2042.

(34) Pradhan, N. R.; Rhodes, D.; Feng, S.; Xin, Y.; Memaran, S.; Moon, B.; Terronees, H.; Terrones, M.; Balicas, L. *ACS Nano* **2014**, *8* (6), 5911–5920.

(35) Qian, X.; Liu, J.; Fu, L.; Li, J. *Science (80-.).* **2014**, *346* (6215).

(36) Keum, D. H.; Cho, S.; Kim, J. H.; Choe, D.-H.; Sung, H.-J.; Kan, M.; Kang, H.; Hwang, J.-Y.; Kim, S. W.; Yang, H.; Chang, K. J.; Lee, Y. H. *Nat. Phys.* **2015**, *11* (6), 482–486.

(37) Qi, Y.; Naumov, P. G.; Ali, M. N.; Rajamathi, C. R.; Schnelle, W.; Barkalov, O.; Hanfland, M.; Wu, S. C.; Shekhar, C.; Sun, Y.; Süß, V.; Schmidt, M.; Schwarz, U.; Pippel, E.; Werner, P.; Hillebrand, R.; Förster, T.; Kampert, E.; Parkin, S.; Cava, R. J.; Felser, C.; Yan, B.; Medvedev, S. A. *Nat. Commun.* **2016**, *7*, 11038.

(38) Predel, B. In *Li-Mg – Nd-Zr*; Springer-Verlag: Berlin/Heidelberg, 1997; pp 1–3.

(39) Zhou, Y.; Reed, E. J. *J. Phys. Chem. C* **2015**, *119* (37), 21674–21680.

(40) Li, Y.; Duerloo, K.-A. N.; Wauson, K.; Reed, E. J. *Nat. Commun.* **2016**, *7*, 10671.

(41) Wang, Y.; Xiao, J.; Zhu, H.; Li, Y.; Alsaid, Y.; Fong, K. Y.; Zhou, Y.; Wang, S.; Shi, W.; Wang, Y.; Zettl, A.; Reed, E. J.; Zhang, X. *Nature* **2017**.

(42) Cho, S.; Kim, S.; Kim, J. H.; Zhao, J.; Seok, J.; Keum, D. H.; Baik, J.; Choe, D. H.; Chang, K. J.; Suenaga, K.; Kim, S. W.; Lee, Y. H.; Yang, H. *Science (80-.).* **2015**, *349* (6248), 625–628.

(43) Zhan, Y.; Liu, Z.; Najmaei, S.; Ajayan, P. M.; Lou, J. *Small* **2012**, *8* (7), 966–971.

(44) Song, J.-G.; Park, J.; Lee, W.; Choi, T.; Jung, H.; Lee, C. W.; Hwang, S.-H.; Myoung, J. M.; Jung, J.-H.; Kim, S.-H.; Lansalot-Matras, C.; Kim, H. *ACS Nano* **2013**, *7* (12), 11333–11340.

(45) Woods, J. M.; Jung, Y.; Xie, Y.; Liu, W.; Liu, Y.; Wang, H.; Cha, J. J. *ACS Nano* **2016**, *10* (2), 2004–2009.

(46) Taheri, P.; Wang, J.; Xing, H.; Destino, J. F.; Arik, M. M.; Zhao, C.; Kang, K.; Blizzard, B.; Zhang, L.; Zhao, P.; Huang, S.; Yang, S.; Bright, F. V.; Cerne, J.; Zeng, H. *Mater. Res. Express* **2016**, *3* (7), 75009.

(47) Orofeo, C. M.; Suzuki, S.; Sekine, Y.; Hibino, H. *Appl. Phys. Lett.* **2014**, *105* (8).

(48) Park, J. C.; Yun, S. J.; Kim, H.; Park, J. H.; Chae, S. H.; An, S. J.; Kim, J. G.; Kim, S. M.; Kim, K. K.; Lee, Y. H. *ACS Nano* **2015**, *9* (6), 6548–6554.

(49) Yoo, Y.; DeGregorio, Z. P.; Su, Y.; Koester, S. J.; Johns, J. E. *Adv. Mater.* **2017**, *29* (16).

(50) Yamamoto, M.; Wang, S. T.; Ni, M.; Lin, Y. F.; Li, S. L.; Aikawa, S.; Jian, W. Bin; Ueno, K.; Wakabayashi, K.; Tsukagoshi, K. *ACS Nano* **2014**, *8* (4), 3895–3903.

(51) Zhou, L.; Xu, K.; Zubair, A.; Liao, A. D.; Fang, W.; Ouyang, F.; Lee, Y. H.; Ueno, K.; Saito, R.; Palacios, T.; Kong, J.; Dresselhaus, M. S. *J. Am. Chem. Soc.* **2015**, *137* (37), 11892–11895.

(52) Kan, M.; Nam, H. G.; Lee, Y. H.; Sun, Q. *Phys. Chem. Chem. Phys. Phys. Chem. Chem. Phys* **2015**, *17* (17), 14866–14871.

(53) Bernède, J. .; Amory, C.; Assmann, L.; Spiesser, M. *Appl. Surf. Sci.* **2003**, *219* (3–4), 238–248.

(54) Heda, N. L.; Dashora, A.; Marwal, A.; Sharma, Y.; Srivastava, S. K.; Ahmed, G.; Jain, R.; Ahuja, B. L. *J. Phys. Chem. Solids* **2010**, *71* (3), 187–193.

(55) Yang, L.; Zhang, W.; Li, J.; Cheng, S.; Xie, Z.; Chang, H. *ACS Nano* **2017**, *11* (2), 1964–1972.

(56) Cheng, S.; Yang, L.; Li, J.; Liu, Z.; Zhang, W.; Chang, H. *CrystEngComm* **2017**, *19* (7), 1045–1051.

(57) Yun, W. S.; Han, S. W.; Hong, S. C.; Kim, I. G.; Lee, J. D. *Phys. Rev. B* **2012**, *85* (3), 33305.

(58) Novoselov, K. S.; Geim, A. K.; Morozov, S. V.; Jiang, D.; Zhang, Y.; Dubonos, S. V.; Grigorieva, I. V.; Firsov, A. A. *Science (80-.).* **2004**, *306* (5696), 666–669.

(59) Novoselov, K. S.; Geim, A. K.; Morozov, S. V.; Jiang, D.; Katsnelson, M. I.; Grigorieva, I. V.; Dubonos, S. V.; Firsov, A. A. *Nature* **2005**, *438* (7065), 197–200.

(60) Dean, C. R.; Young, A. F.; Meric, I.; Lee, C.; Wang, L.; Sorgenfrei, S.; Watanabe, K.; Taniguchi, T.; Kim, P.; Shepard, K. L.; Hone, J. *Nat. Nanotechnol.* **2010**, *5* (10), 722–726.

(61) Zhang, Y.; Chang, T. R.; Zhou, B.; Cui, Y. T.; Yan, H.; Liu, Z.; Schmitt, F.; Lee, J.; Moore, R.; Chen, Y.; Lin, H.; Jeng, H. T.; Mo, S. K.; Hussain, Z.; Bansil, A.; Shen, Z. X. *Nat. Nanotechnol.* **2014**, *9* (2), 111–115.

(62) Mak, K. F.; Lee, C.; Hone, J.; Shan, J.; Heinz, T. F. *Phys. Rev. Lett.* **2010**, *105* (13).

(63) Zhao, W.; Ghorannevis, Z.; Chu, L.; Toh, M.; Kloc, C.; Tan, P. H.; Eda, G. *ACS Nano* **2013**, *7* (1), 791–797.

(64) Fang, Z.; Wang, Y.; Liu, Z.; Schlather, A.; Ajayan, P. M.; Koppens, F. H. L.; Nordlander, P.; Halas, N. J. *ACS Nano* **2012**, *6* (11), 10222–10228.

(65) Sun, J.; Lee, H. W.; Pasta, M.; Yuan, H.; Zheng, G.; Sun, Y.; Li, Y.; Cui, Y. *Nat. Nanotechnol.* **2015**, *10* (11), 980–985.

(66) Novoselov, K. S.; Jiang, Z.; Zhang, Y.; Morozov, S. V.; Stormer, H. L.; Zeitler, U.; Maan, J. C.; Boebinger, G. S.; Kim, P.; Geim, A. K. *Science* **2007**, *315* (5817), 1379.

(67) Bertolazzi, S.; Brivio, J.; Kis, A. *ACS Nano* **2011**, *5* (12), 9703–9709.

(68) Xia, F.; Wang, H.; Xiao, D.; Dubey, M.; Ramasubramaniam, A. *Nat. Photonics* **2014**, *8* (12), 899–907.

(69) Zhu, H.; Wang, Y.; Xiao, J.; Liu, M.; Xiong, S.; Wong, Z. J.; Ye, Z.; Ye, Y.; Yin, X.; Zhang, X. *Nat. Nanotechnol.* **2015**, *10* (2), 151–155.

(70) Hong, X.; Kim, J.; Shi, S.-F.; Zhang, Y.; Jin, C.; Sun, Y.; Tongay, S.; Wu, J.; Zhang, Y.; Wang, F. *Nat. Nanotechnol.* **2014**, *9* (9), 682–686.

(71) Gong, Y.; Lin, J.; Wang, X.; Shi, G.; Lei, S.; Lin, Z.; Zou, X.; Ye, G.; Vajtai, R.; Yakobson, B. I.; Terrones, H.; Terrones, M.; Tay, B. K.; Lou, J.; Pantelides, S. T.; Liu, Z.; Zhou, W.; Ajayan, P. M. *Nat. Mater.* **2014**, *13* (12), 1135–1142.

(72) Chen, K.; Wan, X.; Wen, J.; Xie, W.; Kang, Z.; Zeng, X.; Chen, H.; Xu, J. Bin. *ACS Nano* **2015**, *9* (10), 9868–9876.

(73) Rivera, P.; Schaibley, J. R.; Jones, A. M.; Ross, J. S.; Wu, S.; Aivazian, G.; Klement, P.; Seyler, K.; Clark, G.; Ghimire, N. J.; Yan, J.; Mandrus, D. G.; Yao, W.; Xu, X. *Nat. Commun.* **2015**, *6*, 6242.

(74) Gong, Y.; Lei, S.; Ye, G.; Li, B.; He, Y.; Keyshar, K.; Zhang, X.; Wang, Q.; Lou, J.; Liu, Z.; Vajtai, R.; Zhou, W.; Ajayan, P. M. *Nano Lett.* **2015**, *15* (9), 6135–6141.

(75) Li, Q.; Liu, M.; Zhang, Y.; Liu, Z. *Small* **2016**, *12* (1), 32–50.

(76) Zuo, Z.; Xu, Z.; Zheng, R.; Khanaki, A.; Zheng, J. G.; Liu, J. *Sci. Rep.* **2015**, *5*, 14760.

(77) Liu, Z.; Ma, L.; Shi, G.; Zhou, W.; Gong, Y.; Lei, S.; Yang, X.; Zhang, J.; Yu, J.; Hackenberg, K. P.; Babakhani, A.; Idrobo, J. C.; Vajtai, R.; Lou, J.; Ajayan, P. M. *Nat. Nanotechnol.* **2013**, *8* (2), 119–124.

(78) Allain, A.; Kang, J.; Banerjee, K.; Kis, A. *Nat. Mater.* **2015**, *14* (12), 1195–1205.

(79) Popov, I.; Seifert, G.; Tomanek, D. *Phys. Rev. Lett.* **2012**, *108* (15).

(80) Kang, J.; Liu, W.; Sarkar, D.; Jena, D.; Banerjee, K. *Phys. Rev. X* **2014**, *4* (3), 31005.

(81) Xu, Y.; Cheng, C.; Du, S.; Yang, J.; Yu, B.; Luo, J.; Yin, W.; Li, E.; Dong, S.; Ye, P.; Duan, X. *ACS Nano* **2016**, *10* (5), 4895–4919.

(82) Liu, W.; Kang, J.; Sarkar, D.; Khatami, Y.; Jena, D.; Banerjee, K. *Nano Lett.* **2013**, *13* (5), 1983–1990.

(83) Jeong, H.; Oh, H. M.; Bang, S.; Jeong, H. J.; An, S. J.; Han, G. H.; Kim, H.; Yun, S. J.; Kim, K. K.; Park, J. C.; Lee, Y. H.; Lerondel, G.; Jeong, M. S. *Nano Lett.* **2016**, *16* (3), 1858–1862.

(84) Roy, K.; Padmanabhan, M.; Goswami, S.; Sai, T. P.; Ramalingam, G.; Raghavan, S.; Ghosh, A. *Nat. Nanotechnol.* **2013**, *8* (11), 826–830.

(85) Roy, T.; Tosun, M.; Kang, J. S.; Sachid, A. B.; Desai, S. B.; Hettick, M.; Hu, C. C.; Javey, A. *ACS Nano* **2014**, *8* (6), 6259–6264.

(86) Huang, X.; Zeng, Z.; Fan, Z.; Liu, J.; Zhang, H. *Adv. Mater.* **2012**, *24* (45), 5979–6004.

(87) Chuang, H. J.; Tan, X.; Ghimire, N. J.; Perera, M. M.; Chamlagain, B.; Cheng, M. M. C.; Yan, J.; Mandrus, D.; Tománek, D.; Zhou, Z. *Nano Lett.* **2014**, *14* (6), 3594–3601.

(88) Das, S.; Gulotty, R.; Sumant, A. V; Roelofs, A. *Nano Lett.* **2014**, *14* (5), 2861–2866.

(89) Yu, H.; Kutana, A.; Yakobson, B. I. *Nano Lett.* **2016**, *16* (8), 5032–5036.

(90) Chuang, H. J.; Chamlagain, B.; Koehler, M.; Perera, M. M.; Yan, J.; Mandrus, D.; Tománek, D.; Zhou, Z. *Nano Lett.* **2016**, *16* (3), 1896–1902.

(91) Kim, Y.; Kim, A. R.; Yang, J. H.; Chang, K. E.; Kwon, J. D.; Choi, S. Y.; Park, J.; Lee, K. E.; Kim, D. H.; Choi, S. M.; Lee, K. H.; Lee, B. H.; Hahm, M. G.; Cho, B. *Nano Lett.* **2016**, *16* (9), 5928–5933.

(92) Fang, H.; Chuang, S.; Chang, T. C.; Takei, K.; Takahashi, T.; Javey, A. *Nano Lett.* **2012**, *12* (7), 3788–3792.

(93) Kappera, R.; Voiry, D.; Yalcin, S. E.; Branch, B.; Gupta, G.; Mohite, A. D.; Chhowalla, M. *Nat. Mater.* **2014**, *13* (12), 1128–1134.

(94) Kim, S.; Kim, J. H.; Kim, D.; Hwang, G.; Baik, J.; Yang, H.; Cho, S. *2D Mater.* **2017**, *4* (2), 24004.

(95) Empante, T. A.; Zhou, Y.; Klee, V.; Nguyen, A. E.; Lu, I.-H.; Valentin, M. D.; Naghibi Alvillar, S. A.; Preciado, E.; Berges, A. J.; Merida, C. S.; Gomez, M.; Bobek, S.; Isarraraz, M.; Reed, E. J.; Bartels, L. *ACS Nano* **2017**, *11* (1), 900–905.

(96) Sung, J. H.; Heo, H.; Si, S.; Kim, Y. H.; Noh, H. R.; Song, K.; Kim, J.; Lee, C. S.; Seo, S. Y.; Kim, D. H.; Kim, H. K.; Yeom, H. W.; Kim, T. H.; Choi, S. Y.; Kim, J. S.; Jo, M. H. *Nat. Nanotechnol.* **2017**, *12* (11), 1064–1070.

(97) Zhou, L.; Zubair, A.; Wang, Z.; Zhang, X.; Ouyang, F.; Xu, K.; Fang, W.; Ueno, K.; Li, J.; Palacios, T.; Kong, J.; Dresselhaus, M. S. *Adv. Mater.* **2016**, *28* (43), 9526–9531.

(98) Lin, Y. F.; Xu, Y.; Wang, S. T.; Li, S. L.; Yamamoto, M.; Aparecido-Ferreira, A.; Li, W.; Sun, H.; Nakaharai, S.; Jian, W. Bin; Ueno, K.; Tsukagoshi, K. *Adv. Mater.* **2014**, *26* (20), 3263–3269.

(99) Choi, K.; Lee, Y. T.; Kim, J. S.; Min, S. W.; Cho, Y.; Pezeshki, A.; Hwang, D. K.; Im, S. *Adv. Funct. Mater.* **2016**, *26* (18), 3146–3153.

(100) Larentis, S.; Fallahazad, B.; Movva, H. C. P.; Kim, K.; Rai, A.; Taniguchi, T.; Watanabe, K.; Banerjee, S. K.; Tutuc, E. *ACS Nano* **2017**, *11* (5), 4832–4839.

(101) Song, S.; Keum, D. H.; Cho, S.; Perello, D.; Kim, Y.; Lee, Y. H. *Nano Lett.* **2016**, *16* (1), 188–193.

(102) Naylor, C. H.; Parkin, W. M.; Ping, J.; Gao, Z.; Zhou, Y. R.; Kim, Y.; Streller, F.; Carpick, R. W.; Rappe, A. M.; Drndić, M.; Kikkawa, J. M.; Johnson, A. T. C. *Nano Lett.* **2016**, *16* (7), 4297–4304.

(103) Chen, B.; Sahin, H.; Suslu, A.; Ding, L.; Bertoni, M. I.; Peeters, F. M.; Tongay, S. *ACS Nano* **2015**, *9* (5), 5326–5332.

(104) Radisavljevic, B.; Radenovic, A.; Brivio, J.; Giacometti, V.; Kis, A. *Nat. Nanotechnol.* **2011**, *6* (3), 147–150.

(105) Berger, H. H. *Solid State Electron.* **1972**, *15* (2), 145–158.

(106) Liu, Y.; Stradins, P.; Wei, S. H. *Sci. Adv.* **2016**, *2* (4), e1600069.

(107) Kresse, G.; Furthmüller, J. *Phys. Rev. B* **1996**, *54* (16), 11169–11186.

(108) Chiu, M.-H.; Zhang, C.; Shiu, H.-W.; Chuu, C.-P.; Chen, C.-H.; Chang, C.-Y. S.; Chen, C.-H.; Chou, M.-Y.; Shih, C.-K.; Li, L.-J. *Nat. Commun.* **2015**, *6*, 7666.

(109) RAMAN, C. V.; KRISHNAN, K. S. *Nature* **1928**, *121* (3048), 501–502.

(110) Fleischmann, M.; Hendra, P. J.; McQuillan, A. J. *Chem. Phys. Lett.* **1974**, *26* (2), 163–166.

(111) Campion, A.; Kambhampati, P. *Chem. Soc. Rev.* **1998**, *27* (4), 241.

(112) Panneerselvam, R.; Liu, G.-K.; Wang, Y.-H.; Liu, J.-Y.; Ding, S.-Y.; Li, J.-F.; Wu, D.-

Y.; Tian, Z.-Q. *Chem. Commun. Chem. Commun* **2018**, *10* (10), 10–25.

(113) Schlücker, S. *Angew. Chemie - Int. Ed.* **2014**, *53* (19), 4756–4795.

(114) Tian, F.; Bonnier, F.; Casey, A.; Shanahan, A. E.; Byrne, H. J. *Anal. Methods* **2014**, *6* (22), 9116–9123.

(115) Xu, W.; Ling, X.; Xiao, J.; Dresselhaus, M. S.; Kong, J.; Xu, H.; Liu, Z.; Zhang, J. *Proc. Natl. Acad. Sci.* **2012**, *109* (24), 9281–9286.

(116) Ling, X.; Xie, L.; Fang, Y.; Xu, H.; Zhang, H.; Kong, J.; Dresselhaus, M. S.; Zhang, J.; Liu, Z. *Nano Lett.* **2010**, *10* (2), 553–561.

(117) Schedin, F.; Lidorikis, E.; Lombardo, A.; Kravets, V. G.; Geim, A. K.; Grigorenko, A. N.; Novoselov, K. S.; Ferrari, A. C. *ACS Nano* **2010**, *4* (10), 5617–5626.

(118) Tan, Y.; Ma, L.; Gao, Z.; Chen, M.; Chen, F. *Nano Lett.* **2017**, *17* (4), 2621–2626.

(119) Ling, X.; Fang, W.; Lee, Y. H.; Araujo, P. T.; Zhang, X.; Rodriguez-Nieva, J. F.; Lin, Y.; Zhang, J.; Kong, J.; Dresselhaus, M. S. *Nano Lett.* **2014**, *14* (6), 3033–3040.

(120) Zhang, D.; Wu, Y. C.; Yang, M.; Liu, X.; Coileain, C. O.; Abid, M.; Abid, M.; Wang, J. J.; Shvets, I.; Xu, H.; Chun, B. S.; Liu, H.; Wu, H. C. *Sci. Rep.* **2016**, *6*.

(121) Valeš, V.; Kovaříček, P.; Fridrichová, M.; Ji, X.; Ling, X.; Kong, J.; Dresselhaus, M. S.; Kalbáč, M. *2D Mater.* **2017**, *4* (2), 25087.

(122) Xia, M. *Int. J. Spectrosc.* **2018**, *4861472*, 1–14.

(123) Dines, M. B. *Mater. Res. Bull.* **1975**, *10* (4), 287–291.

(124) Py, M. A.; Haering, R. R. *Can. J. Phys.* **1983**, *61* (1), 76–84.

(125) Eda, G.; Yamaguchi, H.; Voiry, D.; Fujita, T.; Chen, M.; Chhowalla, M. *Nano Lett.* **2011**, *11* (12), 5111–5116.

(126) Lin, Y. C.; Dumcenco, D. O.; Huang, Y. S.; Suenaga, K. *Nat. Nanotechnol.* **2014**, *9* (5), 391–396.

(127) Duerloo, K. A. N.; Reed, E. J. *ACS Nano* **2016**, *10* (1), 289–297.

(128) Zhang, C.; KC, S.; Nie, Y.; Liang, C.; Vandenberghe, W. G.; Longo, R. C.; Zheng, Y.; Kong, F.; Hong, S.; Wallace, R. M.; Cho, K. *ACS Nano* **2016**, *10* (8), 7370–7375.

(129) Rhodes, D.; Chenet, D. A.; Janicek, B. E.; Nyby, C.; Lin, Y.; Jin, W.; Edelberg, D.; Mannebach, E.; Finney, N.; Antony, A.; Schiros, T.; Klarr, T.; Mazzoni, A.; Chin, M.; Chiu, Y. C.; Zheng, W.; Zhang, Q. R.; Ernst, F.; Dadap, J. I.; Tong, X.; Ma, J.; Lou, R.; Wang, S.; Qian, T.; Ding, H.; Osgood, R. M.; Paley, D. W.; Lindenberg, A.

174

        M.; Huang, P. Y.; Pasupathy, A. N.; Dubey, M.; Hone, J.; Balicas, L. *Nano Lett.* **2017**, *17* (3), 1616–1622.

(130) Cabanillas-Gonzalez, J.; Grancini, G.; Lanzani, G. *Adv. Mater.* **2011**, *23* (46), 5468–5485.

(131) Vigliotti, F.; Chen, S.; Ruan, C.-Y.; Lobastov, V. a; Zewail, A. H. *Angew. Chem. Int. Ed. Engl.* **2004**, *43* (20), 2705–2709.

(132) Lin, M. F.; Kochat, V.; Krishnamoorthy, A.; Bassman, L.; Weninger, C.; Zheng, Q.; Zhang, X.; Apte, A.; Tiwary, C. S.; Shen, X.; Li, R.; Kalia, R.; Ajayan, P.; Nakano, A.; Vashishta, P.; Shimojo, F.; Wang, X.; Fritz, D. M.; Bergmann, U. *Nat. Commun.* **2017**, *8* (1).

(133) Li, R. K.; Reid, A. H.; Weathersby, S. P.; Brown, G.; Centurion, M.; Chase, T.; Coffee, R.; Corbett, J.; Frisch, J. C.; Guehr, M.; Hartmann, N.; Hast, C.; Ho, L. V.; Jobe, K. R.; Jongewaard, E. N.; Lewandowski, J. R.; Lindenberg, A. M.; May, J. E.; McCormick, D.; Shen, X.; Sokolowski-Tinten, K.; Vecchione, T.; Wu, J.; Yang, J.; Diirr, H. A.; Wang, X. J. *Microsc. Microanal.* **2015**, *21* (S3), 1209–1210.